The Pennsylvania State University

The Graduate School

College of Earth and Mineral Sciences

PHASE TRANSITIONS IN EPITAXIAL RHOMBOHEDRAL

Pb(Zr$_{1-x}$Ti$_X$)O$_3$ THIN FILMS

A Dissertation in

Materials Science and Engineering

by

Daniel Scott Tinberg

Submitted in Partial Fulfillment

of the Requirements

for the Degree of

Doctor of Philosophy

December 2010

The dissertation of Daniel S. Tinberg was reviewed and approved* by the following:

Susan Trolier-McKinstry
Professor of Ceramic Science and Engineering
Dissertation Advisor
Chair of Committee

Clive A. Randall
Professor of Materials Science and Engineering

Elizabeth Dickey
Professor of Materials Science and Engineering

L. Eric Cross
Professor of Electrical Engineering

Dr. Joan Redwing
Professor of Materials Science and Engineering
Chair of Intercollege Graduate Degree Program in Materials Science and Engineering

*Signatures are on file in the Graduate School.

Abstract

It has been shown for bulk materials that the transition from an untilted perovskite to a tilted perovskite can yield a significant reduction in both permittivity as well as piezoelectric coefficients. As a model system to study tilt transitions in thin films, rhombohedral compositions of $Pb(Zr_{1-x}Ti_x)O_3$ were investigated. Films with thicknesses greater than 350 nm were observed to have permittivities in the 400-500 range with loss tangents less than 3% at 10 kHz. Piezoelectric measurements were performed using the wafer flexure method; $e_{31,f}$ coefficients of -2.7 C/m^2 were obtained for x=0.2 films, increasing to -9.1 C/m^2 for x=0.4 films. At 10kHz, the films exhibited bulk Curie temperatures with relative permittivities in excess of 3000, loss tangents less than 5% and bulk Curie-Weiss constants matching those of bulk materials. Likewise, the octahedral tilt transition temperatures for relaxed films are comparable to those of bulk ceramics. However, it was also found that the transition is not between tilted and un-tilted states, but through an intermediate state of non-zero tilt in which there is either a short coherence length for the tilt or smaller tilt angles. The non-zero tilt region persists ~ 100°C <u>above</u> T_{Tilt}. This explains anomalies in the temperature dependence of the relative permittivity and switchable polarization of both bulk ceramics and thin films. The $Pb(Zr_{1-x}Ti_x)O_3$ phase diagram has been modified to illustrate this.

Strained $Pb(Zr_{1-x}Ti_x)O_3$ thin films were also grown by pulsed laser deposition. Due to the large lattice parameter of rhombohedral $Pb(Zr_{1-x}Ti_x)O_3$ a ~10 nm thick buffer layer of relaxed $Pb(Zr_{0.6}Ti_{0.4})O_3$ was used as a pseudo-substrate for lattice matching purposes. High resolution transmission electron microscopy was performed and

confirmed the presence of an untilted buffer layer and octahedral tilting within the strained film. Temperature dependent synchrotron x-ray diffraction was performed and it was found that for the strained films the T_C increased systematically with strain. The superlattice reflection was investigated and found to exist for all compositions to temperatures higher than the reported bulk tilt transition temperature. Based on an analysis of the FWHM of the superlattice reflection, it was found that the T_{Tilt} does not significantly increase with strain. A region of non-zero tilt was found above the bulk tilt transition temperature. The larger strain dependence for the ferroelectric transition, relative to the tilt transition suggests that it may be possible to use strain to stabilize ferroelectric phases without greatly increasing T_{Tilt}. Lastly, it was found that the tilt system for rhombohedral $Pb(Zr_{1-x}Ti_x)O_3$ under biaxial strain remains anti-phase tilting only for both $(100)_{pc}$ and $(111)_{pc}$ films.

Table of Contents

List of Figures

List of Tables

Acknowledgements

I would like to express my gratitude to my advisor, Dr. Susan Trolier-McKinstry, for her patience and understanding in guiding me through graduate school throughout the years. It has been a pleasure to study under her and every discussion is valuable. I would like to thank Drs. Randall, Dickey, and Cross for their suggestions and being on my committee. I would like to thank the technical staff at the Materials Research Lab. and the Materials Characterization Lab. for their help throughout the years.

The work presented in this thesis would not have been able to be completed without the help of many people. At Argonne National Laboratory, Dr. Dillon Fong, Dr. Timothy Fister, Dr. Stephen Streiffer, Dr. Jenia Karapetrova and Peter Baldo all assisted in setting up and running the experiments at the Advanced Photon Source and the Center for Nanoscale Materials. Additionally, Drs. Fong, Fister, and Streiffer were available for numerous conversations concerning the analysis and interpretation of the resulting data. Our collaborators at the University of Sheffield (Yisong Han and Prof. Ian Reaney) in the United Kingdom provided the TEM images and analysis shown in this thesis, along with abundant insights on the research. Special thanks go to Raegan Johnson who worked hand in hand with me studying tilt transitions in perovskites for the past several years. Our almost daily discussions on octahedral tilting, x-ray diffraction, data analysis, and what it all means, were invaluable.

I want to thank all the past and present members of the STM group for their help. I have enjoyed working with all of you throughout the years. Thanks to all my friends that have come and gone at Penn State. Knowing all of you have made getting this

degree a little more pleasurable. Lastly, I need to thank my family for their constant support and encouragement.

Chapter 1   Introduction

1.1 *Motivation*

Oxide materials with the ABO_3 structure have been utilized by the electroceramics industry since the discovery of the large dielectric and piezoelectric properties of $BaTiO_3$ in the 1940s.[1] The high polarizability arises from a phase transition from a high symmetry point group at high temperatures to one which allows a spontaneous polarization. A spontaneous polarization is symmetry allowed only in the 10 pyroelectric point groups as shown in Figure 1.1.[2] Materials which exhibit pyroelectricity also exhibit piezoelectricity.

The development of a spontaneous polarization within perovskites is an example of a ferrodistortive transition in which the number of formula units per unit cell does not change at the transition. For example, in $PbTiO_3$ the development of the spontaneous polarization can be attributed to the relative displacement of the cation and anion sublattices.[3]

In contrast, the antiferrodistortive transition in $PbZrO_3$ occurs when the Pb^{2+} cations displace on two distinct sublattices. In materials like $PbZrO_3$,[4] the transition leads to antiferroelectricity where polarizations on the separate sublattices cancel each other, yielding no net spontaneous polarization within unit cell. Furthermore, the resulting symmetry of the phase influences the properties of the material. Any subsequent phase transitions alter the dielectric and piezoelectric properties. In perovskites, this can be beneficial for temperature independent phase transitions such as a morphotropic phase boundary (MPB). Multiple phase transitions can also be detrimental to the properties

either due to the production of large temperature dependences to the response, or by changes in the polarizability.
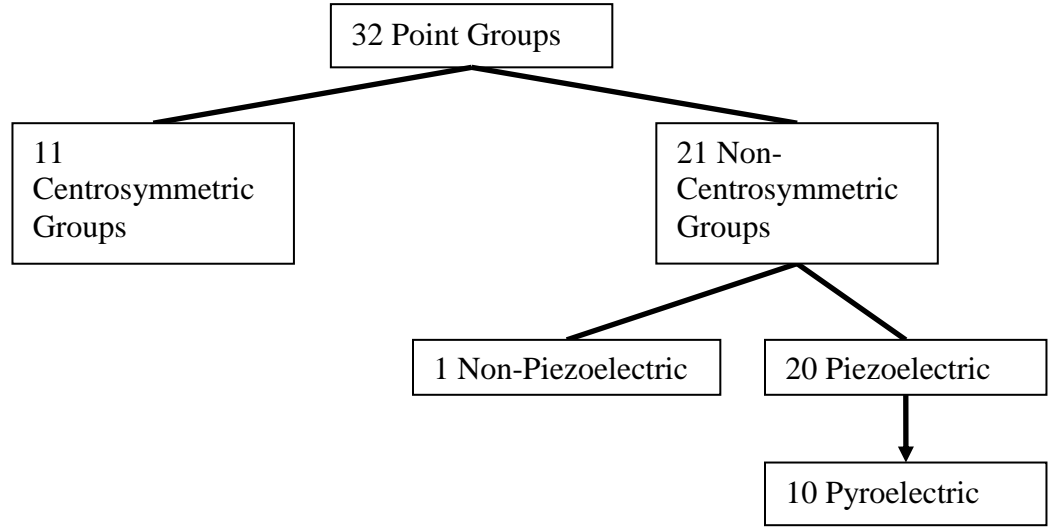
Figure 1.1. Schematic of point groups classifying which may allow piezoelectricity and pyroelectricity.

Tilt transitions are phase transitions which entail rigid rotations of the oxygen octahedra within the material, without necessarily distorting the octahedra. These tend to occur when the Goldschmidt tolerance factor given in Equation 2.1 is below 1;[5]

$$t = \frac{r_A + r_O}{\sqrt{2}(r_B + r_O)},$$

Equation 1.1. Goldschmidt tolerance factor

where r denotes the radii of the A, B, and O ions in an ABO_3 perovskite.

Studying tilt transitions is important in piezoelectric materials because of their unfavorable effects on the piezoelectric constant and the electromechanical coupling factor. As seen in Figure 1.2, there is a correlation between the end-member tolerance

factor and the Curie temperature at the morphotropic phase boundary (MPB).[6] Unfortunately, low tolerance factor materials are often tilted. This can introduce tilted phases to the phase diagram with the tilt phase sometimes occurring near the MPB.[7-10] Moreover, for Pb-free piezoelectrics, replacing Pb^{2+} with a smaller cations, such as Bi^{3+}, in the perovskite structure leads to tilt phases.
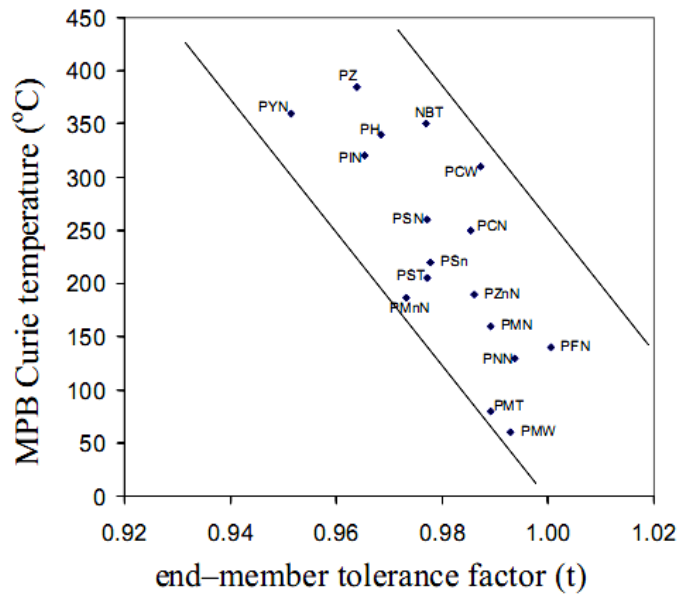
Figure 1.2. T_C at the morphotropic phase boundary for $PbTiO_3$-based materials.[6]

1.2 *Motivation and Organization of the Thesis*

As described above, an understanding of tilt transitions is important to design and control the properties of novel piezoelectric materials. $Pb(Zr_{1-x}Ti_x)O_3$ (PZT) is currently the most important piezoelectric ceramic and has been vigorously studied throughout the years. It contains several tilt transitions on the Zr-rich side of the phase diagram.

3

In order to study the tilt transitions in PZT, several points need to be considered. While bulk $Pb(Zr_{1-x}Ti_x)O_3$ ceramics have been produced for years, single crystal PZT still is not widely available. However, epitaxial films of PZT have been grown[11-13] and allow characterization of high quality PZT near the tilt transition. Thus, epitaxial films formed the heart of this thesis. Chapter 2 is a literature review which explains the various phase transitions perovskites undergo, as well as a more in-depth discussion of the effects of tilting on PZT. A discussion of the equipment used and the experimental procedure is in Chapter 3. The common bottom electrode material used in this study ($SrRuO_3$) also undergoes octahedral tilting. As such, Chapter 4 is devoted to studying the structure of $SrRuO_3$ films in order to understand how it may influence the PZT, as well as to be able to easily separate out any effects of the $SrRuO_3$ from the PZT in the diffraction patterns. Next, in Chapter 5 the growth and characterization of relaxed PZT are described to determine how the tilt transition affects the properties and structure of the films. In Chapter 6, biaxially constrained films were studied to determine what effect changing the mechanical boundary conditions has on tilting within these films. Finally, in Chapter 7, the conclusions for relaxed and strained tilted piezoelectric films are presented.

1.3 *References*

[1]S. Roberts, "Dielectric and piezoelectric properties of barium titanate," *Physical Review,* **71**[12] 890-95 (1947).

[2]R. E. Newnham, "Properties of Materials: Anisotropy, Symmetry, Structure,*"* pp. 392. Oxford University Press: Oxford, NY, (2005).

[3]A. Amin, R. E. Newnham, and L. E. Cross, "Atom shifts, polarization levels, and Curie temperatures in ferroelectric $PbZrO_3$-$PbTiO_3$ solid-solutions," *Materials Research Bulletin,* **15**[6] 721-28 (1980).

[4]M. J. Haun, T. J. Harvin, M. T. Lanagan, Z. Q. Zhuang, S. J. Jang, and L. E. Cross, "Thermodynamic theory of $PbZrO_3$," *Journal of Applied Physics,* **65**[8] 3173-80 (1989).

[5]A. M. Glazer, "Classification of tilted octahedra in perovskites," *Acta Crystallographica Section B-Structural Science,* **B 28**[Nov15] 3384-92 (1972).

[6]R. Eitel, "Novel piezoelectric ceramics: Development of high temperature, high performance, piezoelectrics on the basis of structure" pp.173, Ph.D. thesis in Materials Science and Engineering, The Pennsylvania State University, (2003)

[7]D. I. Woodward, J. Knudsen, and I. M. Reaney, "Review of crystal and domain structures in the $PbZr_xTi_{1-x}O_3$ solid solution," *Physical Review B,* **72**[10] 104110 (2005).

[8]R. E. Eitel, S. J. Zhang, T. R. Shrout, C. A. Randall, and I. Levin, "Phase diagram of the perovskite system (1-x)$BiScO_3$-x$PbTiO_3$," *Journal of Applied Physics,* **96**[5] 2828-31 (2004).

[9]R. R. Duan, R. F. Speyer, E. Alberta, and T. R. Shrout, "High Curie temperature perovskite $BiInO_3$-$PbTiO_3$ ceramics," *Journal of Materials Research,* **19**[7] 2185-93 (2004).

[10]S. J. Zhang, R. Xia, L. Lebrun, D. Anderson, and T. R. Shrout, "Piezoelectric materials for high power, high temperature applications," *Materials Letters,* **59**[27] 3471-75 (2005).

[11]M. Suga, M. Hiratani, C. Okazaki, M. Koguchi, and H. Kakibayashi, "Characterization of hetero-epitaxial PZT capacitor," *Integrated Ferroelectrics,* **18**[1-4] 389-96 (1997).

[12]C. M. Foster, G. R. Bai, R. Csencsits, J. Vetrone, R. Jammy, L. A. Wills, E. Carr, and J. Amano, "Single-crystal $Pb(Zr_xTi_{1-x})O_3$ thin films prepared by metal-organic chemical vapor deposition: Systematic compositional variation of electronic and optical properties," *Journal of Applied Physics,* **81**[5] 2349-57 (1997).

[13]C. B. Eom, R. A. Rao, Q. Gan, K. Wasa, and D. J. Werder, "Single crystal thin films of conductive oxides $SrRuO_3$ and ferroelectric heterostructures," *Integrated Ferroelectrics,* **21**[1-4] 251-61 (1998).

Chapter 2   Literature Review

2.1.1 Perovskite Structure

The perovskite crystal structure is adopted by many materials which are useful for piezoelectric, ferroelectric, and dielectric applications.[1-3]   The perovskite structure is composed of a lattice of corner-sharing, BO_6 oxygen octahedra with a large cation in 12-fold coordination in the available interstices, as shown in Figure 2.1(a). The prototypical paraelectric phase typically observed at elevated temperatures has the cubic $Pm\bar{3}m$ symmetry. The Goldschmidt tolerance factor for perovskites given in Equation 2.1 has been used extensively to predict the stability of potential perovskites.

$$t = \frac{r_A + r_O}{\sqrt{2}(r_B + r_O)} ,$$

Equation 2.1. Goldschmidt tolerance factor

where r_A is the radius of the ion on the A site, r_B is the radius of the ion on the B site and r_O is the radius of oxygen.[4] It was noted that perovskite crystal structure is stable from t = 0.85 to t =1.09.[4,5]

Because of the stability of this crystal structure, a variety of perovskites with distorted coordination polyhedra and lower symmetries are also observed. The symmetry of the crystal structure was noted in many cases to be correlated to tolerance factor. Materials with tolerance factors above 1 are typically tetragonal, while lower tolerance factors are found in materials with rhombohedral, orthorhombic, or monoclinic symmetries.[6-8] Figure 2.1(b) shows common ferroelectric distortions of the perovskite crystal structure.
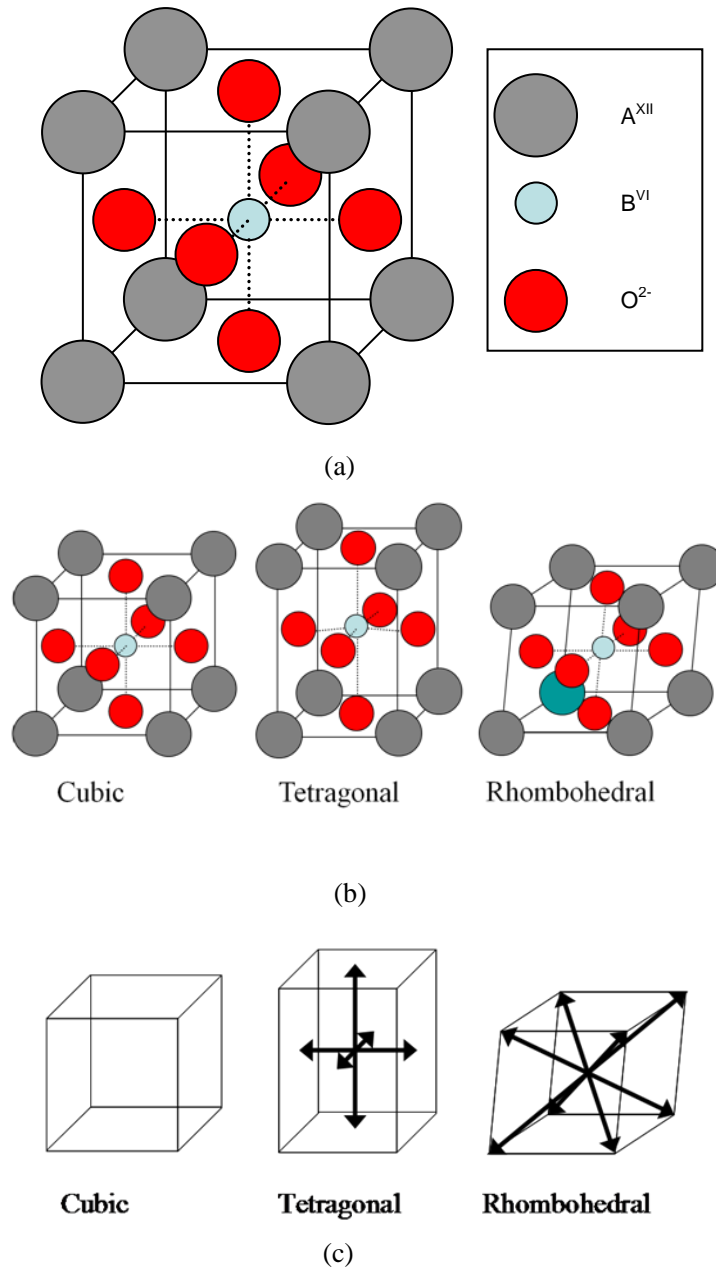
Figure 2.1   Schematic of (a) a perovskite unit cell and (b) cubic, tetragonal, and rhombohedral distortions of the perovskite unit cell. The superscripts for the cations denote their coordination number.   (c) illustrates potential polarization directions for the tetragonal and rhombohedral ferroelectric distortions.

2.2   *Types of Phase Transitions in Perovskites*

2.2.1 Ferroelectric Phase Transitions

Ferroelectric phenomena can arise from two primary sources. In the first type, ferroelectricity develops from an order-disorder transition, where dipoles exist both above and below the transition temperature.[2,9] Above the Curie temperature, T_C, the dipoles are randomized so that no net spontaneous polarization, P_S, exists; below the transition temperature the local dipoles order over long length scales and produce a finite spontaneous polarization. In contrast, in displacive ferroelectrics, ferroelectricity develops when there is a collective displacements of atoms (e.g. by off-centering of ions from a high symmetry position) inducing a dipole moment below T_C.[10] This creates a spontaneous polarization which can be switched to symmetry-equivalent orientations within the unit cell. Above T_C in most displacive ferroelectrics there is there is no off-centering of the cation. This state is the paraelectric prototype state. Displacive ferroelectrics were studied in this thesis, and so they will be discussed in more depth here.

For normal ferroelectrics, the permittivity values do not depend much on frequency below 1 GHz,[11] however they are a strong function of temperature. Peaks in the permittivity appear at polymorphic phase transition temperatures as shown in Figure 2.2 for $BaTiO_3$.[2] As $BaTiO_3$ is cooled from the cubic paraelectric state, it undergoes a transition to a ferroelectric tetragonal state with the polarization along the c-axis. Upon further cooling, the Ti^{4+} displaces along the $[110]_{pc}$ direction in the orthorhombic state

9

and finally along the [111]$_{pc}$ direction in the rhombohedral state. The subscript pc refers

to the prototype cubic state. At T$_C$, permittivities upwards of 10,000 can be obtained.[2,9,12]
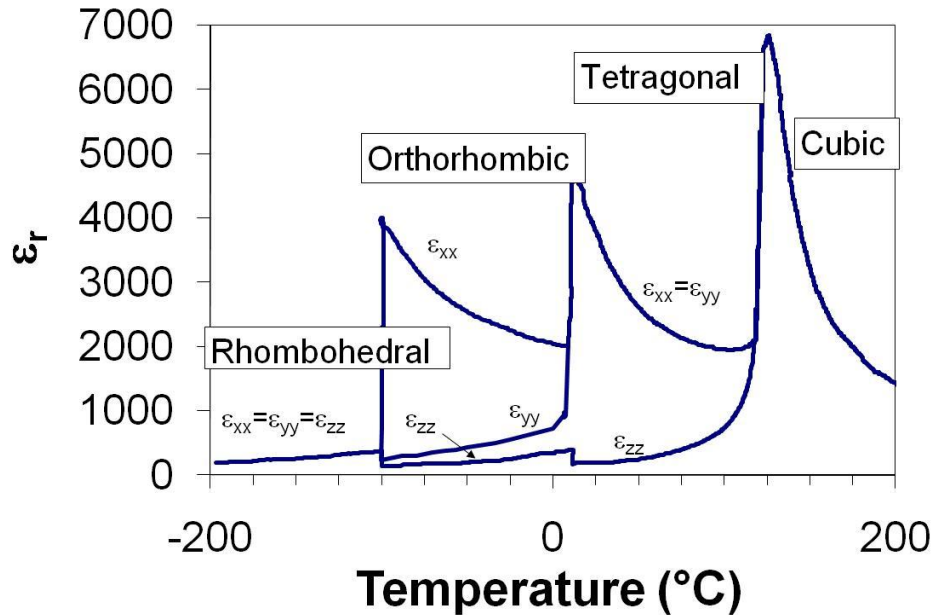
Figure 2.2.   Permittivity vs. temperature for BaTiO$_3$. After Smolenskii.[12]

At temperatures below the Curie temperature, a domain structure will form due to

availability of multiple possible polarization directions.[2,9,12] A domain is a region of

material which possesses a uniform polarization (or at least nearly so). A domain wall is

a boundary between regions with different polarization directions. The number and

orientation of the allowed polarization directions can be determined based on the

symmetry elements lost on the transition from the prototype phase to the ferroelectric

one. The two types of domain walls are a) 180° domain walls, where the polarization

directions of the domains are antiparallel and b) non-180° domain walls, where the two

polarizations differ by another angle. Motion of both 180° and non-180° domain walls contributes to the observed dielectric and piezoelectric properties of ferroelectrics.[2]
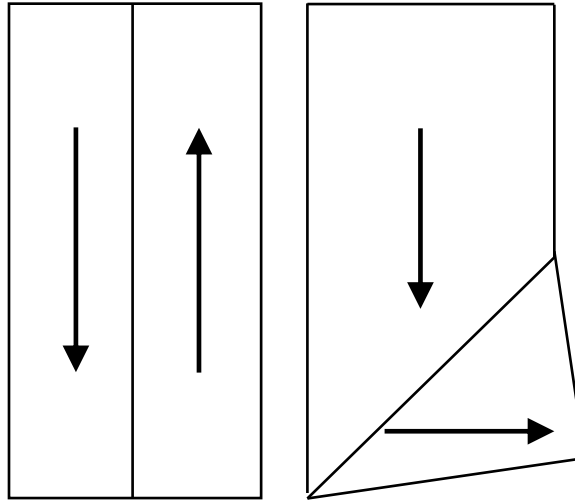
Figure 2.3. Schematic of 180° (left) and non-180° domain walls (right). The arrows denote the polarization direction within the domain.

2.2.2 Antiferroelectric Phase Transitions

A second type of phase transition observed in perovskites is an antiferroelectric phase transition. A well-known antiferroelectric material is $PbZrO_3$.[13,14] For this material, the Pb^{2+} cations on the A-site of the perovskite structure off-center. However, rather than all shifting in the same direction, the cation displacements occurs on two separate sublattices, which cancel out to leave no net polarization for the unit cell. Antiferroelectrics also show a peak in permittivity at phase transitions. However, the polarization – electric field, P-E, loop for an antiferroelectric materials differs drastically from that of a well processed ferroelectric material, as shown in Figure 2.4.

Antiferroelectric materials have doubled hysteresis loops which result from a field-forced phase transition to a ferroelectric phase. It should be noted that this type of double hysteresis loop are distinct from those present just above the Curie temperature in $BaTiO_3$ or pinched loops due to defect dipoles pinning the domains within a ferroelectric.[15,16]
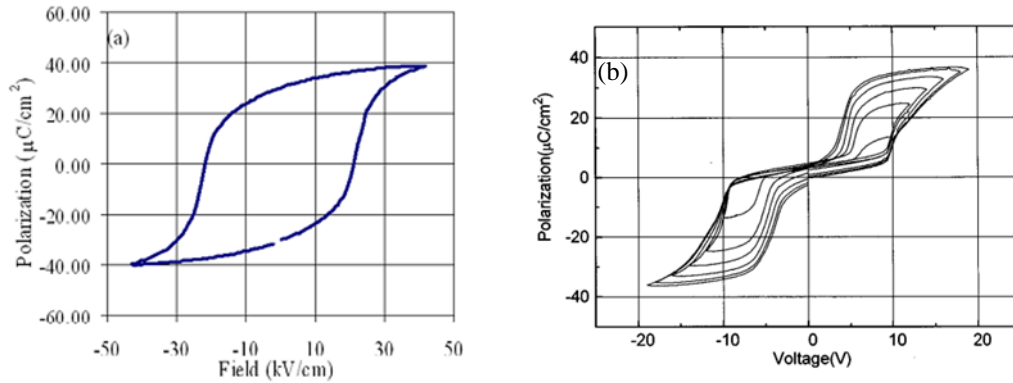
Figure 2.4.   Polarization vs. electric field data for a (a) ferroelectric and (b) antiferroelectric material. [17,18]

2.2.3 Tilt Transitions

The most common type of phase transition in perovskites is due to the rotation of the oxygen octahedra about a specific crystallographic axis to reduce the coordination volume of the A-site cation. The notation used to describe octahedral tilting was first developed by Glazer.[19] Glazer notation describes the phase and relative magnitudes of tilt along the three principle axes, *a*, *b*, and *c* within the unit cell. For directions with the same magnitude of tilt, the letter is repeated. In-phase tilting is characterized by rotation of the oxygen octahedra in successive layers along a specific axis having the same sign; this is noted in Glazer notation as a (+) superscript. For anti-phase tilting, along a

12

specific axis, adjacent layers have tilt angles with opposite signs; in Glazer notation, this is denoted using a superscript (−). If there happens to be no rotation of the oxygen octahedra along a specific axis, then that axis is given the superscript (0). Examples of these three types of tilt are shown in Figure 2.5. Through the various combinations of in-phase, anti-phase, and no tilt, there are a total of 23 possible tilt systems in the perovskite family and later augmented to include various cation displacements.[19-21] These occur in various materials as shown in Table 2.1. Several materials such as $AgNbO_3$, $NaNbO_3$, $KMnF_3$ have multiple tilt transitions.[22-24]
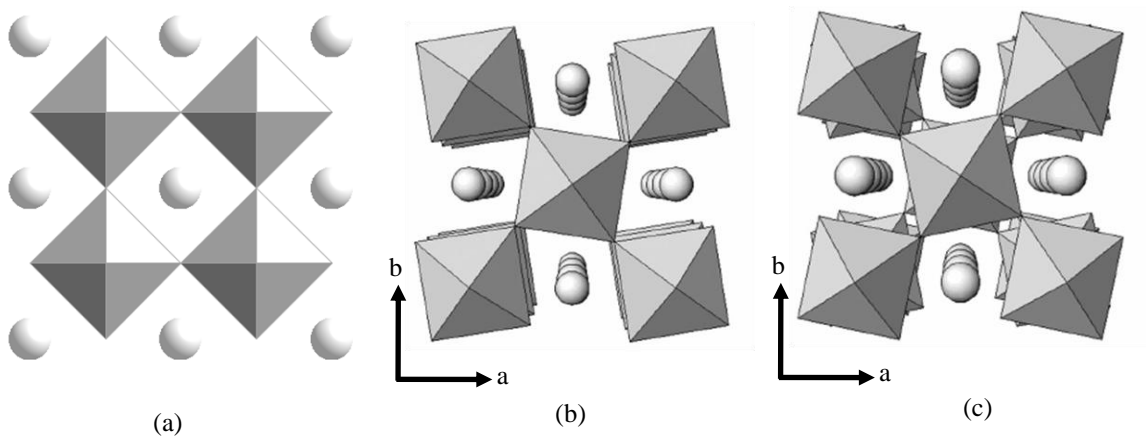
Figure 2.5. Octahedral tilt structures for (a) $a^0a^0a^0$ (b) $a^0a^0c^+$ and (c) $a^0a^0c^-$.[25]

Table 2.1 Tilt systems for common perovskite materials

Material	Tilt system	Space group	Ref:
$CaTiO_3$	$a^-a^-c^+$	Pbnm	[26]
$SrTiO_3$	$a^0a^0c^-$	I4mmm	[19]
$KMnF_3$	$a^0a^0c^-$	F4/mmc	[19]
$NaNbO_3$	$a^0a^0c^+$	C4/mmb	[19]
$DyScO3$	$a^-a^-c^+$	Pbnm	[5]
$LaAlO_3$	$a^-a^-a^-$	$R\bar{3}c$	[27]
$BiFeO_3$	$a^-a^-a^-$	R3c	[28]
$SrRuO_3$	$a^-a^-c^+$	Pbnm	[29]
$LaNiO_3$	$a^-a^-a^-$	$R\bar{3}c$	[19]
$NaMgF_3$	$a^-a^-c^+$	Pbnm	[30]

2.2.4 Incommensurate Phase Transitions

A fourth type of phase transition is an incommensurate phase transition. This occurs when the soft phonon responsible for ferroelectric phase transition condenses at a wavevector which is not a rational descriptor of the unit cell. This has been shown to occur for some ferroelectric displacive transitions.[31] However incommensuration has not been observed in octahedral tilting and will be neglected in this thesis.[32]

2.2.5 Characterizing Phase Transitions

There are several structural indicators of the observed phase transitions in perovskites. First, with the development of a spontaneous polarization, the material

typically elongates along the direction of the polarization and contracts laterally, causing a spontaneous strain.[2,3,33] For a tetragonal distortion, if a polarization develops along the $[001]_{pc}$ direction, the d-spacing for the $[001]_{pc}$ direction increases while the $[100]_{pc}$ and $[010]_{pc}$ contract. This will split the peaks observed in the x-ray diffraction pattern. Peak splitting such as this will occur for different peaks depending on the direction of the polarization.

By performing x-ray or neutron diffraction and monitoring which peaks split when going through the ferroelectric phase transition, it is possible to determine in which direction the spontaneous polarization develops, as well as the temperature dependence of the spontaneous strain. This is seen in Figure 2.6 for the 220_{pc} peak of $Pb(Zr_{0.8}Ti_{0.2})O_3$ powders. At high temperature, the material is in the paraelectric cubic phase (marked by C on the graph). At T_C, the material transforms to a rhombohedral ferroelectric phase labeled by R_{HT} on the graph. At low temperatures, the material undergoes a tilt transition from a tilt system of $a^0a^0a^0$ to $a^-a^-a^-$ and is labeled as R_{LT}. One step that is often performed on bulk ceramic materials is to perform a Rietveld analysis on the diffraction patterns to yield atomic positions. The resulting atomic positions describe ion off-centering and rotation of the oxygen octahedra.[22,29,34,35]
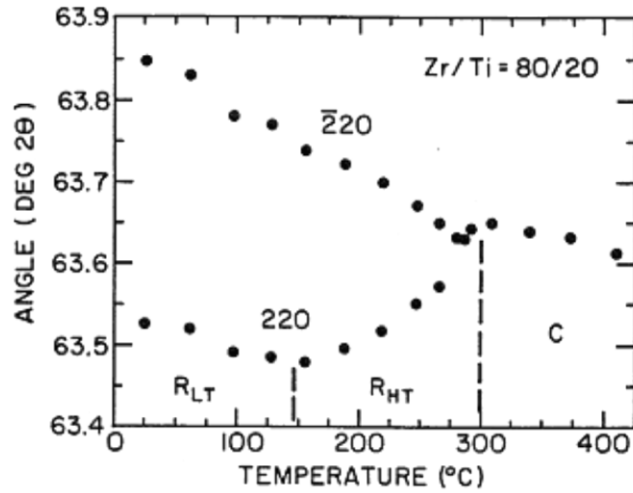
Figure 2.6. Peak splitting of the 220_{pc} peak for $Pb(Zr_{0.8}Ti_{0.2})O_3$ powders. Marked on the graph are the paraelectric–ferroelectric phase transition and the ferroelectric untilted (R_{HT})–ferroelectric tilted(R_{LT}) phase transition.[36]

For antiferrodistortive transitions, the unit cell contains an integer multiple of the formula units as compared with the high temperature unit cell. This can occur through cation displacements as in antiferroelectric distortions, octahedral tilting, magnetic ordering, or a combination thereof.[37] This increase in the unit cell size leads to additional weak reflections in the diffraction pattern associated with the small deviations in the primitive unit cell. For example, in $SrTiO_3$, below the tilt transition the material has the $a^0a^0c^-$ tilt system. In a single domain single crystal or thin film $SrTiO_3$, the superlattice reflection will appear at $\frac{1}{2}\{113\}_{pc}$ location but not the $\frac{1}{2}\{311\}_{pc}$ or $\frac{1}{2}\{131\}_{pc}$ locations. Figure 2.7 shows a reciprocal space map around the 101_{pc} peak of a $AgNbO_3$ thin film. Sol-gel processing was used to deposit the film to ~300 nm thick on (100) $SrTiO_3$. The film was epitaxial as deposited. At the center there is a strong reflection from the $SrTiO_3$

16

substrate and the AgNbO$_3$ thin film. The four weak reflections surrounding are superlattice reflections produced by the film. In AgNbO$_3$, at low temperatures, the material undergoes a transition associated with the shift in all the Nb^{5+} positions along either the $[11l]$ or the $[11\bar{l}]$ directions.[35] Should the long axis of the AgNbO$_3$ film exist solely out of plane of the film, the superlattice reflections should only exist in the direction from the lower left to upper right of the reciprocal space map, whereas if the c-axis was within the plane of the film, the reflections should be in the upper left and lower right. Since reflections are evident at all four positions, it can be concluded that the film has domains with the c-axis pointed both in-plane and out-of-plane of the film. This result is consistent with domain structure seen for other perovskite films.[38]
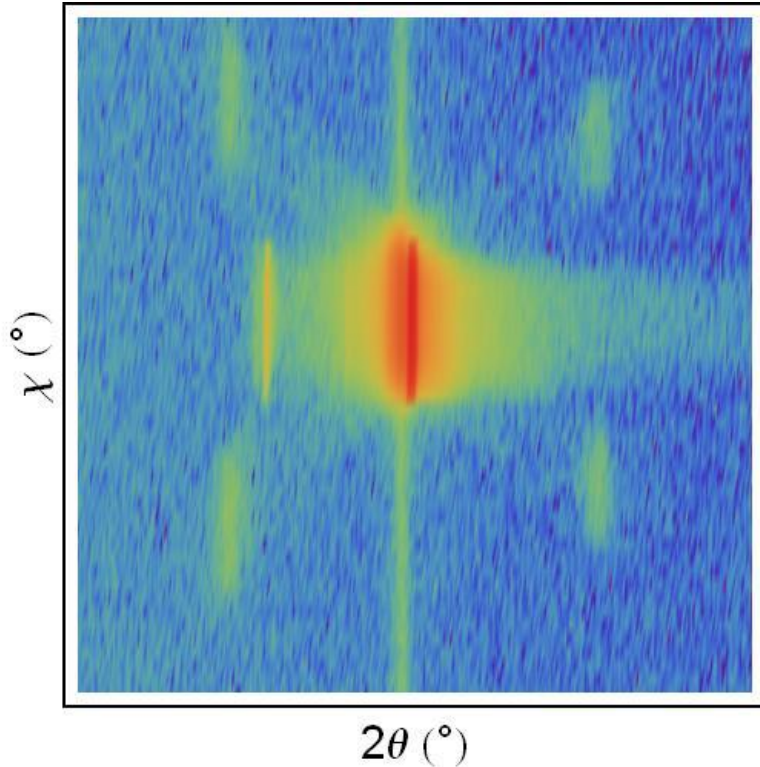
Figure 2.7. Reciprocal space map around the 101_{pc} reflection of $AgNbO_3$ on (100) $SrTiO_3$. Weak reflections result from superlattice reflections.

The intensity of the superlattice reflections for most perovskite materials is on the order of 0.01-1% of the maximum intensity. For films, this makes it difficult to locate the superlattice reflections using lab-source x-ray diffractometers, due to the peaks being at or near the noise floor. Electron diffraction has also shown to be a useful tool for determining the tilt structure of thin films.[39] For tilted perovskites, such reflections enable the determination of the tilt system of a material. For a material with $a^0a^0c^+$ tilt, the unit cell is changed by a rotation of the BO_6 octahedra about the c-axis and leads to a superlattice reflection at a location of $\frac{1}{2}\{ooe\}_{pc}$ where e is an even number, o is an odd

number and h$\neq$k. For a material with a tilt system of $a^0a^0c^-$, the superlattice reflection is found at ½{ooo}$_{pc}$ where h$\neq$k.

Table 2.2 lists the various diffraction conditions required for tilt along specific axes as reported by Glazer.[40] In addition, the superlattice locations for the tilt systems of SrRuO$_3$ and Pb(Zr$_{1-x}$Ti$_x$)O$_3$ are shown.   Using this table, one can assess which superlattice reflections are present for more complicated tilt structures.

Table 2.2. Superlattice reflections for several conditions of octahedral tilting.[39]

Glazer notation	Superlattice location	Conditions	Example Peak Location
a^+	½{eoo}	k$\neq$l	½{013}$_{pc}$
b^+	½{oeo}	h$\neq$l	½{103}$_{pc}$
c^+	½{ooe}	h$\neq$k	½{130}$_{pc}$
a^-	½{ooo}	k$\neq$l	½{131}$_{pc}$
b^-	½{ooo}	h$\neq$l	½{113}$_{pc}$
c^-	½{ooo}	h$\neq$k	½{311}$_{pc}$
$a^-a^-c^+$	½{ooe}	h$\neq$k	½{211}$_{pc}$
	½{ooo}		½{113}$_{pc}$
$a^-a^-a^-$	½{ooo}		½{113}$_{pc}$

2.3 *Piezoelectric Materials*

Piezoelectricity is the ability of certain crystalline materials to develop an electric polarization proportional to an applied mechanical stress. The direct piezoelectric effect is given in Equation 2.2. This material property is used in pressure sensors. The converse piezoelectric effect relates the induced strain to the applied electric field as shown in Equation 2.3:

$$P_i = d_{ijk}\sigma_{jk}$$

Equation 2.2. Direct piezoelectric effect

$$x_{jk} = d_{ijk} E_i$$

Equation 2.3. Converse piezoelectric effect

where P_i is the polarization tensor, E_i is the electric field tensor, σ_{jk} is the stress tensor, x_{jk} is the strain tensor and d_{ijk} is the piezoelectric tensor.

Piezoelectric materials vary widely in composition from quartz crystals, to AlN film resonators, to a wide selection of perovskite materials. Currently the most important piezoelectric ceramic material is $Pb(Zr_{1-x}Ti_x)O_3$. Over the last two decades, large piezoelectric constants have also been demonstrated in several single crystal perovskites.[41]

Phenomenological calculations have shown that octahedral tilting can influence the electrical properties of perovskites, including the intrinsic dielectric permittivity and piezoelectric constants.[42] Figure 2.8(a) shows the total piezoelectric constant measured across the tilt transition for $Pb(Zr_{0.6}Ti_{0.4})O_3$ ceramics.[43] There is a deviation in the piezoelectric constant at the tilt transition. Additionally, Figure 2.8(b) shows a measure of the piezoelectric nonlinearity present as a function of temperature for the same composition. Below the tilt transition temperature, the ferroelectric domain walls show decreased mobility, which limits the extrinsic contribution to the coefficients.
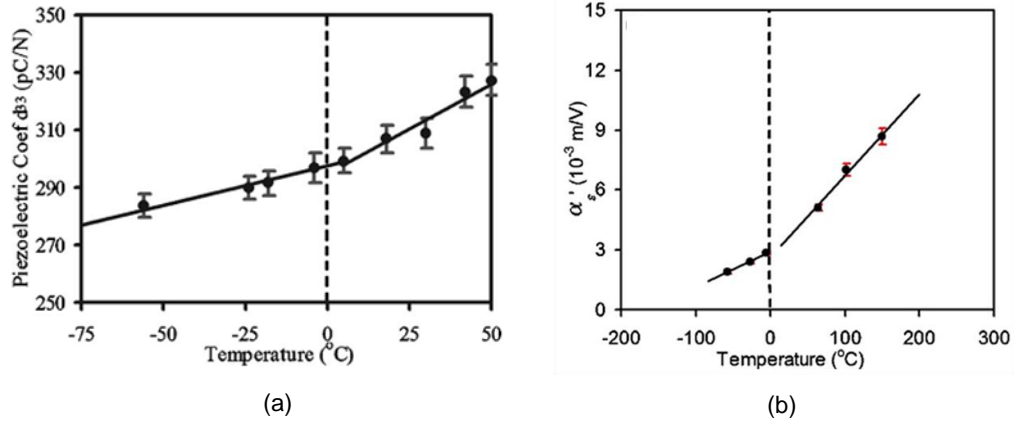
Figure 2.8. (a) Piezoelectric constant and (b) the piezoelectric nonlinearity across the

tilt transition in $Pb(Zr_{0.6}Ti_{0.4})O_3$ ceramics.[43]

A morphotropic phase boundary (MPB) is defined as a nearly temperature

independent boundary in a solid solution phase diagram between two ferroelectric phases

of different composition which differ only in symmetry.[44] In most perovskite solid

solutions, it has been found that morphotropic phase boundaries appear when the

tolerance factor is slightly less than 1.[4] At the morphotropic phase boundary for a

rhombohedral-tetragonal transition, both sets of distortions are possible (the polarization

directions were shown schematically in Figure 2.1(c)). In some cases, a bridging phase,

often a monoclinic distortion, which is a subgroup of the rhombohedral and tetragonal

phases, is observed.[45,46] The larger polarizability of the material at the phase boundary

allows for enhanced properties over its endmembers.[2,47]

2.3.1 Piezoelectric Single Crystals

Perovskite piezoelectric single crystals are important because of their high strain

response and large piezoelectric constants.[41] Typically, single crystal perovskite

piezoelectrics are not utilized at the morphotropic phase boundary. Instead domain

engineering in the rhombohedral phase is used to achieve for high strain associated with polarization rotation within the material.[48,49]   Polarization rotation, shown schematically in Figure 2.9(a), can develop when the electric field is applied along the $[001]_{pc}$ direction. As the field is increased, the polarization rotates from the $<111>_{pc}$ directions to align closer to the electric field direction.[41]   At sufficiently high fields, a transition from the rhombohedral to tetragonal phase can occur as shown in Figure 2.9(a). To avoid the hysteresis associated with this phase transition, single crystals are often chosen with compositions far enough away from the morphotropic phase boundary.[49] However, the existence of tilt transitions near the MPB can complicate materials choice, because these tilt transitions also degrade both the intrinsic and extrinsic contributions to the piezoelectric response.[50] Consequently, it may be difficult to simultaneously avoid both field-induced phase transitions and tilt transitions in potential domain-engineered piezoelectrics.
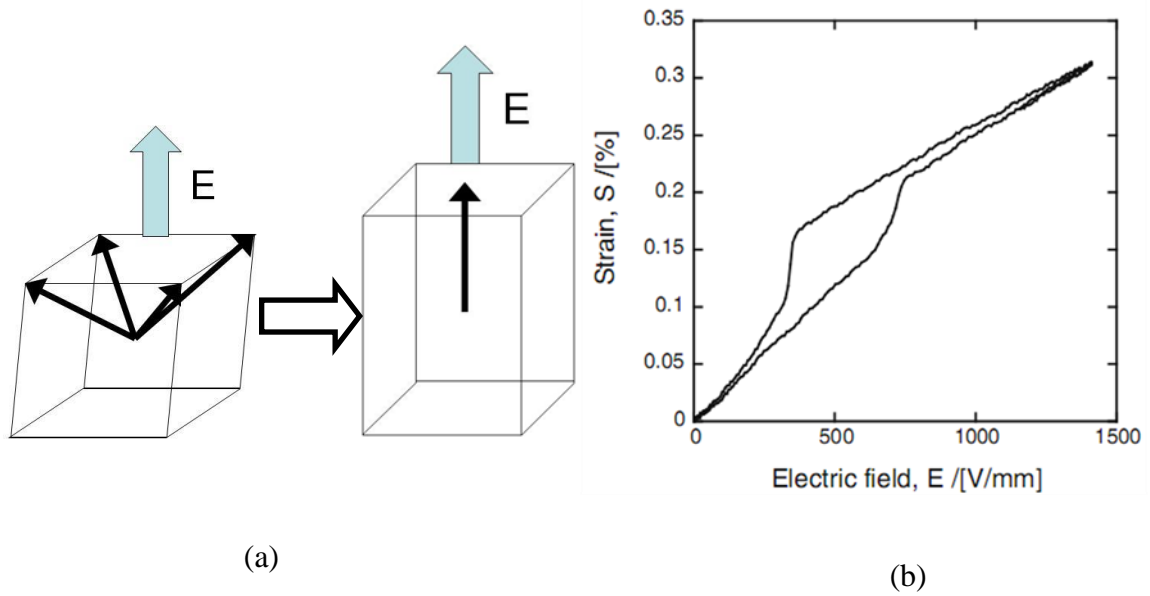
Figure 2.9.   (a) Schematic for polarization rotation in the rhombohedral phase field and (b) strain response to an electric field showing a field induced phase transition from rhombohedral to tetragonal phases in $(001)_{pc}$ oriented $0.69PbMg_{1/3}Nb_{2/3}O_3$-$0.31PbTiO_3$.[51]

One developing field research is for piezoelectric materials which operate at high temperatures. The performance of ferroelectric piezoelectrics degrades at temperatures near T_C due to depoling, so high strain, high temperature piezoelectrics require high T_C materials. High Curie temperatures are favored by materials with end-members with a large difference in tolerance factor. This can be seen for $PbTiO_3$-based solid solutions, as the end-member tolerance factor is reduced, the T_C at the MPB increases (shown in Figure 1.2). However, as the tolerance factor of a perovskite is reduced, the probability

that a tilt phase exists near the MPB increases. Tilted phases existing at compositions near the morphotropic phase boundary may limit the usefulness of domain engineering.

2.3.2 $Pb(Zr_{1-x}Ti_x)O_3$

In $Pb(Zr_{1-x}Ti_x)O_3$, the large size, high polarizability, and 6s-shell electrons of the Pb^{2+} cation leads to large dielectric and piezoelectric constants at the morphotropic phase boundary.[52,53] Recently, transmission electron microscopy was used to review the crystal structure of bulk $Pb(Zr_{1-x}Ti_x)O_3$ across the phase diagram and showed numerous tilt phase, which are reproduced in Figure 2.10(c-e).[54]

The electrical properties measured for bulk ceramics (see Figure 2.10(b)) show that as the composition moves away from the MPB, there is a drop in the dielectric constant of the material. The dielectric constant drops further upon the presence of a tilt phase. Additionally, the electromechanical coupling factor is relatively stable in the rhombohedral phase, but once tilt develops, there is a dramatic decrease. The presence of distorted phases near the MPB indicates that $Pb(Zr_{1-x}Ti_x)O_3$ system is an ideal system to study octahedral tilting in piezoelectric materials. Table 2.3 shows the values for the Curie and tilt transition temperatures of the compositions studied in this thesis.

Table 2.3 Phase transition temperatures for $Pb(Zr_{1-x}Ti_x)O_3$

x	T_C (°C)	T_{Tilt} (°C)
0.2	295	135
0.25	315	115
0.3	333	80
0.35	350	35
0.4	366	-27
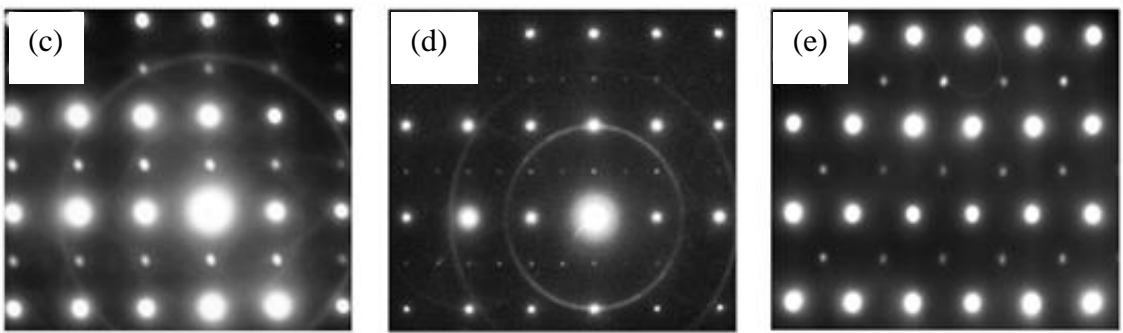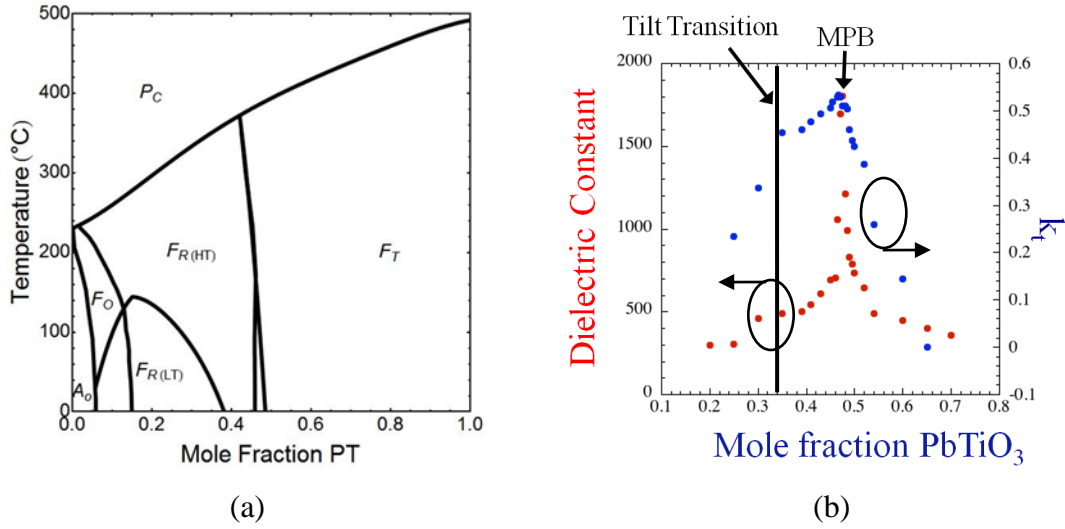
Figure 2.10 (a) Phase diagram for Pb(Zr$_{1-x}$Ti$_x$)O$_3$ (after Woodward, Knudsen, and Reaney)[54] and (b) room temperature permittivity as a function of composition. Electron diffraction patterns from Pb(Zr$_{1-x}$Ti$_x$)O$_3$ with (c) 0.95, (d) x=0.9, and (e) x=0.7. Images were taken with a <110>$_{pc}$ zone axis and show three distinct superlattice reflections.[54] F denotes the ferroelectric phase, A an antiferroelectric phase, and P the paraelectric phase. The subscripts T, M, R, O, and C refer to the tetragonal, monoclinic, rhombohedral, orthorhombic, and cubic phases. LT and RT refer to low temperature and high temperature phases, respectively.

2.4 *Thin Films*

The development of the ferroelectric phase in perovskites involves an increase in the volume of the unit cell. From thermodynamics, we know that high pressure favors low volume states. Thus, by increasing the hydrostatic pressure on most perovskite ferroelectrics, one is able to lower the Curie temperature. This has been done for $BaTiO_3$ as is shown in Figure 2.12(a).[2] Similar studies in thin films show that biaxial strain can change the Curie temperature by over 300°C.[55,56] Figure 2.12(b) shows the predicted Curie temperatures for strained $SrTiO_3$ as calculated by phase-field modeling. This increase can be attributed to the stabilization of the spontaneously polarized phase by the biaxial strain. For films with compressive strain, a spontaneous polarization pointing out of the plane of the film is favored, whereas tensile in-plane strains promote the development of a twinned ferroelectric with the spontaneous polarization in the film plane.[57] It has been shown previously for $PbTiO_3$ thin films that the domain structure of the films can change a function of thickness as a method of relieving stresses.[38]

2.4.1 Epitaxial Growth of Thin Films

Epitaxial growth is where the crystal structure of the grown film has both in-plane and out of plane registry to the substrate.[58,59] For thin films, it is possible to grow films which have in-plane coherent registry to the substrate, i.e., the in-plane lattice parameter of the film is identical to that of the substrate. These types of films are called coherently strained films. In order to grow high quality coherently strained epitaxial films, the difference between the lattice parameters of the substrate and film must be small at

growth temperatures, and the surface energies of the film and the substrate should be comparable. The amount of strain experienced by the films can be determined by calculating the lattice mismatch, f, between the film and substrate Equation 2.4,

$$f = \frac{(a_f - a_s)}{(a_f + a_s)/2} \approx (a_f - a_s)/a_s ,$$

Equation 2.4. Lattice mismatch for thin films

where a_f and a_s are film and substrate lattice parameters respectively.[58,59] At small thicknesses, there is a competition between the strain energy of the film, and the strain energy associated with the introduction of dislocations. The Matthews-Blakeslee criterion describes the relationship between the critical thickness for a coherent film, h, and the strain, ε, is expressed in Equation 2.5,

$$\varepsilon = \frac{b}{8h\pi(1+v)} \ln(\frac{4h}{b}) ,$$

Equation 2.5. Matthews-Blakeslee criterion

where b is the Burgers vector and v is the Poisson's ratio.[58] Above this critical thickness, misfit dislocations are thermodynamically favored to relieve the stress of the films.

During the initial stages of epitaxial deposition, the lattice of the epitaxial layer will constrain itself to the lattice of the substrate, as shown schematically in Figure 2.11(a) and Figure 2.11(b). Being constrained to the substrate, the film is under stress in the plane of the film, i.e., the x and y directions. As mentioned before, epitaxial films remain strained to the substrate until a critical thickness is reached. Upon passing that, films begin to form misfit dislocations as shown schematically in Figure 2.11(c).
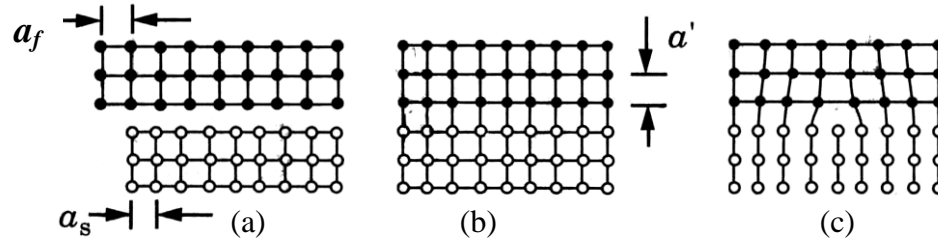
Figure 2.11 Schematic of lattice mismatch between film and substrate (a) film and substrate lattices prior to deposition, (b) film lattice constrained to substrate, and (c) misfit dislocation relieving stress in the film. After Smith.[58]

2.4.2 Effect of Mechanical Constraints on Phase Transitions

The development of the ferroelectric phase involves an increase in the volume of the perovskite unit cell. From thermodynamics, we know that high pressure favors low volume states. Thus, by increasing the hydrostatic pressure on most perovskite ferroelectrics, one is able to lower the Curie temperature. This has been done for $BaTiO_3$ as is shown in Figure 2.12(a).[2] Similar studies in thin films show that biaxial strain can change the Curie temperature by over 300°C.[55,56] Figure 2.12(b) shows the predicted Curie temperatures for strained $SrTiO_3$ as calculated by phase-field modeling. This increase can be attributed to the stabilization of the spontaneously polarized phase by the biaxial strain. For films with compressive strain, a spontaneous polarization pointing out of the plane of the film is favored, whereas tensile in-plane strains promote the development of a twinned ferroelectric with the spontaneous polarization in the film plane.[57] It has been shown previously for $PbTiO_3$ thin films that the domain structure of the films changes as a function of thickness as a method of relieving stresses.[38]

(a)	(b)
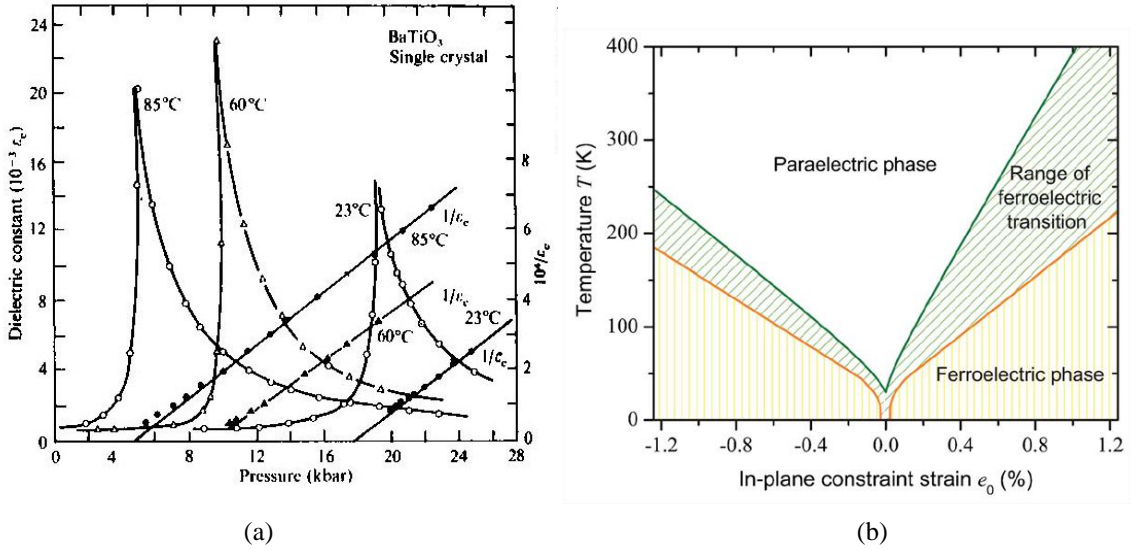
Figure 2.12. (a) Dielectric constant as a function of hydrostatic pressure for $BaTiO_3$ showing pressure-induced changes in the ferroelectric phase transition[2] and (b) theoretical phase diagram for $SrTiO_3$ showing how stress can induce a ferroelectric phase in a material.[60]

As mentioned in section 2.2.3, the tilt transition lowers the A-site coordination volume. The volume of the tilted cell is lower than that of the untilted one, and therefore it is favored at higher hydrostatic pressures.[61,62] This result is not surprising since thermodynamics favors low volume phases at high pressure. The relative stability of octahedrally tilted phases is less clear for other strain conditions. Recent research shows that the tilt transition for $SrTiO_3$ depends on the biaxial strain.[60,63,64] Phase field modeling done for $SrTiO_3$ suggests that the tilt transition is weakly coupled with the strain, however uncertainty in the stiffness and rotostrictive constants leads to uncertainty

in the calculations, as evidenced by the shaded regions in Figure 2.13.[60] Figure 2.13 also shows experimental data for the tilt transition temperature measured for $SrTiO_3$ thin films. In-plane tensile strain appears to increase the tilt transition temperature for the films; however, T_{Tilt} is not strongly strain dependent for strains above ~ 0.25%. Compressive strain, however, seems to have a more significant impact on the tilt transition temperature. It is intriguing that the measured strain dependence considerably exceeds the prediction from phenomenological models.
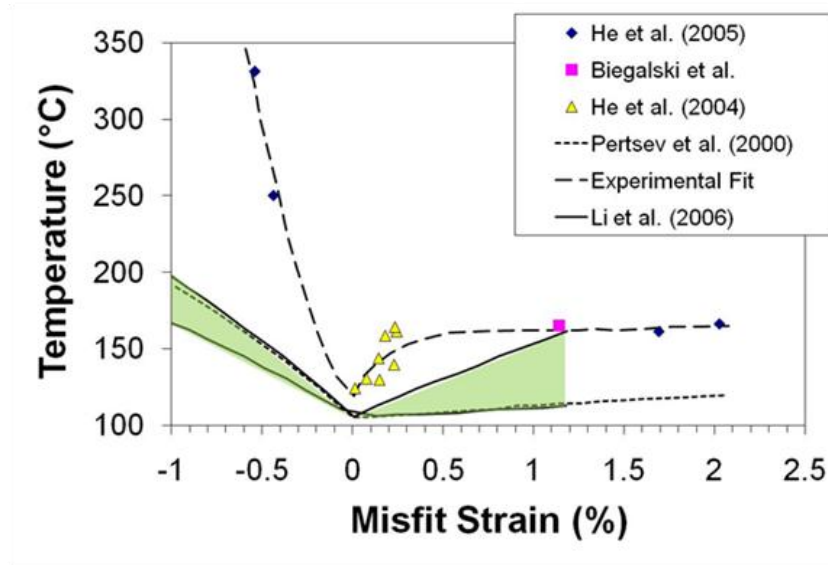
Figure 2.13. Tilt transition temperature as a function of strain for $SrTiO_3$ thin films. A combination of experimental data[57,63,64] and phenomenological modeling[60,65] is included. Above the line, the material is untilted; below the line a tilted phase is favored. Shaded regions indicate uncertainty in the calculated tilt transition temperature based on uncertainty in the material constants for $SrTiO_3$.[60]

First principle studies on biaxially strained $(001)_{pc}$ $LaAlO_3$ also suggest that the tilt angle is dependent on the strain as shown in Figure 2.14(a).[66] Here the authors define

"tilt" to be the rotation of the oxygen octahedra within the plane of the film, whereas "rotation" is the rotation of oxygen octahedra about the $[001]_{pc}$ (e.g. out of the film plane). The development of a rotation about a specific direction results in a corresponding elastic strain. Rotation about the c-axis reduces the lattice a and b lattice parameters. Thus, if a $(001)_{pc}$ oriented film was under biaxial compressive strain, the material would favor a state with smaller in-plane lattice parameters − a rotated phase. This result is consistent with what was measured for $(001)_{pc}$ LaNiO$_3$ thin films where the in-plane angles were not sensitive to strain, whereas the out-of-plane rotation was strongly sensitive to strain.[67]   Figure 2.14(b) shows the tilt angle calculated by density functional theory (DFT) using the experimentally recorded lattice parameters, where γ is the rotation angle along the $[001]_{pc}$ and α is the rotation angle along the $[100]_{pc}$. Additionally, due to coherency of the films, the Ni-O bond length was observed to change (Figure 2.14) with applied strain as evidenced by the (DFT) calculations from experimental lattice parameters. These studies indicate that it may not be possible to eliminate octahedral tilting using strain, however, they leave open questions such as, how does strain affect the tilt transition temperature, and how the distortion of the oxygen octahedra affects the measured properties of the films.
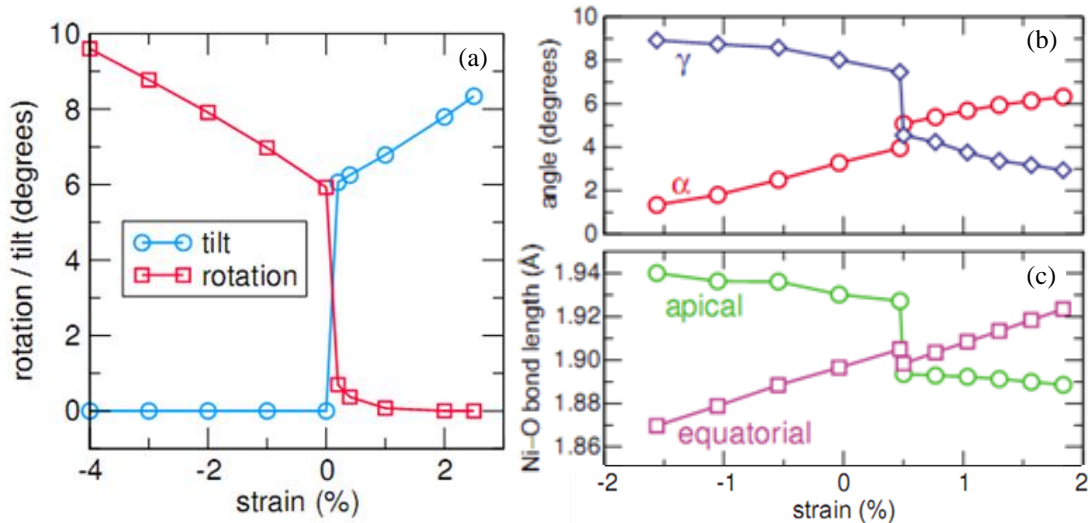
Figure 2.14. Tilt angle as a function of strain for LaAlO₃[66] and (b) oxygen shift

parameter (δ_O) and center of oxygen octahedra shift parameter (δ_C) for

LaAlO$_3$/SrTiO$_3$ superlattices.[68]

Other factors such as interfaces have also been shown to influence the tilt state of

the material.[69] For example, in PbTiO$_3$ thin films, the surface has been shown to undergo

a reconstruction to a $(\sqrt{2} \times \sqrt{2})R45°$ state.[69] This arises due to the oxygen atoms within

the top-most unit cell undergoing a rotation along [001]. As a result, the repeat unit for

the surface of the film rotates by 45° with respect to the [100]. The new surface unit cell

is shown in Figure 2.15(a). In the figure, the underlying square shows the orientation of

the underlying PbTiO$_3$ unit cells, and illustrates the displacement of the oxygen ions.

Additionally, it has been shown in superlattices the tilt can propagate across interfaces.[68]

Aberration-corrected transmission electron microscopy was performed using

negative spherical aberration imaging and high angle annular dark field imaging was

obtained for a SrTiO$_3$/LaAlO$_3$/SrTiO$_3$ superlattice. Intensity profiles were obtained from

the images and the lattice parameter were calculated for each unit cell across the

superlattice; this is plotted in Figure 2.15(b). There is no apparent change in lattice parameter in the $SrTiO_3$ layers leading up to the interface. The shift of the oxygen ions was calculated and the oxygen shift parameter (δ_O) is shown in Figure 2.15(c). The $LaAlO_3$ layer showed a strong shift in the oxygen positions. Interestingly, the shift in oxygen positions was observed to extend several unit cells deep into the $SrTiO_3$ layers. While, there is observable tilt within the first several unit cells of $SrTiO_3$, there is no observable change in the lattice parameter of the $SrTiO_3$ layers.
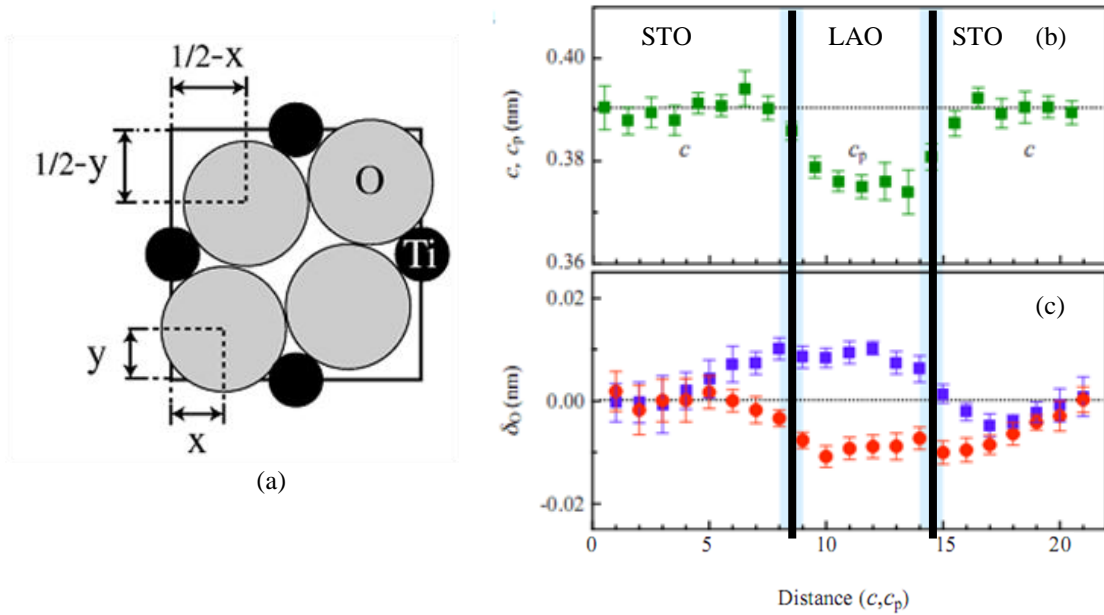
Figure 2.15.   (a) Schematic of the $PbTiO_3$ surface showing an antiferrodistortive reconstruction; (b) lattice parameter as a function of position for $SrTiO_3/LaAlO_3/SrTiO_3$ superlattice and oxygen shift parameter (δ_O) for $LaAlO_3/SrTiO_3$ superlattices.[68]   The vertical black lines in (b) and (c) indicate the location of the $SrTiO_3/LaAlO_3$ interface.

2.5 *References:*

[1]B. Jaffe, W. R. Cook Jr., and H. Jaffe, "Piezoelectric Ceramics," pp. 317. Academic Press Ltd. : New York, (1971).

[2]M. E. Lines and A. M. Glass, "Principles and Applications of Ferroelectrics and Related Materials," pp. 680. Oxford University Press: Oxford, NY, (1977).

[3]F. Jona and G. Shirane, "Ferroelectric Crystals," pp. 402. Dover Publications, Inc.: Mineola, New York, (1962).

[4]R. E. Eitel, C. A. Randall, T. R. Shrout, P. W. Rehrig, W. Hackenberger, and S. E. Park, "New high temperature morphotropic phase boundary piezoelectrics based on Bi(Me)O_3-PbTiO_3 ceramics," *Japanese Journal of Applied Physics Part 1-Regular Papers Short Notes & Review Papers,* **40**[10] 5999-6002 (2001).

[5]M. D. Biegalski, J. H. Haeni, S. Trolier-McKinstry, D. G. Schlom, C. D. Brandle, and A. J. Ven Graitis, "Thermal expansion of the new perovskite substrates DySCO_3 and GdSCO_3," *Journal of Materials Research,* **20**[4] 952-58 (2005).

[6]V. A. Isupov, "Causes of Different Symmetry Ferroelectric Phase in Perovskite Type Ferroelectrics," *Fizika Tverdogo Tela,* **26**[1] 243-45 (1984).

[7]T. R. Shrout and A. Halliyal, "Preparation of Lead-Based Ferroelectric Relaxors for Capacitors," *American Ceramic Society Bulletin,* **66**[4] 704-11 (1987).

[8]O. Furukawa, Y. Yamashita, M. Harata, T. Takahashi, and K. Inagaki, "Dielectric-Properties of Modified Lead Zinc Niobate Ceramic," *Japanese Journal of Applied Physics Part 1-Regular Papers Short Notes & Review Papers,* **24** 96-99 (1985).

[9]F. Jona and G. Shirane, "Ferroelectric Crystals," pp. 402. Dover Publications, Inc.: Mineola, New York, (1993).

[10]R. E. Newnham, "Properties of Materials: Anisotropy, Symmetry, Structure," pp. 392. Oxford University Press: Oxford, NY, (2005).

[11]L. Jin, V. Porokhonskyy, and D. Damjanovic, "Domain wall contributions in $Pb(Zr,Ti)O_3$ ceramics at morphotropic phase boundary: A study of dielectric dispersion," *Applied Physics Letters,* **96**[24] - (2010).

[12]G. A. Smolenskii, V. A. Bokov, V. A. Isupov, N. N. Krainik, R. E. Pasynkov, and A. I. Sokolov, "Ferroelectrics and Related Materials," pp. 763 **Vol. 3**. Gordon and Breach Science Publishers: New York, NY, (1984).

[13]F. Jona, G. Shirane, F. Mazzi, and R. Pepinsky, "X-Ray and Neutron Diffraction Study of Antiferroelectric Lead Zirconate, $PbZrO_3$," *Physical Review,* **105**[3] 849-56 (1957).

[14]M. J. Haun, T. J. Harvin, M. T. Lanagan, Z. Q. Zhuang, S. J. Jang, and L. E. Cross, "Thermodynamic theory of $PbZrO_3$," *Journal of Applied Physics,* **65**[8] 3173-80 (1989).

[15]W. J. Merz, "Double Hysteresis Loop of $BaTiO_3$ at the Curie Point," *Physical Review,* **90**[2] 513-17 (1953).

[16]S. K. Pandey, O. P. Thakur, A. Kumar, C. Prakash, R. Chatterjee, and T. C. Goel, "Study of pinched loop characteristics of lead zirconate titanate (65/35)," *Journal of Applied Physics,* **100**[1] 014104 (2006).

[17]R. Eitel, "Novel piezoelectric ceramics: Development of high temperature, high performance, piezoelectrics on the basis of structure" pp.173, Ph.D. thesis in Materials Science and Engineering, The Pennsylvania State University, (2003)

[18]K. Yamakawa, S. Trolier-McKinstry, J. P. Dougherty, and S. B. Krupanidhi, "Reactive Magnetron Co-Sputtered Antiferroelectric Lead Zirconate Thin-Films," *Applied Physics Letters,* **67**[14] 2014-16 (1995).

[19]A. M. Glazer, "Classification of tilted octahedra in perovskites," *Acta Crystallographica Section B-Structural Science,* **B 28**[Nov15] 3384-92 (1972).

[20]H. T. Stokes, E. H. Kisi, D. M. Hatch, and C. J. Howard, "Group-theoretical analysis of octahedral tilting in ferroelectric perovskites," *Acta Crystallographica Section B-Structural Science,* **58** 934-38 (2002).

[21]C. J. Howard and H. T. Stokes, "Octahedral tilting in cation-ordered perovskites - a group-theoretical analysis," *Acta Crystallographica Section B-Structural Science,* **60** 674-84 (2004).

[22]P. Sciau, A. Kania, B. Dkhil, E. Suard, and A. Ratuszna, "Structural investigation of $AgNbO_3$ phases using x-ray and neutron diffraction," *Journal of Physics-Condensed Matter,* **16**[16] 2795-810 (2004).

[23]G. Shirane, R. Newnham, and R. Pepinsky, "Dielectric Properties and Phase Transitions of $NaNbO_3$ and $(Na,K)NbO_3$," *Physical Review,* **96**[3] 581-88 (1954).

[24]S. M. Shapiro, G. Shirane, J. D. Axe, and T. Riste, "Critical Scattering in $SrTiO_3$ and $KMnF_3$," *Bulletin of the American Physical Society,* **17**[3] 277-& (1972).

[25]M. W. Lufaso and P. M. Woodward, "Prediction of the crystal structures of perovskites using the software program SPuDS," *Acta Crystallographica Section B-Structural Science,* **57** 725-38 (2001).

[26]B. J. Kennedy, C. J. Howard, and B. C. Chakoumakos, "Phase transitions in perovskite at elevated temperatures - a powder neutron diffraction study," *Journal of Physics-Condensed Matter,* **11**[6] 1479-88 (1999).

[27]J. D. Axe, G. Shirane, and K. A. Mueller, "Zone-boundary phonon instability in cubic $LaAlO_3$," *Bulletin of the American Physical Society,* **14**[1] 61-68 (1969).

[28]D. I. Woodward, I. M. Reaney, R. E. Eitel, and C. A. Randall, "Crystal and domain structure of the $BiFeO_3$-$PbTiO_3$ solid solution," *Journal of Applied Physics,* **94**[5] 3313-18 (2003).

[29]B. J. Kennedy, B. A. Hunter, and J. R. Hester, "Synchrotron x-ray diffraction reexamination of the sequence of high-temperature phases in $SrRuO_3$," *Physical Review B,* **65**[22] 224103 (2002).

[30]H. Z. Liu, J. Chen, J. Hu, C. D. Martin, D. J. Weidner, D. Hausermann, and H. K. Mao, "Octahedral tilting evolution and phase transition in orthorhombic $NaMgF_3$ perovskite under pressure," *Geophysical Research Letters,* **32**[4] L04304 (2005).

[31]C. A. Randall, S. A. Markgraf, A. S. Bhalla, and K. Babakishi, "Incommensurate Structures in Highly Ordered Complex Perovskites $Pb(Co_{1/2}W_{1/2})O_3$ and $Pb(Sc_{1/2}Ta_{1/2})O_3$," *Physical Review B,* **40**[1] 413-16 (1989).

[32]I. P. Swainson, "Tilt and acoustic instabilities in ABX_4, A_2BX_4 and ABX_3 perovskite structure types: their role in the incommensurate phases of the organic-inorganic

perovskites," *Acta Crystallographica Section B-Structural Science,* **61** 616-26 (2005).

[33]J. Grindlay, "An introduction to the phenomenological theory of ferroelectricity,*"* pp. 255 1st ed. Pergamon Press: New York, New York, (1970).

[34]D. L. Corker, A. M. Glazer, R. W. Whatmore, A. Stallard, and F. Fauth, "A neutron diffraction investigation into the rhombohedral phases of the perovskite series $PbZr_{1-x}Ti_xO_3$," *Journal of Physics-Condensed Matter,* **10**[28] 6251-69 (1998).

[35]I. Levin, V. Krayzman, J. C. Woicik, J. Karapetrova, T. Proffen, M. G. Tucker, and I. M. Reaney, "Structural changes underlying the diffuse dielectric response in $AgNbO_3$," *Physical Review B,* **79**[10] 104113 (2009).

[36]M. J. Haun, "Thermodynamic theory of the lead zirconate-titante solid solution system" pp.158, Ph.D. thesis in Solid State Science, The Pennsylvania State University, (1988)

[37]B. Dabrowski, M. Avdeev, O. Chmaissem, S. Kolesnik, P. W. Klamut, M. Maxwell, and J. D. Jorgensen, "Freezing of octahedral tilts below the Curie temperature in $SrRu_{1-v}O_3$ perovskites," *Physical Review B,* **71**[10] 104411 (2005).

[38]C. D. Theis, "Investigation of growth and domain structure of epitaxial lead titanate thin films" pp.114, M.S. thesis in Materials Science and Engineering, The Pennsylvania State University, (1996)

[39]D. I. Woodward and I. M. Reaney, "Electron diffraction of tilted perovskites," *Acta Crystallographica Section B-Structural Science,* **61** 387-99 (2005).

[40]A. M. Glazer, "Simple ways of determining perovskite structures," *Acta Crystallographica Section A,* **31**[Nov1] 756-62 (1975).

[41]S. E. Park and T. R. Shrout, "Ultrahigh strain and piezoelectric behavior in relaxor based ferroelectric single crystals," *Journal of Applied Physics,* **82**[4] 1804-11 (1997).

[42]M. J. Haun, E. Furman, T. R. Halemane, and L. E. Cross, "Thermodynamic theory of the lead zirconate-titanate Solid-solution system, .4. Tilting of the oxygen octahedra," *Ferroelectrics,* **99** 55-62 (1989).

[43]R. Eitel and C. A. Randall, "Octahedral tilt-suppression of ferroelectric domain wall dynamics and the associated piezoelectric activity in $Pb(Zr,Ti)O_3$," *Physical Review B,* **75**[9] (2007).

[44]"An American National Standard IEEE Standard Definitions of Terms Associated with Ferroelectric and Related Materials," *IEEE Transactions on Ultrasonics, Ferroelectrics, and Frequency Control,* **50**[12] 1-32 (2003).

[45]B. Noheda, D. E. Cox, G. Shirane, J. A. Gonzalo, L. E. Cross, and S. E. Park, "A monoclinic ferroelectric phase in the $Pb(Zr_{1-x}Ti_x)O_3$ solid solution," *Applied Physics Letters,* **74**[14] 2059-61 (1999).

[46]B. Noheda, D. E. Cox, and G. Shirane, "Low symmetry phases in piezoelectric systems: PZN-xPT single crystal and powder," *Ferroelectrics,* **267** 147-55 (2002).

[47]Y. Inaguma, A. Miyaguchi, M. Yoshida, T. Katsumata, Y. Shimojo, R. P. Wang, and T. Sekiya, "High-pressure synthesis and ferroelectric properties in perovskite-type $BiScO_3$-$PbTiO_3$ solid solution," *Journal of Applied Physics,* **95**[1] 231-35 (2004).

[48]M. Davis, D. Damjanovic, D. Hayem, and N. Setter, "Domain engineering of the transverse piezoelectric coefficient in perovskite ferroelectrics," *Journal of Applied Physics,* **98**[1] - (2005).

[49]D. Damjanovic, M. Budimir, M. Davis, and N. Setter, "Piezoelectric anisotropy: Enhanced piezoelectric response along nonpolar directions in perovskite crystals," *Journal of Materials Science,* **41**[1] 65-76 (2006).

[50]I. M. Reaney, "Octahedral tilting, domain structure and piezoelectricity in perovskites and related ceramics," *Journal of Electroceramics,* **19**[1] 1-8 (2007).

[51]M. Davis, "Picturing the elephant: Giant piezoelectric activity and the monoclinic phases of relaxor-ferroelectric single crystals," *Journal of Electroceramics,* **19**[1] 23-45 (2007).

[52]R. Seshadri and N. A. Hill, "Visualizing the role of Bi 6s "Lone pairs" in the off-center distortion in ferromagnetic $BiMnO_3$," *Chemistry of Materials,* **13**[9] 2892-99 (2001).

[53]J. Iniguez, D. Vanderbilt, and L. Bellaiche, "First-principles study of $(BiScO_3)_{(1-x)}$-$(PbTiO_3)_{(x)}$ piezoelectric alloys," *Physical Review B,* **67**[22] 224107 (2003).

[54]D. I. Woodward, J. Knudsen, and I. M. Reaney, "Review of crystal and domain structures in the $PbZr_xTi_{1-x}O_3$ solid solution," *Physical Review B,* **72**[10] 104110 (2005).

[55]M. D. Biegalski, Y. Jia, D. G. Schlom, S. Trolier-McKinstry, S. K. Streiffer, V. Sherman, R. Uecker, and P. Reiche, "Relaxor ferroelectricity in strained epitaxial

SrTiO$_3$ thin films on DyScO$_3$ substrates," *Applied Physics Letters,* **88**[19] 192907 (2006).

[56]K. J. Choi, M. Biegalski, Y. L. Li, A. Sharan, J. Schubert, R. Uecker, P. Reiche, Y. B. Chen, X. Q. Pan, V. Gopalan, L. Q. Chen, D. G. Schlom, and C. B. Eom, "Enhancement of ferroelectricity in strained BaTiO$_3$ thin films," *Science,* **306**[5698] 1005-09 (2004).

[57]M. Biegalski, "Epitaxially Strained Strontium Titanate" pp.209, Ph.D. thesis in Materials Science and Engineering, The Pennsylvania State University, (2006)

[58]D. L. Smith, "Thin-Film Deposition: Principles & Practice,*"* pp. 616. McGraw-Hill, Inc., (1995).

[59]M. Ohring, "Materials Science of Thin Films: Deposition & Structure,*"* pp. 794. Academic Press: San Diego, CA, (2002).

[60]Y. L. Li, S. Choudhury, J. H. Haeni, M. D. Biegalski, A. Vasudevarao, A. Sharan, H. Z. Ma, J. Levy, V. Gopalan, S. Trolier-McKinstry, D. G. Schlom, Q. X. Jia, and L. Q. Chen, "Phase transitions and domain structures in strained pseudocubic (100) SrTiO$_3$ thin films," *Physical Review B,* **73**[18] 184112 (2006).

[61]J. Rouquette, J. Haines, V. Bornand, M. Pintard, P. Papet, and F. A. Gorelli, "Pressure-induced low symmetry phases in Ti-rich lead zirconate titanate PbZr$_{0.20}$Ti$_{0.80}$O$_3$," *Journal of the European Ceramic Society,* **25**[12] 2393-96 (2005).

[62]K. A. Muller, W. Berlinger, and J. C. Slonczewski, "Order Parameter and Phase Transitions of Stressed SrTiO$_3$," *Physical Review Letters,* **25**[11] 734-37 (1970).

[63]F. Z. He, B. O. Wells, Z. G. Ban, S. P. Alpay, S. Grenier, S. M. Shapiro, W. D. Si, A. Clark, and X. X. Xi, "Structural phase transition in epitaxial perovskite films," *Physical Review B,* **70**[23] 235405 (2004).

[64]F. Z. He, B. O. Wells, and S. M. Shapiro, "Strain phase diagram and domain orientation in SrTiO3 thin films," *Physical Review Letters,* **94**[17] - (2005).

[65]N. A. Pertsev, A. K. Tagantsev, and N. Setter, "Phase transitions and strain-induced ferroelectricity in SrTiO3 epitaxial thin films," *Physical Review B,* **61**[2] R825-R29 (2000).

[66]A. J. Hatt and N. A. Spaldin, "Competition between polar distortions and octahedral rotations in epitaxially strained $LaAlO_3$," *Condensed Matter-Materials Science,* **3792**[1] (2008).

[67]S. J. May, J. W. Kim, J. M. Rondinelli, E. Karapetrova, N. A. Spaldin, A. Bhattacharya, and P. J. Ryan, "Quantifying octahedral rotations in strained perovskite oxide films," *Physical Review B,* **82**[1] - (2010).

[68]C. L. Jia, S. B. Mi, M. Faley, U. Poppe, J. Schubert, and K. Urban, "Oxygen octahedron reconstruction in the $SrTiO_3/LaAlO_3$ heterointerfaces investigated using aberration-corrected ultrahigh-resolution transmission electron microscopy," *Physical Review B,* **79**[8] 081405 (2009).

[69]A. Munkholm, S. K. Streiffer, M. V. R. Murty, J. A. Eastman, C. Thompson, O. Auciello, L. Thompson, J. F. Moore, and G. B. Stephenson, "Antiferrodistortive reconstruction of the $PbTiO_3$ (001) surface," *Physical Review Letters,* **88**[1] 016101 (2002).

Chapter 3   Experimental Procedure

This chapter discusses the procedures used to grow and characterize relaxed and strained $Pb(Zr_{1-x}Ti_x)O_3$ thin films. An overview of the compositions explored, and target preparation is given. The pulsed laser deposition system used in this thesis is described, along with the deposition parameters utilized. The resulting films were characterized structurally by x-ray diffraction, transmission electron microscopy (TEM) and optical techniques. Lastly, the procedure for electrical measurements, including top electrode definition and the equipment employed for low and high field dielectric measurements is described.

3.1 *$Pb(Zr_{1-x}Ti_x)O_3$ Phase Diagram*

This thesis was directed towards studying phase transitions, particularly those involving octahedral tilting in $Pb(Zr_{1-x}Ti_x)O_3$ (PZT) thin films. Figure 3.1 shows the PZT phase diagram adapted from Woodward, Knudsen and Reaney.[1] $Pb(Zr_{1-x}Ti_x)O_3$ is a solid solution between the orthorhombic anti-ferroelectric $PbZrO_3$ and the tetragonal ferroelectric $PbTiO_3$. At high $PbTiO_3$ contents, the material remains tetragonal. At x=0.48, there is a morphotropic phase boundary (MPB) between the rhombohedral and tetragonal phases, with a wedge of monoclinic distortion at the MPB. At higher Zr compositions, (0.15<x<0.54), the material possesses a rhombohedral symmetry with the A and B-site cations in the ferroelectric phase displaced along the $[111]_{pc}$ direction in the unit cell. The subscripts pc denotes a pseudocubic cell, since the distortions are small. At low temperatures, the oxygen octahedra rotate around the $<111>_{pc}$, producing an $a^-a^-a^-$ tilt system using Glazer notation.[2] The effects of this type of phase transition have

44

been widely noted to influence the properties of ferroelectrics; this is why compositions within the shaded region in Figure 3.1 were studied.
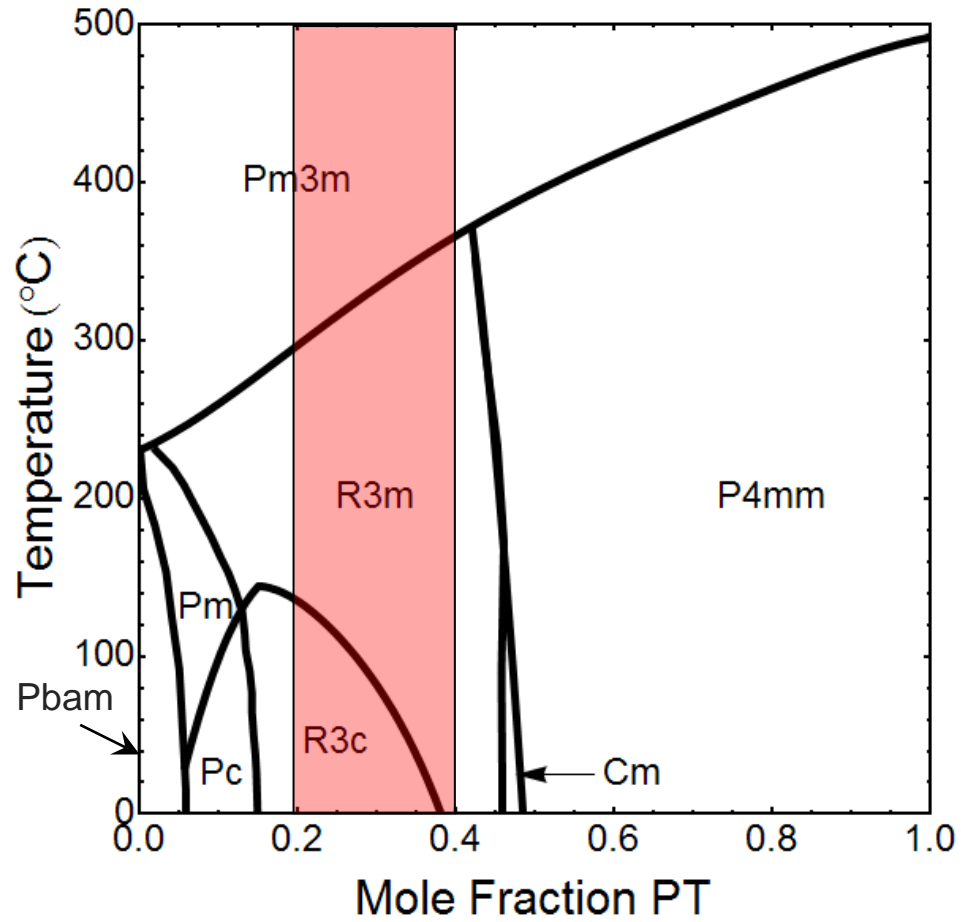
Figure 3.1. Phase diagram for $Pb(Zr_{1-x}Ti_x)O_3$ showing the space groups of the cubic and distorted phases. The highlighted region represents the compositions studied in this thesis.

3.2 *Target Preparation*

Ceramic targets for pulsed laser deposition (PLD) were batched from PbO, TiO_2, and ZrO_2 powders. 20 mol% excess PbO was used to compensate for Pb volatility during

the deposition process.[3] Powders were combined in a polyethylene jar and ball milled in ethanol for 1-2 days using ZrO_2 milling media. After being dried in an 80°C oven for 24 hours, the powders were ground in a mortar and pestle and passed through an 80 mesh sieve. An acrylic binder system (Acryloid Resin, Rohm and Hass) was added in a 5 wt% ratio of binder/powder and was diluted with acetone. The powder-binder composite was dried in air and ground in a mortar and pestle until a fine powder was obtained. The powder plus binder was then isostatically pressed at 50 MPa in a 1" cylindrical die in order to provide sufficient compact strength for sintering. The pressed compact was placed on $PbZrO_3$ sand on a refractory ceramic for sintering. During the sintering run, the target was given a three hour soak at 300°C to initiate binder burnout. The binder burnout was completed during a 90 minute soak at 550°C. Liquid phase sintering of the targets occurred at 900°C for 2 hours (since the PbO melting point is 880°C). This allowed for sufficient densification so that the targets were mechanically stable (i.e. not easily polished) and had little observable surface porosity in an optical microscope. The resulting targets were a multi-phase ensemble as shown in Figure 3.2, with evidence of a perovskite phase along with PbO.
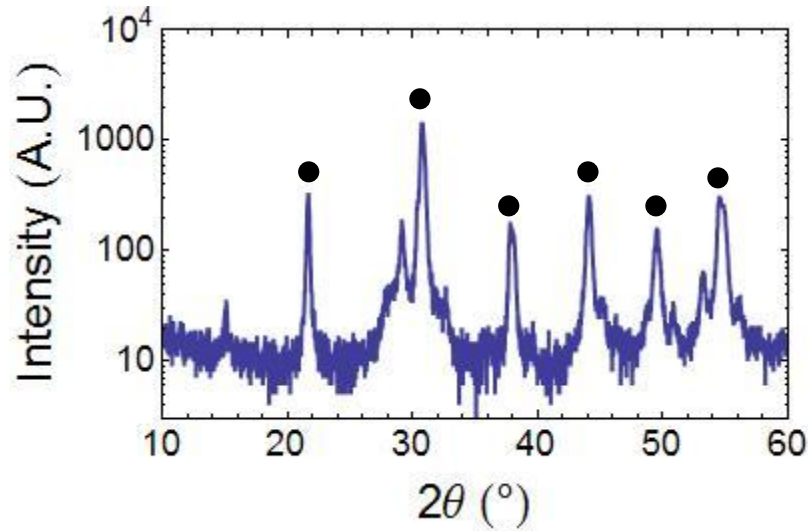
Figure 3.2. Representative θ-2θ scan of the target material. The composition shown is $Pb(Zr_{0.7}Ti_{0.3})O_3$. Circles denote perovskite phase.

3.3 *Vacuum System*

The vacuum system used in this study was designed by Maffei[4] for pulsed laser deposition and upgraded by Maria.[5] A schematic of the pulsed laser deposition system is given in Figure 3.3.[6] A Varian model M6 diffusion pump with fluorinated polymer oil (Solvey Solexis, Thorofare, NJ) was used to maintain a base pressure of 1 x 10^{-6} Torr. An Alcatel rotary pump was used as a backing and roughing pump. A Bayard-Alpert ion gauge (Duniway Stockroom Corp, Mountain View, CA) was used to determine the base pressure. During deposition, a convectron style gauge was used to monitor pressure. The process gas for deposition of PZT was a 10%/90% mixture of O_3/O_2 output from a PCI-G1 ozone generator. Ultra-high purity (UHP) oxygen was used as the source gas for the ozone generator. An MKS model 179A (MKS Instruments, Wilmington MA) flow meter set at a flow rate of ~50 sccm was used to introduce the ambient gas to the growth chamber. With the gate valve open, a minimum deposition pressure of 15 mTorr was

47

achieved. Deposition pressures above 15 mTorr were obtained through constriction of the gate valve between the deposition chamber and the diffusion pump. A valve which bypassed the mass flow controller was used to rapidly increase the pressure to >100 Torr after deposition to allow the sample to cool under oxidizing conditions.

Compex KrF102

λ= 248 nm
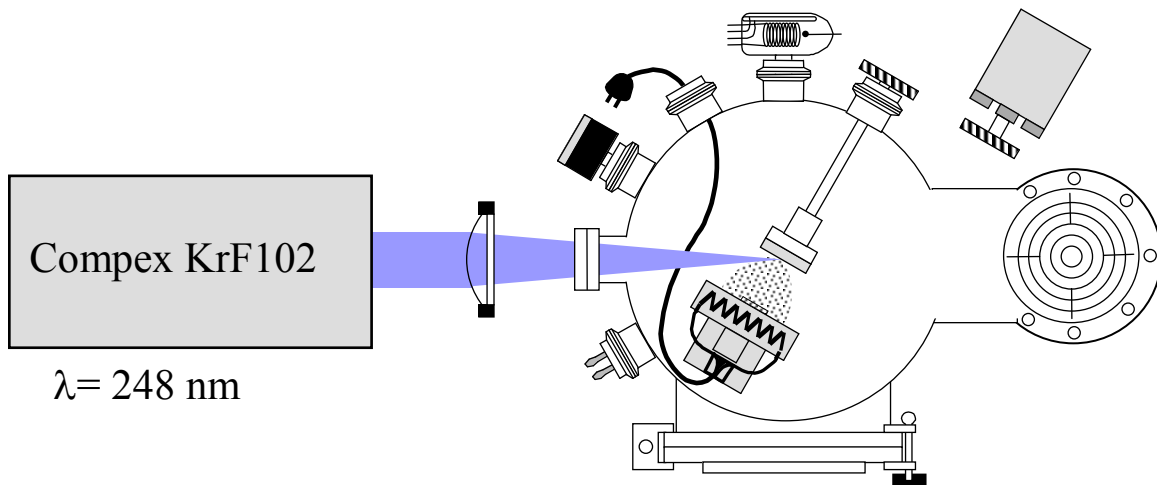
Figure 3.3. Schematic of pulsed laser deposition setup used for these experiments. [6]

The block heater used to control the substrate temperature was constructed from 304 stainless steel and was resistively heated using a winding of Inconel sheathed nickel-chromium wire produced by Thermocoax. The temperature of the heater block was monitored via an Omega K-type thermocouple imbedded into the center of the heater block. A Hewlett Packard model 6268B direct current supply was used as a power supply for the heater. The power required to reach 700°C was on the order of 250 W. The heater block was mounted on an independent stand, which allowed the target-to-substrate distances to be varied between 4 and 9 cm, as well as the use of off-axis geometries.
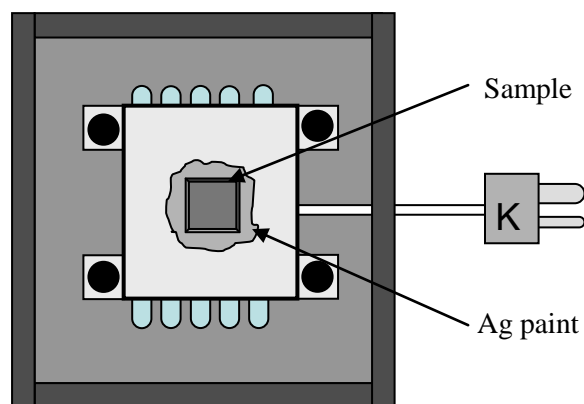
Figure 3.4.   Schematic of heater block used for these experiments.[7]

SrTiO$_3$ substrates were purchased from MTI Crystal Inc. (Richmond, CA) or Crystec (Germany), while Pt-coated Si substrates were purchased from Nova Electronic Materials Ltd (Carrollton, TX). Substrates were cleaned by sonicating for five minutes in acetone, methanol, and isopropanol, successively, and blown dry using a dry Ar jet. They were then bonded to the heater block using silver paint and cured at temperatures between 175 and 200°C for 30 min prior to deposition to ensure good thermal contact.

The laser used in this study is a KrF laser (Coherent CompexPro 102, Fort Lauderdale, FL) which emits 248 nm ultraviolet radiation. A fused quartz window was used to pass the beam into the vacuum chamber. A plano-convex lens focused the laser to a spot size of ~ 2 mm x 1 mm at the target surface. An energy density at the target surface of ~2 J/cm^2 was used.[8] The targets were mounted on a rotary feed-through which allowed the target to be rotated during deposition so that subsequent laser pulses impinged at different locations on the surface.

3.4 *Pulsed Laser Deposition of $Pb(Zr_{1-x}Ti_x)O_3$ Thin Films*

Following the work of Maria on $Pb(Mg_{1/3}Nb_{2/3})O_3$-$PbTiO_3$ growth, a substrate temperature of 630°C and a growth pressure of 100 mTorr O_2/O_3 were used as initial conditions for growth.[9] A laser repetition rate of 10 Hz was used to minimize Pb-loss by reducing the time for evaporation between pulses. The target-substrate distance was set to 6 cm. In order to optimize the growth temperature, films were prepared on Pt-coated substrates, for which there is no epitaxial stabilization of the perovskite phase. Once phase stability was determined, films were grown on (001), (111) and (110) oriented $SrTiO_3$. $SrRuO_3$ bottom electrodes were deposited from ceramic targets (Target Materials Inc., Columbus, OH) following the procedure of Maria et al. and shown in Table 3.1.[10]

Table 3.1. Growth conditions for $SrRuO_3$ used in this study.

Growth Parameter	Value
Deposition Temperature	680°C
Deposition Pressure	160 mTorr
Target to Substrate Distance	8 cm
Deposition Length	10 minutes
Laser Fluence	200 mJ
Cool Down Pressure	100 Torr
Ambient Gas	$0.9O_2/0.1O_3$

For deposition of the $Pb(Zr_{1-x}Ti_x)O_3$ films, the heater was placed at the edge of the plume in an on-axis geometry. During evacuation of the chamber, the sample was heated to the deposition temperature in 3 steps over the course of 1 hour. Prior to deposition, O_2/O_3 was fed into the chamber and the gate valve was throttled to give the desired process pressure. The deposition time was varied to control the thickness of the film.

Immediately following deposition, the power supply to the heater was turned off to minimize Pb-loss at high temperatures. Next, the gate valve was closed and a bypass valve was opened and the process gas was allowed to rapidly fill the chamber until a pressure of 100 Torr was obtained; the overpressure should help control Pb-loss as well as minimize oxygen vacancies. This high pressure was achieved before the film was cooled below 500°C.

3.5 *Structural Characterization*

3.5.1 2-circle X-ray Diffraction

A Scintag powder diffractometer operating in θ-2θ mode was used in this study to measure the crystallographic texture of the films. Typical settings on the instrument were 35 kV and 30 mA. The films on single crystal substrates were measured to determine if there were any second phases or other orientations present. A common contamination was a small secondary peak originating from the $SrRuO_3$ layer at 38° 2θ, which occurred in a small number of samples and had no obvious effect on the as deposited PZT films.

3.5.2 4-circle X-ray Diffraction

Out-of-plane lattice parameters were investigated using a Philips X'pert Pro MRD High resolution 4-circle diffractometer (PANalytical Inc., Tempe, AZ) equipped with high temperature stage capabilities. The diffractometer was equipped with a hybrid graphite monochromater which selectively collimated Cu $K_{\alpha 1}$ radiation. A schematic of a typical 4-circle diffractometer geometry is shown in Figure 3.5.
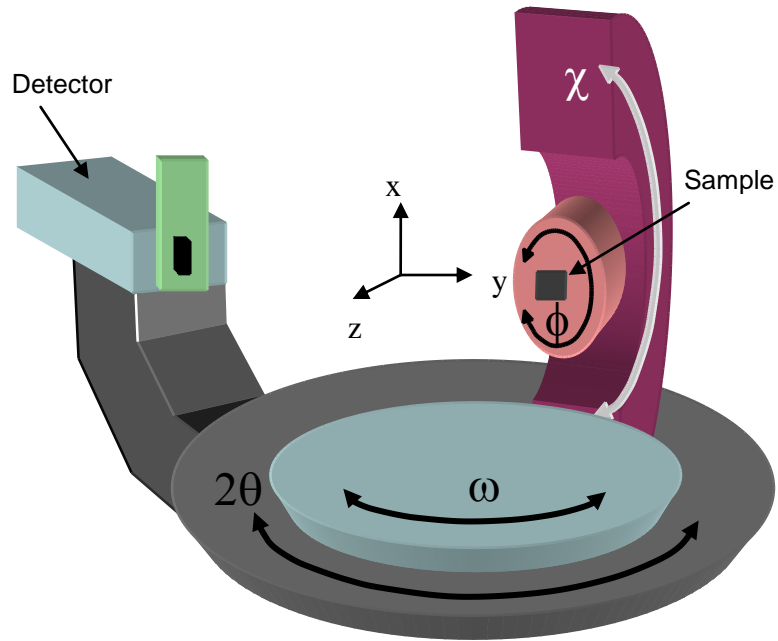
Figure 3.5.   Schematic of 4-circle x-ray diffraction geometry.[7]

Samples were mounted on a zero-background holder made from highly miscut Si single crystal. The zero of the x-ray beam was found and the sample was moved in the *z*-direction until the beam intensity was approximately cut in half.   A scan in the z-direction was performed and the z-position was moved so that the sample halved the beam. The sample was rocked in the ω-axis to align the sample surface parallel to the direction of the x-ray beam and realigned in the *z*-direction. The sample was then moved to a substrate peak to align the goniometer to the miscut in the single crystal. This was done using scans in the x, y, z, ω, 2θ, and χ axes. After a sample was aligned to a substrate peak, θ-2θ scans and ω-scans (rocking curves) were performed on the film and substrate peaks. To determine the in-plane lattice parameters, the 101_{pc} peak was used. The sample was set to a χ of 45° and scanned in ϕ to locate the substrate reflection. Once the substrate reflection was located, alignment scans in ϕ, χ and 2θ were completed. θ-

2θ scans were acquired to determine the in-plane lattice parameter and a 360° ϕ scan was performed to determine epitaxy.

The lab-source diffractometer offered the ability to characterize the Bragg peaks of deposited films, however the superlattice reflections observed were 2-3 times the noise floor at room temperature and unsuitable for performing temperature dependant diffraction. In order to characterize the superlattice reflections as a function of temperature, temperature dependent x-ray diffraction experiments were performed at the Advanced Photon Source at the 33-BM beam line using a Huber 4-circle diffractometer (Figure 3.6). The high flux of the Advanced Photon Source allows for detection of the weak superlattice reflections even from thin layers. The high x-ray energy used (21 keV) enabled large regions of reciprocal space to be investigated. The sample was mounted to a temperature stage developed for *in situ* deposition of films using spring loaded ceramic clips.[11] SPEC software was used to control the diffractometer; this allowed scans to be performed by controlling the individual motors or by scanning through directions in reciprocal space.
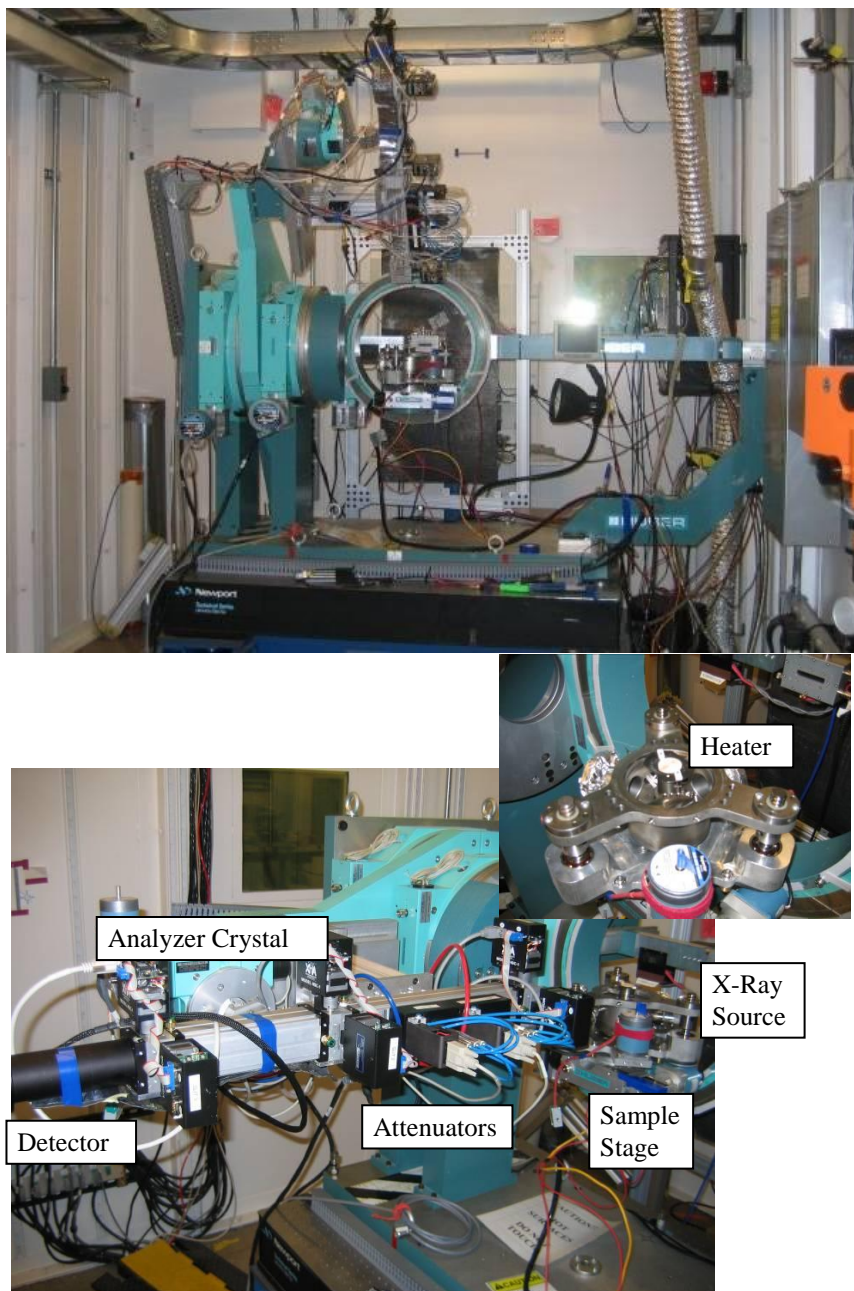
Figure 3.6. Huber diffractometer installed at beam line 33BM at the Advanced Photon Source with the high temperature heater mounted to the diffractometer.

The orientation of the crystal was determined at room temperature prior to heating by locating an out-of-plane $SrTiO_3$ reflection (444 for a (111) oriented $SrTiO_3$ or 006 for (100) oriented $SrTiO_3$) and the 311 $SrTiO_3$ reflection. Additionally, the Bragg peaks arising from the $Pb(Zr_{1-x}Ti_x)O_3$ films were found at room temperature prior to heating above T_C. The sample was heated to a temperature above T_C; at each temperature 2θ, θ, χ, and z alignment scans were performed to ensure that the sample was in the center of the diffractometer circle.

The temperature at each step was calibrated using the thermal expansion of the $SrTiO_3$ substrate. The $SrTiO_3$ 444 reflection was recorded and the thermal expansion for the crystal was calculated. The experimental thermal expansion of the $SrTiO_3$ was plotted against the thermal expansion data reported in literature.[12] For the particular sample shown in Figure 3.7 it was found that the temperature of the sample was ~10% higher than the heater. The out-of-plane film peak was found and θ-2θ scans were acquired.
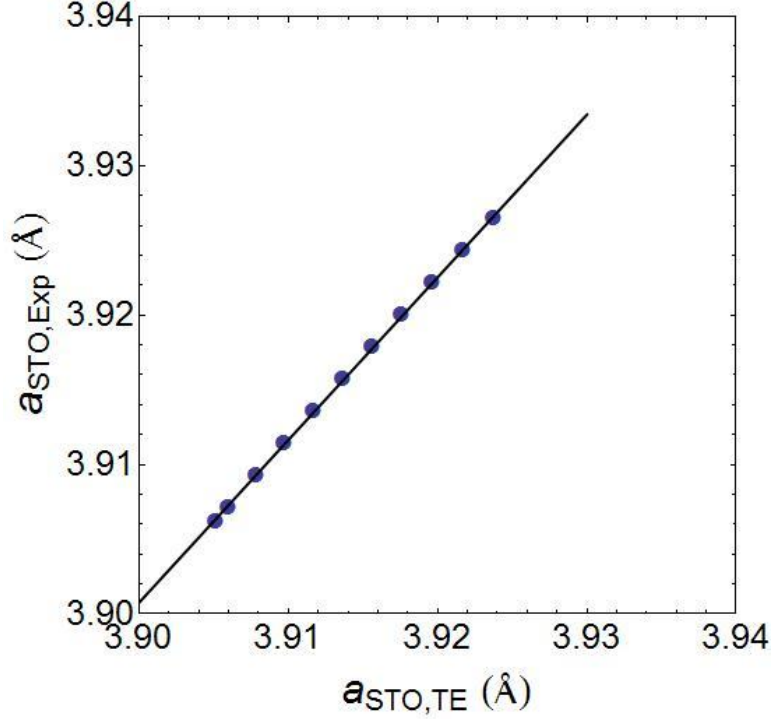
Figure 3.7. Experimental ($a_{STO,Exp}$) vs. reported lattice parameter ($a_{STO,TE}$) calculated using reported thermal expansion data[12] for temperature calibration of the high temperature x-ray diffraction equipment.

Alignment scans in the 2θ, χ and ϕ directions were performed on the 311_{pc} and ½$(311)_{pc}$ reflections, and data were collected. The peaks were fit using the pseudo-Voigt function and peak positions and integrated intensities were calculated after background subtraction. The peaks were fit using the pseudo-Voigt function:[13]

$$I = A_0(\mu_0 \frac{2}{\pi} \frac{fwhm_0^2}{(x-cen_0)^2 + fwhm_0^2} + (1-\mu_0)\frac{\sqrt{4\ln(2)}}{2\sqrt{\pi}\,fwhm_0} e^{\frac{\sqrt{4\ln(2)}}{2\sqrt{\pi}\,fwhm_0}(x-cen_0)^2}) + C$$

Equation 3.1 Pseudo-Voigt Function

where A_0 is amplitude, $fwhm_0$ is the full width at half-maximum of the reflection, cen_0 is the position of the reflection, μ_0 is a parameter to weight the function between the

Gaussian and Lorentzian components, and C is a constant. The integrated intensities of the diffracted peaks as a function of temperature were calculated after background subtraction. For multiple peaks a second set of independent parameters was added to the equation. Also, simple functions such as A_0x were added to compensate for a non-constant background.

3.5.3 Transmission Electron Microscopy

Cross sectional transmission electron microscopy (TEM) specimens were prepared by mechanical polishing followed by Ar ion milling using a Gatan Duo Mill, operated at 6 kV and a combined current of 6 mA. Room temperature microstructural characterization was performed using diffraction contrast imaging and selected area electron diffraction techniques with a JEOL 2010f TEM, operated at 200 kV. The low and high temperature electron diffraction experiments were performed in a liquid He sample holder attached to a Hitachi H-8000 TEM and a hot sample stage on a Philips CM200 TEM, respectively. In this context, all crystallographic directions and planes refer to the pseudocubic unit cell.

3.6 *Electrical Property Measurements*

The dielectric properties of the films were characterized via capacitor structures shown schematically in Fig. 3.6. Films were deposited on a bottom electrode, in either epitaxial or polycrystalline form, with a Pt-top electrode. The permittivity was calculated using Equation 3.2:

$$C = \varepsilon_o \varepsilon_r \frac{A}{d},$$

Equation 3.2 Capacitance equation

where C is capacitance, ε_o and ε_r are the permittivity of free space and the relative permittivity respectively, A is area of the capacitor, and d is the thickness.

Photolithography was performed to pattern the top electrodes. The top electrode area ranged from ~75 μm^2 to 0.04 mm^2. Shipley 1811 photoresist was used in conjunction with LOR 5A lift-off resist (MicroChem Corp. Newton, MA) to pattern the electrodes. Samples were cleaned using acetone, dried using a dry nitrogen jet, and a ~10s bake at 180°C and the cleaning was repeated with isopropanol to ensure a clean surface prior to lithography. Lift-off resist was spun on the samples at ~4000 rpm for 45s prior to a bake at 180°C for 2 minutes to remove excess solvents. Photoresist was spun at 4000 rpm for 45s followed by a soft bake at 100°C for 1 minute. UV exposure was performed using an Hg vapor lamp operating at ~300 W for 90s in an Suss MJB3 mask aligner. The photoresist and lift-off resist were developed using CD-26 (Shipley Marlboro MA) for approximately a minute, or until clear undercutting of the photoresist was observed. After developing, the samples were rinsed using de-ionized water and dried using a dry-N_2 jet.

The Pt-top electrode was sputtered using the W.M. Keck Smart Materials Integration Laboratory Lesker sputter system. The system involves a high vacuum chamber with multiple sputter guns allowing for deposition of multiple materials at one time. Pt-electrodes were deposited at low Ar pressures of 2.5 mTorr. The typical thickness of Pt metal deposited was 50 nm. Excess Pt and photoresist were removed

using acetone while the remaining lift-off resist was removed using the CD-26 developer. Prior to electrical measurements, the samples were annealed in O_2 at 500°C to provide a good interface between the metal and dielectric. This is done to minimize space charge contributions to the measurements.

Measurements were made using a pair of point probes. Contact to the top electrode was achieved via physical contact between the point probe and the Pt electrode. The bottom electrode was contacted either through a shorted electrode or by etching the dielectric using a buffered HF solution to reveal the bottom electrode. Polarization hysteresis loops were measured using a TF Analyzer 2000 (aixACCT Systems GmbH, Aachen, Germany). When the voltage required for hysteresis loops exceeded the aixACCT tool's 25V limit, a 10:1 voltage amplifier (AVC Instrumentation, Div. of PCB Piezotronics Inc., Depew, NY) was used. The aixACCT tool was also used to perform PUND (Positive-Up-Negative-Down) measurements as a function of temperature in an attempt to remove leakage effects from the hysteresis measurements at high temperature.

Capacitance and loss measurements were made using a Hewlett Packard 4192A LF impedance analyzer (Agilent Technology, Palo Alto, CA) on a probe station equipped with a high temperature stage. LabView programs were used to record the capacitance and loss data as a function of frequency (0.1-1000 kHz), applied DC bias (0-20V) and temperature between room temperature and 400°C using a 30 mV AC field excitation. Additionally, the AC field excitation was varied as a function of frequency, DC bias field, and temperature.

3.7 *References:*

[1]D. I. Woodward, J. Knudsen, and I. M. Reaney, "Review of crystal and domain structures in the $PbZr_xTi_{1-x}O_3$ solid solution," *Physical Review B,* **72**[10] 104110 (2005).

[2]A. M. Glazer, "Classification of tilted octahedra in perovskites," *Acta Crystallographica Section B-Structural Science,* **B 28**[Nov15] 3384-92 (1972).

[3]C. D. Theis and D. G. Schlom, "Epitaxial lead titanate grown by MBE," *Journal of Crystal Growth,* **174**[1-4] 473-79 (1997).

[4]N. Maffei, "Excimer laser ablated bismuth titante thin films for nondestructive readout nonvolatile memory applications" pp.169, Ph.D. thesis in Materials Science and Engineering, The Pennsylvania State University, (1993)

[5]J. P. Maria, "Deposition and measurement of epitaxial barium titante thin films using conductive epitaxial oxide electrodes prepared by pulsed laser deposition" pp.145, M.S. thesis in Materials Science and Engineering, The Pennsylvania State University, (1996)

[6]L. F. Edge, "Pulsed laser deposition of bismuth zinc niobate thin films for dielectric applications" pp.116, M.S. thesis in Materials Science and Engineering, The Pennsylvania State University, (2002)

[7]D. S. Tinberg, "Pulsed laser deposition of xBiScO$_3$-(1-x)BaTiO$_3$ thin films for Pb-free dielectric applications" pp.127, M.S. thesis in Materials Science and Engineering, The Pennsylvania State University, (2006)

[8]M. D. Strikovsky, E. B. Klyuenkov, S. V. Gaponov, J. Schubert, and C. A. Copetti, "Crossed fluxes technique for pulsed-laser deposition of smooth $YBa_2Cu_3O_{7-X}$ films and multilayers," *Applied Physics Letters,* **63**[8] 1146-48 (1993).

[9]J. P. Maria, W. Hackenberger, and S. Trolier-McKinstry, "Phase development and electrical property analysis of pulsed laser deposited $Pb(Mg_{1/3}Nb_{2/3})O_3$-$PbTiO_3$ (70/30) epitaxial thin films," *Journal of Applied Physics,* **84**[9] 5147-54 (1998).

[10]J. P. Maria, H. L. McKinstry, and S. Trolier-McKinstry, "Origin of preferential orthorhombic twinning in $SrRuO_3$ epitaxial thin firms," *Applied Physics Letters,* **76**[23] 3382-84 (2000).

[11]A. Munkholm, S. K. Streiffer, M. V. R. Murty, J. A. Eastman, C. Thompson, O. Auciello, L. Thompson, J. F. Moore, and G. B. Stephenson, "Antiferrodistortive reconstruction of the $PbTiO_3$ (001) surface," *Physical Review Letters,* **88**[1] 016101 (2002).

[12]Y. S. Touloukian, "Thermal Expansion--Nonmetallic Solids." in Thermophysical Properties of Matter, **Vol. 13.** IFI/Plenum, 1977.

[13]D. Balzar, "Profile fitting of x-ray-diffraction lines and Fourier-analysis of broadening," *Journal of Applied Crystallography,* **25** 559-70 (1992).

Chapter 4   SrRuO$_3$ Thin Films

4.1 *Introduction*

SrRuO$_3$ (SRO) is widely used as a bottom electrode for perovskite thin films due to its metallic electrical conductivity, high resistance to chemical erosion and good lattice matching with a wide range of perovskite materials.[1-3] At room temperature, it has a GdFeO$_3$-type orthorhombic structure (space group Pbnm), which can be described as a distorted pseudocubic perovskite cell, $a = a_{pc}\sqrt{2}$, b $= a_{pc}\sqrt{2}$ and c $= 2a_{pc}$ ($a_{pc} =\sim3.93$ Å where the subscript pc denotes pseudocubic).[4] The *Pbnm* symmetry of SRO is dictated by an a$^-$a$^-$c$^+$ Glazer tilt system, in which the O octahedra rotate with equal magnitude in antiphase around the a_{pc} and b_{pc} axes and in-phase around the c_{pc} axis.

Epitaxial SRO has been successfully grown on (001) oriented substrates including Si,[5] MgO,[6,7] (LaAlO$_3$)$_{0.3}$-(SrAl$_{0.5}$Ta$_{0.5}$O$_3$)$_{0.7}$(LSAT),[8] LaAlO$_3$ (LAO),[9,10] and SrTiO$_3$,[7,8,11-15] by either pulsed later deposition (PLD), off-axis *rf* magnetron sputter deposition or metallorganic chemical vapor deposition (MOCVD). Even though the SRO layer maintains a well-defined cube-on-cube epitaxial relationship with the underlying substrates, multi-domain structures are generally observed either by XRD,[6,7] or TEM[5,9,16] as result of the orthorhombic symmetry of SRO. Briefly, 6 types of ferroelastic domain may co-exist in the epitaxial SRO layers, with 4 types being associated with the *c* pseudocubic axis lying in-plane and 2 types with that out of plane.[17] The ferroelastic domain structure of thin film SRO is now well understood. In this chapter, the tilt system of SrRuO$_3$ will be investigated. This is done to determine the tilt system of SrRuO$_3$ thin films and to gather a baseline for studying relaxed PZT films.

4.2 *Structural Characterization of SrRuO₃ Thin Films*

Figure 4.1 is a dark-field image taken from the SRO/LAO(001) sample close to the <100> pseudocubic direction.[*] The film is ~60 nm thick and highly faulted/strained as evidenced by the strong but varied diffraction contrast under two beam conditions. No reaction layer was observed in high magnification studies of the SRO/LAO interface.
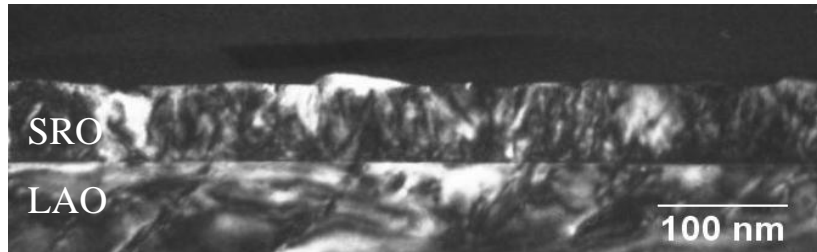
Figure 4.1. Dark-field image from the $(001)_{pc}$SRO/LAO sample taken along the $<100>_{pc}$ direction.

For comparison, electron diffraction patterns were also recorded from a bulk ceramic SRO sample prepared by a standard mixed-oxide processing route. Figure 4.2(a), (b) and (c) are representative diffraction patterns from the bulk SRO sample taken along the $[001]_{pc}$, $[100]_{pc}$ and $[110]_{pc}$ zone axes, respectively. In addition to fundamental diffraction spots, superlattice reflections are also present at $\frac{1}{2}\{ooe\}_{pc}$ ($h\neq k$), $\frac{1}{2}\{ooo\}_{pc}$ ($h\neq k$) and $\frac{1}{2}\{eeo\}_{pc}$ ($h\neq k$) positions, in agreement with the known *Pnma* symmetry and the $a^-a^-c^+$ Glazer tilt system.[4] Diffraction patterns taken from the SRO/LAO(001) sample along the $<100>_{pc}$ and $<110>_{pc}$ directions are shown in Figure 4.2(d) and (e), respectively. Figure 4.2(d) is a multidomain diffraction pattern in which three sets of superlattice reflections of the type $\frac{1}{2}\{ooo\}_{pc}$ and $\frac{1}{2}\{eeo\}_{pc}$ along two $<100>_{pc}$ directions

---

[*] All of the TEM micrographs reported in this thesis were taken by Dr. Yisong Han.

are recorded. Thus, as has been reported previously, the SRO layer consists of a multi-domain structure although it maintains a cube-on-cube epitaxial relationship. More interestingly, along the $<110>_{pc}$ projection, extra spots located at $\pm 1/6(ooo)_{pc}$ and $\pm 1/3(ooo)_{pc}$ positions are also observed (arrowed in Figure 4.2(e) and described with reference to the fundamental diffraction spots in Figure 4.2(c)).

Bulk SRO   **SRO film**
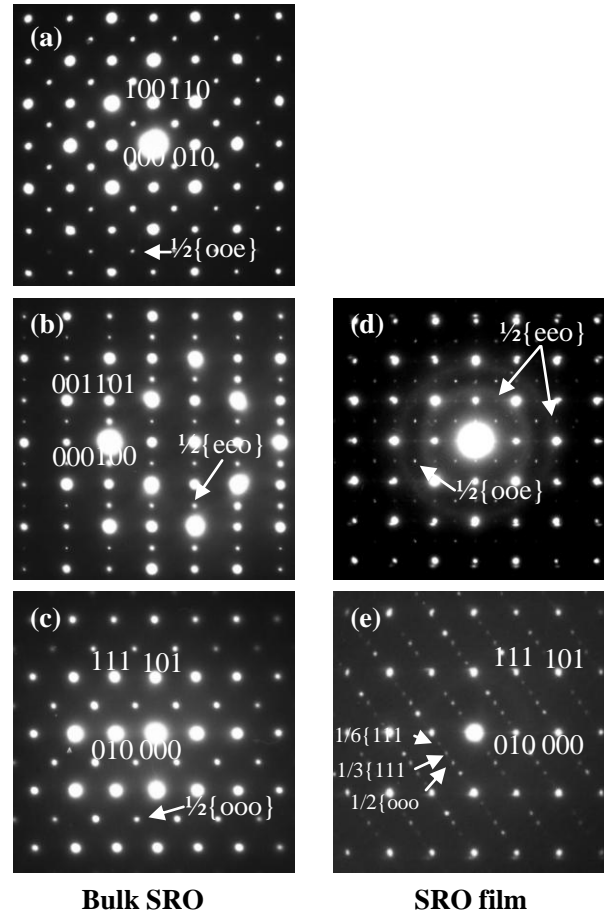
Figure 4.2.   (a), (b) and (c) diffraction patterns taken from bulk SRO ceramics along the $<001>_{pc}$, $<100>_{pc}$ and $<110>_{pc}$ axes, respectively; (d) and (e) are diffraction patterns taken from the SRO/LAO thin films along the $<100>_{pc}$ and $<110>_{pc}$ axes, respectively.

For a standard tilt system, superlattice reflections are expected at the $\frac{1}{2}\{ooo\}_{pc}$ and $\frac{1}{2}\{ooe\}_{pc}$ positions. The presence of the reflection at the $1/6\{ooo\}_{pc}$ and $1/3\{ooo\}_{pc}$ positions should not arise from the tilt system and should be from something other type of super structure not related to octahedral tilting. In Figure 4.3, the diffraction pattern in Figure 4.2(d) is reconstructed from (111) twinned single domain variants of the pseudocubic $<110>_{pc}$ zone axis. The superstructure reflections at $\pm 1/6(ooo)_{pc}$ and $\pm 1/3(ooo)_{pc}$ positions are reproduced and attributed to either the matrix SRO, $(111)_{pc}$ SRO twins or multiple diffraction effects. The dark and red circles correspond to the fundamental diffraction spots from the matrix and the twins, respectively, with solid circles corresponding to the $\frac{1}{2}\{ooo\}_{pc}$ superlattice spots for each case. The $[110]_{pc}$ zone-axes diffraction pattern from the twins (Figure 4.3(b)) are rotated ~70.7° and superimposed on the $[110]_{pc}$ zone-axis diffraction pattern from the matrix (Figure 4.3(a)).
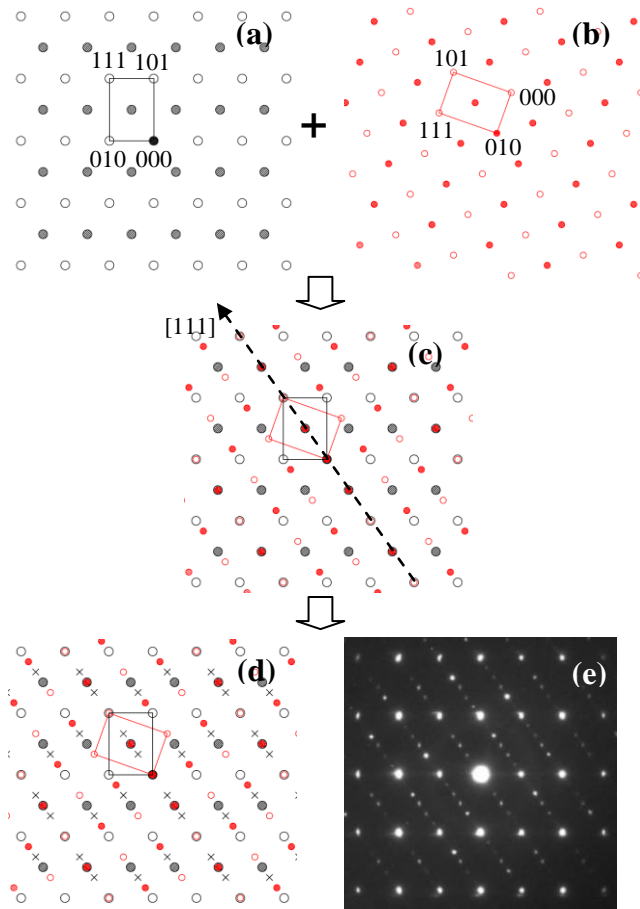
Figure 4.3. Schematic (a–d) and experimental (e) diffractions patterns (reproduced for ease of comparison) along the $<110>_{pc}$ projection. Combining diffraction patterns from (a) matrix SRO and (b) twinned SRO generates pattern (c). (d) Multiple diffraction generates further reflections in the positions indicated by crosses (e)

The major effect of this twin operation is to produce systematic rows of diffraction spots at some but not all $\pm 1/6\{ooo\}_{pc}$ and $\pm 1/3\{ooo\}$ positions. The electron beam is parallel to the $(111)_{pc}$ twin plane and the diffraction patterns from the matrix and the twins are mirror reflections across the $[111]_{pc}$ twin axis. However, some spots at $\pm 1/3(111)_{pc}$ positions are absent in Figure 4.3(c) in comparison with the experimental

diffraction pattern (Figure 4.3(e)). These spots are represented by crosses in Figure 4.3(d) and normally have lower intensity as compared with the corresponding $\pm 1/3(ooo)_{pc}$ position spots with opposite signs in the same row. The weaker reflections arise from multiple diffraction by routes of the type: $(ooo)_{pc} \pm 1/3(ooo)_{pc} = \pm 2/3(ooo)_{pc}$. An inclined twin is highlighted in Figure 4.4(a). The dark-field image was recorded using a diffraction spot attributed to the microtwins. The width of the twin is ~30 nm, much smaller than the smallest available objective aperture (~100 nm). Due to the nature of the TEM specimen (thickness and size of twins), such multiple diffraction effects could not be avoided. In addition, $(111)_{pc}$ twinning takes place on all four inclined $\{111\}_{pc}$ planes in this sample, giving rise to the diffraction pattern shown in Figure 4.4(b) which exhibits superstructure reflections along all $\langle 111 \rangle_{pc}$ directions.

Twins within perovskite materials have long been recognized,[18-20] whilst $(111)_{pc}$ growth twin structures are more likely to be found in thin films than in ceramics.[5,7,21] In the case of SRO, $(111)_{pc}$ twins are difficult to distinguish because of the coincidence of reflections from the matrix and twinned grains. In addition, multiple diffraction 'fills in' the salient systematic absences at $\pm 1/3\{ooo\}_{pc}$ positions which would normally be the fingerprint of a diffraction pattern arising from a twinned microstructure. In the case of perovskites, further confusion arises in that several other mechanisms can also produce apparent superstructure spots at $\pm 1/6\{ooo\}_{pc}$ and $\pm 1/3\{ooo\}_{pc}$ positions. Hexagonal BaTiO$_3$ contains face-shared O octahedra which create a unit cell in which the c axis has a lattice parameter $\sim 6 \times d_{(111)pc}$ and a and b axes $\sqrt{2}d_{(001)pc}$. Reflections therefore appear at $\pm 1/6\{ooo\}_{pc}$ positions.[22,23] Planes of O vacancies on each third $(111)_{pc}$ plane have also

been shown to give rise to superlattice reflections at $\pm 1/3(ooo)_{pc}$ [24] and the combination of 1:2 ordering with a complex tilt system in compounds such as $Ca_4Nb_2O_9$ have superstructure reflections at $\pm 1/3(ooo)_{pc}$ and $\pm 1/6(ooo)_{pc}$ positions.[25]
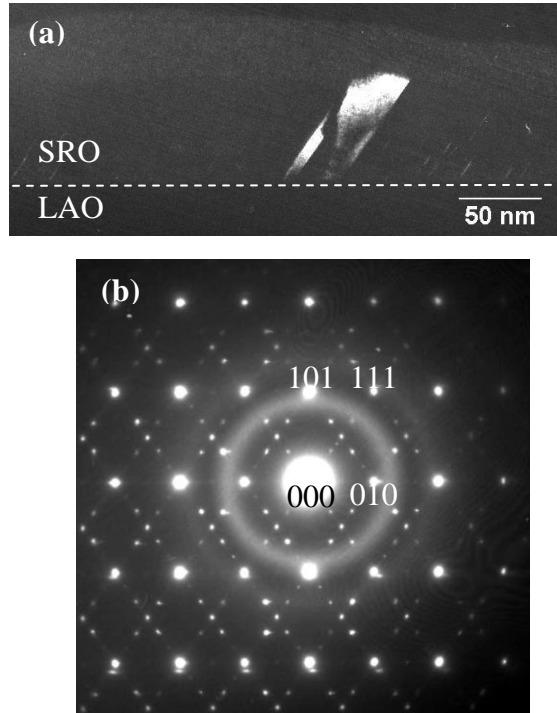
Figure 4.4.   (a) Dark-field image from a region of the SRO/LAO(001)$_{pc}$ thin film, formed using a fundamental diffraction spot from twin grains. (b) <110>$_{pc}$ zone axis diffraction pattern showing extra spots located along both the <111>$_{pc}$ pseudocubic directions.

Similarly, growth twins were found for $SrRuO_3$ films grown on (111) $SrTiO_3$ substrates. This suggests that the growth twins are not unique to films on $LaAlO_3$ and the source of these twins is another mechanism. Although the $SrRuO_3$ thin films exhibited these growth twins they had sufficiently good electrical quality to use as a bottom electrode. $SrRuO_3$ was deposited on $SrTiO_3$ single crystals for the bottom electrode of thick relaxed PZT for electrical measurements and to provide a baseline for strained PZT

films. Samples were taken to the Advanced Photon Source at Argonne National Laboratory to perform temperature dependent x-ray diffraction. Using high energy x-rays and a high resolution diffractometers, it was possible to distinguish the $SrRuO_3$ and PZT peaks. This result is not surprising since due to the large lattice mismatch between $SrRuO_3$ and PZT.
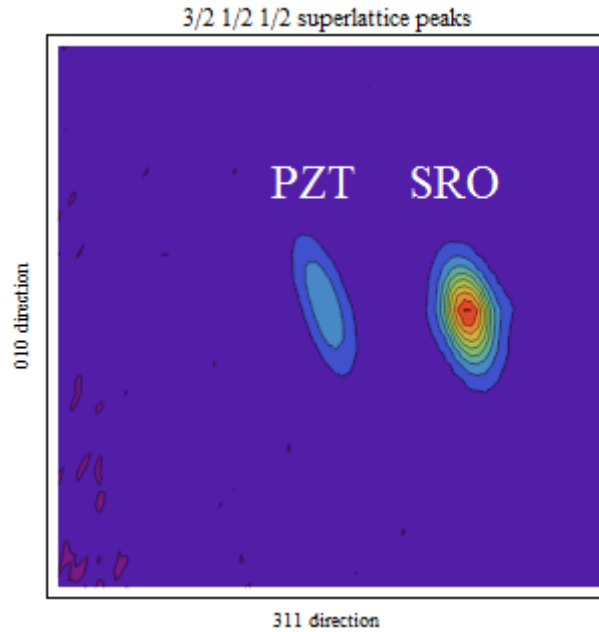
Figure 4.5. Reciprocal space map for the $\frac{1}{2}\{311\}_{pc}$ reflection for PZT and $SrRuO_3$. Peak separation illustrates the ability to distinguish SRO from PZT.

4.3 *References:*

[1]C. B. Eom, R. J. Cava, R. M. Fleming, J. M. Phillips, R. B. Vandover, J. H. Marshall, J. W. P. Hsu, J. J. Krajewski, and W. F. Peck, "Single-Crystal Epitaxial Thin-Films of the Isotropic Metallic Oxides $Sr_{1-X}Ca_XRuO_3$ (0<X<1)," *Science,* **258**[5089] 1766-69 (1992).

[2]H. N. Lee, H. M. Christen, M. F. Chisholm, C. M. Rouleau, and D. H. Lowndes, "Thermal stability of epitaxial $SrRuO_3$ films as a function of oxygen pressure," *Applied Physics Letters,* **84**[20] 4107-09 (2004).

[3]H. N. Lee, H. M. Christen, M. F. Chisholm, C. M. Rouleau, and D. H. Lowndes, "Strong polarization enhancement in asymmetric three-component ferroelectric superlattices," *Nature,* **433**[7024] 395-99 (2005).

[4]B. J. Kennedy and B. A. Hunter, "High-temperature phases of $SrRuO_3$," *Physical Review B,* **58**[2] 653-58 (1998).

[5]Y. X. Chen, J. Koike, T. Higuchi, S. Iwashita, M. Ishida, and I. Shimoda, "Microstructure of epitaxial $SrRuO_3$ films on Si(001) substrates," *Philosophical Magazine B-Physics of Condensed Matter Statistical Mechanics Electronic Optical and Magnetic Properties,* **82**[16] 1731-48 (2002).

[6]W. Y. Ai, J. Zhu, Y. Zhang, Y. R. Li, X. Z. Liu, X. H. Wei, J. L. Li, L. Zheng, W. F. Qin, and Z. Liang, "Microstructure of epitaxial $SrRuO_3$ thin films on MgO substrates," *Applied Surface Science,* **252**[23] 8326-30 (2006).

[7]K. P. Fahey, B. M. Clemens, and L. A. Wills, "Nonorthogonal Twinning in Thin-Film Oxide Perovskites," *Applied Physics Letters,* **67**[17] 2480-82 (1995).

[8]K. Takahashi, T. Oikawa, K. Saito, S. Kaneko, H. Fujisawa, M. Shimizu, and H. Funakubo, "Effect of strain in epitaxially grown $SrRuO_3$ thin films on crystal structure and electric properties," *Japanese Journal of Applied Physics Part 1- Regular Papers Short Notes & Review Papers,* **41**[8] 5376-80 (2002).

[9]J. C. Jiang and X. Q. Pan, "Microstructure and growth mechanism of epitaxial $SrRuO_3$ thin films on (001) $LaAlO_3$ substrates," *Journal of Applied Physics,* **89**[11] 6365-69 (2001).

[10]E. Vasco, R. Dittmann, S. Karthauser, and R. Waser, "Early self-assembled stages in epitaxial $SrRuO_3$ on $LaAlO_3$," *Applied Physics Letters,* **82**[15] 2497-99 (2003).

[11]C. L. Chen, Y. Cao, Z. J. Huang, Q. D. Jiang, Z. Zhang, Y. Y. Sun, W. N. Kang, L. M. Dezaneti, W. K. Chu, and C. W. Chu, "Epitaxial $SrRuO_3$ thin films on (001) $SrTiO_3$," *Applied Physics Letters,* **71**[8] 1047-49 (1997).

[12]J. C. Jiang, X. Q. Pan, and C. L. Chen, "Microstructure of epitaxial $SrRuO_3$ thin films on (001) $SrTiO_3$," *Applied Physics Letters,* **72**[8] 909-11 (1998).

[13]Q. Gan, R. A. Rao, C. B. Eom, J. L. Garrett, and M. Lee, "Direct measurement of strain effects on magnetic and electrical properties of epitaxial $SrRuO_3$ thin films," *Applied Physics Letters,* **72**[8] 978-80 (1998).

[14]J. P. Maria, H. L. McKinstry, and S. Trolier-McKinstry, "Origin of preferential orthorhombic twinning in $SrRuO_3$ epitaxial thin firms," *Applied Physics Letters,* **76**[23] 3382-84 (2000).

[15]R. Bachelet, F. Sanchez, J. Santiso, and J. Fontcuberta, "Reversible growth-mode transition in $SrRuO_3$ epitaxy," *Applied Physics Letters,* **93**[15] 151916 (2008).

[16]G. Herranz, F. Sanchez, J. Fontcuberta, M. V. Garcia-Cuenca, C. Ferrater, M. Varela, T. Angelova, A. Cros, and A. Cantarero, "Domain structure of epitaxial $SrRuO_3$ thin films," *Physical Review B,* **71**[17] 174411 (2005).

[17]J. C. Jiang, W. Tian, X. Q. Pan, Q. Gan, and C. B. Eom, "Domain structure of epitaxial $SrRuO_3$ thin films on miscut (001) $SrTiO_3$ substrates," *Applied Physics Letters,* **72**[23] 2963-65 (1998).

[18]T. J. White, R. L. Segall, J. C. Barry, and J. L. Hutchinson, "Twin Boundaries in Perovskite," *Acta Crystallographica Section B-Structural Science,* **41**[Apr] 93-98 (1985).

[19]L. P. Keller and P. R. Buseck, "Twinning in Meteoritic and Synthetic Perovskite," *American Mineralogist,* **79**[1-2] 73-79 (1994).

[20]W. L. Wang and H. Y. Lu, "Twinning induced by the rhombohedral to orthorhombic phase transition in lanthanum gallate ($LaGaO_3$)," *Physics and Chemistry of Minerals,* **33**[7] 435-44 (2006).

[21]Q. Q. Feng and C. J. McConville, "Investigation of lamella-twinned crystallites and dislocations in paraelectric phases of Bi_2O_3-doped $BaTiO_3$," *Journal of the American Ceramic Society,* **87**[12] 2247-51 (2004).

[22]A. Feteira, D. C. Sinclair, and I. M. Reaney, "Synthesis and characterization of $BaTi_{1-x}Ga_xO_{3-delta}$ ($0 <= x <= 0.15$) ceramics," *Journal of the American Ceramic Society,* **89**[7] 2105-13 (2006).

[23]J. Akimoto, Y. Gotoh, and Y. Oosawa, "Refinement of Hexagonal BaTiO$_3$," *Acta Crystallographica Section C-Crystal Structure Communications,* **50** 160-61 (1994).

[24]D. I. Woodward, I. M. Reaney, G. Y. Yang, E. C. Dickey, and C. A. Randall, "Vacancy ordering in reduced barium titanate," *Applied Physics Letters,* **84**[23] 4650-52 (2004).

[25]I. Levin, L. A. Bendersky, J. P. Cline, R. S. Roth, and T. A. Vanderah, "Octahedral tilting and cation ordering in perovskite-like Ca$_4$Nb$_2$O$_9$-Ca(Ca$_{1/3}$Nb$_{2/3}$)O$_3$ polymorphs," *Journal of Solid State Chemistry,* **150**[1] 43-61 (2000).

Chapter 5   Relaxed Epitaxial Pb(Zr$_{1-x}$Ti$_x$)O$_3$Thin Films

This thesis was directed towards studying octahedral tilting in piezoelectric Pb(Zr$_{1-x}$Ti$_x$)O$_3$ (PZT) thin films. In particular, this chapter focused on the stability of octahedral tilting within relaxed PZT films.

Figure 3.1 shows the phase diagram adapted from Woodward, Knudsen and Reaney.[1] At high PbTiO$_3$ contents, the material remains tetragonal. At x=0.48, there exists a morphotropic phase boundary (MPB) between the rhombohedral and tetragonal phases, with a bridging monoclinic intermediate phase at some temperatures. At higher Zr compositions, (0.15<x<0.54), the material possesses a rhombohedral distortion with the A and B-site in the ferroelectric phase displaced along the [111]$_{pc}$ direction in the unit cell. At low temperatures, the oxygen octahedra rotate along the <111>$_{pc}$ directions in the crystal, giving it a a$^-$a$^-$a$^-$ tilt system using Glazer notation.[2] The octahedral tilt transition influences the properties of ferroelectrics; this is why the compositions within the shaded region in Figure 3.1 were chosen for study. While the Zr-rich side of the phase diagram near the morphotropic phase diagram has widely been described as rhombohedral,[1,3-6] there are recent reports that suggest a monoclinic distortion in addition to the rhombohedral phase.[7] The possible existence of an extended 2-phase region will be ignored. Emphasis here is placed on the presence of tilting.

5.1 *Structural Characterization of Pb(Zr$_{1-x}$Ti$_x$)O$_3$ Thin Films on SrRuO$_3$/SrTiO$_3$*

There are several structural indicators of the phase transitions. First with the development of a spontaneous polarization, the material elongates along the direction of

the polarization, causing a spontaneous strain. This will split the peaks observed in the x-ray diffraction patterns. Peak splitting such as this will occur for different peaks depending on the direction of the polarization, allowing the calculation of the unit cell parameters. By monitoring the development of peak splitting as the sample is cooled, the Curie temperature of the film can be determined.

In addition to the spontaneous strain, antiferroelectric and tilt transitions will lead to a doubling of the unit cell. This doubling introduces extra reflections in the diffraction patterns. For tilt transitions in particular, the superlattice reflections only appear at specific locations for in-phase and anti-phase tilting. The presence of such reflections in a tilted material allows the determination of the material's tilt system. A combination of x-ray diffraction and electron diffraction is a useful way to monitor both the peak splitting as well as octahedral tilting.

5.1.1 X-ray Diffraction of $Pb(Zr_{1-x}Ti_x)O_3$ Thin Films

Thick relaxed films were grown on (100) and (111) oriented $SrTiO_3$ single crystals. Typical thicknesses for the relaxed films were >300 nm. To facilitate electrical measurements, films were grown on conductive $SrRuO_3$. As discussed in chapter 4, it is possible to separate the effect of tilting in $SrRuO_3$ from that in PZT. 4-circle x-ray diffraction was performed on the films to determine the lattice parameters and the film orientation. All films were epitaxial (see representative θ-2θ and ϕ scans in Figure 5.1) and no evidence of a pyrochlore phase was detected.
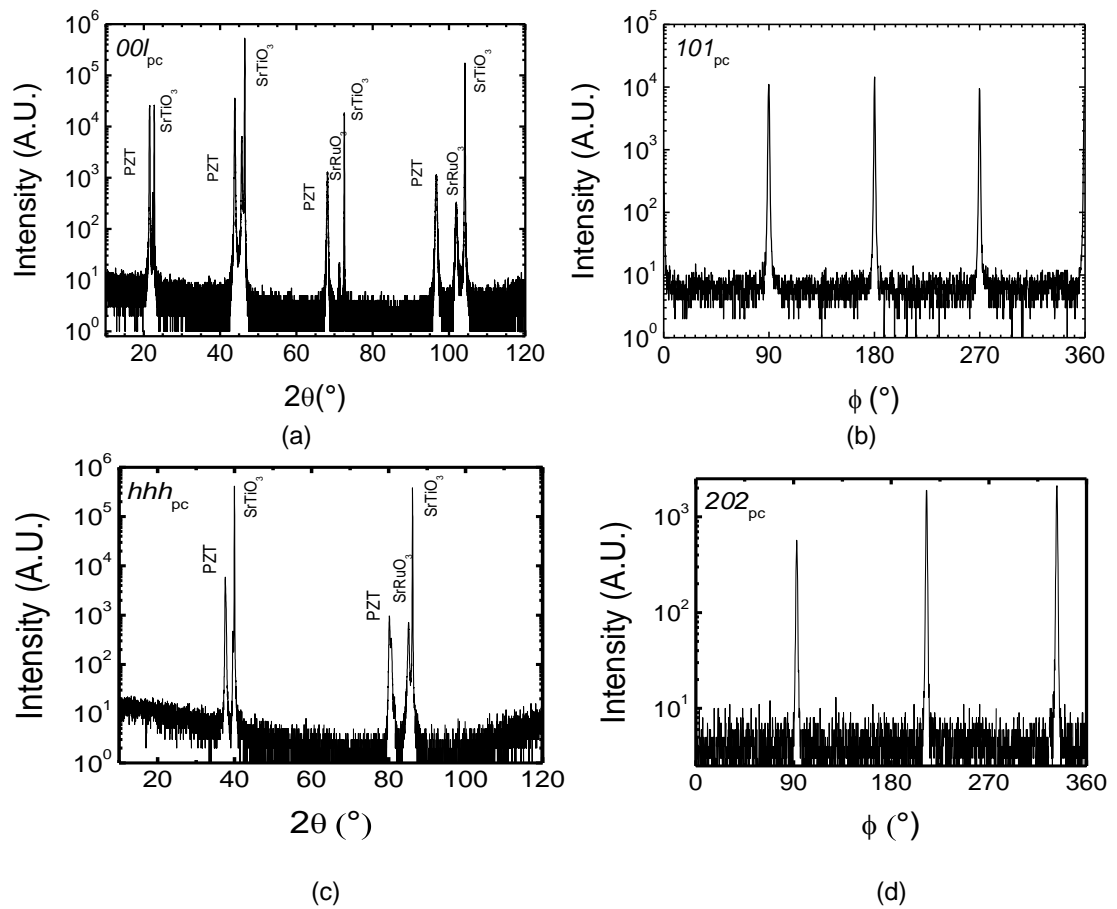
Figure 5.1. (a) θ-2θ and (b) φ scan of a representative $(100)_{pc}$ oriented $Pb(Zr_{0.7}Ti_{0.3})O_3$ showing no second phase and registry with the substrate, indicating epitaxy. (c) θ-2θ and (d) φ scan of a representative $(111)_{pc}$ oriented $Pb(Zr_{0.7}Ti_{0.3})O_3$ showing no second phase and registry with the substrate, indicating epitaxy.

The degree of epitaxy was measured using the full width at half maxima (FWHM) of the in plane and out of plane directions. For $(100)_{pc}$ oriented films, the FWHM in θ and φ were calculated from the 002_{pc} and 101_{pc} peaks, respectively. For $(111)_{pc}$ oriented films, the FWHM in θ and φ were calculated from the 111_{pc} and 200_{pc} peaks,

respectively. The FWHM of the θ rocking curve for $(100)_{pc}$ relaxed PLD films were all less than 0.25°. Additionally, relatively good in-plane alignment was achieved, with FWHM <0.9°. The FWHM values in θ and φ increased slightly on $(111)_{pc}$ oriented samples. The large FWHM indicates the films have some mosaic character. These FWHM are considerable larger than observed for the SrTiO₃ substrate, where the FWHM in θ and φ were ~0.02° and 0.05° respectively.

Table 5.1. Full width at half maximum for $Pb(Zr_{1-x}Ti_x)O_3$ thin films

Substrate Orientation	Scan Axis	x=0.2	x=0.25	x=0.3	x=0.35	x=0.4
$(100)_{pc}$	θ (°)	0.17	0.15	0.21	0.21	0.19
	φ (°)	0.8	0.43	0.56	0.55	0.65
$(111)_{pc}$	θ (°)	0.6	0.4	0.45	0.35	0.39
	φ (°)	1.2	0.8	1	0.75	0.8

Synchrotron x-ray diffraction was performed at the Advanced Photon Source on relaxed films on (111) SrTiO₃ to determine the phase transition temperatures. The 444_{pc} peak was monitored to observe the peak splitting associated with the rhombohedral distortion of the ferroelectric phase, and a $½\{ooo\}_{pc}$ reflection was used to assess octahedral tilting. In addition to making measurements on the PZT film, the SrTiO₃ 444 reflection was recorded to enable calculation of the substrate thermal expansion. Temperature calibration was performed by plotting the measured lattice parameter of SrTiO₃ against the calculated lattice parameter based on the reported thermal expansion.[8] The data were fitted to a line and the recorded temperature was multiplied by the slope to calibrate the temperature. θ-2θ scans were performed every 50°C upon cooling. Figure 5.2(a) shows the temperature dependence of the 444_{pc} d-spacing; a clear transition is

observed from a single peak in the paraelectric phase to two peaks below the Curie temperature. The peak splitting below T_C is consistent with a multidomain state.

For a rhombohedral ferroelectric, the spontaneous strain (x_4) associated with the development of a spontaneous polarization along the $[111]_{pc}$ splits the d-spacing of the $(111)_{pc}$ into a larger d-spacing associated with the direction of spontaneous polarization, $(111)_{pc}$, and a smaller d-spacing associated with the non-polar direction of the ferroelectric, $(11\text{-}1)_{pc}$. The spontaneous strain was calculated from the measured polar 444_{pc} and non-polar $4\bar{4}4_p$ d-spacings relative to the d-spacing extrapolated from the thermal expansion of the paraelectric phase: i.e. $x_4 = \dfrac{d - d_{444_{PE}}}{d_{444_{PE}}}$ where d is the recorded d-spacing of the peak in question, and d_{444_A} is the d-spacing calculated based on the thermal expansion of the high temperature paraelectric phase. It should be noted that the spontaneous strain calculated using the d-spacing associated with the polar direction within the film shows a clear deviation from the extrapolated paraelectric data, whereas the spontaneous strain calculated using the non-polar direction does not deviate from thermal expansion values until T_{Tilt}.

In this part of the phase diagram, the phase transition is considered 2nd order[9] and thus, can be determined from the temperature dependence of the spontaneous strain from the following relationship: $x_4 = aQ_{44}\{1 - \sqrt{[1 - b(T - T_C)]}\}$ where Q_{44} is the electrostrictive constant and a and b are constants.[9,10] Based on this equation, the recorded spontaneous strain data were fitted and T_C was found to be within ~30°C of the bulk values for all of the compositions and orientations investigated.[1]
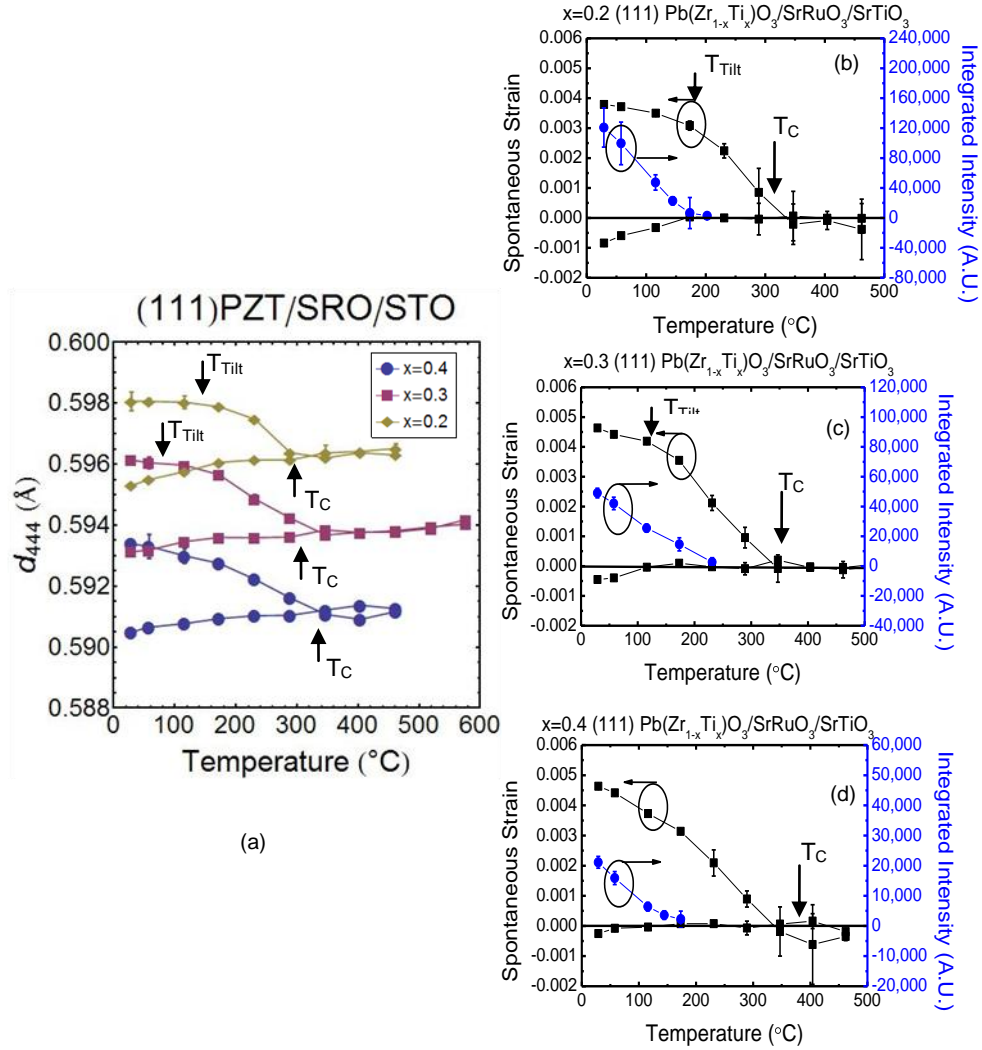
Figure 5.2. (a) Temperature dependence of d_{444pc} for x=0.2-0.4 and the spontaneous strain for d_{444} and $d_{4\bar{4}\bar{4}}$. The integrated intensity of the ½{311}$_{pc}$ reflection is plotted with the spontaneous strain calculated from the 444$_{pc}$ reflection for (b) x=0.2, (c) x=0.3, (d) x=0.4. The arrows indicate the recorded phase transition temperatures for the samples measured.

T_{Tilt} for the films was calculated from the point at which the temperature dependence of the spontaneous strain along the non-polar direction deviated from the

paraelectric extrapolation at low temperatures, and is marked by arrows in Figure 5.2(b-c). In addition, there was also anomaly in the spontaneous strain along the polar direction at T_{Tilt}, as shown in Figure 5.2(b-c). Figure 5.2(d) shows no observed contraction for the $d_{4\bar{4}\bar{1}}$ peak and thus the $PbZr_{0.6}Ti_{0.4}O_3$ film did not exhibit long-range order (LRO) tilting at or above room temperature, which agrees with bulk PZT[13] and with the observed electron diffraction patterns.

The presence of tilting was investigated using the $\frac{1}{2}\{311\}_{pc}$ reflections for the $a^-a^-a^-$ tilt system. The integrated intensity of the $\frac{1}{2}\{311\}_{pc}$ was calculated and it was found that all compositions investigated exhibit intensity at temperatures exceeding the tilt transition temperatures seen for PZT powders. Figure 5.2(b-d) shows the integrated intensity of the $\frac{1}{2}\{311\}_{pc}$ peak plotted with the spontaneous strain, showing finite intensity around the reported T_{Tilt} (and above the contraction of the lattice in the non-polar direction) similar to that observed near second order or weakly first order transitions, including those in $LaAlO_3$ and $SrTiO_3$.[11-14] The increase in the FWHM of the superlattice reflection above the reported T_{Tilt} (plotted in Figure 5.3 along with integrated intensity) suggests that the correlation length is decreasing, indicating that the transition is not a simple "turning on" of the tilt. It is unclear at the moment if this is true short-range order, a decrease in the correlation length of the long-range order, a decrease in the amplitude of the tilt, or combinations thereof. The gradual increase in FWHM however, indicates that the transition is not first order in character. Thus, the reported tilt transition is not abrupt, but has an extended temperature regime with local or weak tilting present

above the previously reported T_{Tilt}. This will be referred to as the region of "non-zero-tilt".
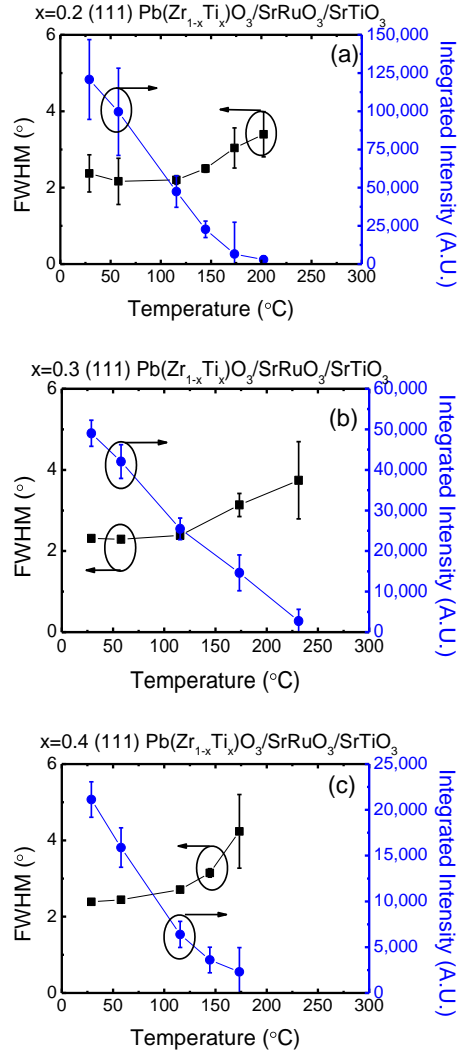
Figure 5.3. Integrated intensity of the ½{311}$_{pc}$ reflection and corresponding full width at half maximum of the φ scans for relaxed Pb(Zr$_{1-x}$Ti$_x$)O$_3$ films with (a) x=0.2, (b) x=0.3, and (c) x=0.4. The increase in FWHM indicates local tilting present within the films at temperatures above bulk T_{Tilt}.

5.1.2 Transmission Electron Microscopy

Figure 5.4 shows dark field TEM images of the PZT samples with compositions of $x = 0.2$, 0.3 and 0.4. These images were recorded close to the $<001>_{pc}$ zone axis. Similar images were recorded for $\{111\}_{pc}$ oriented films but are not shown here. Relatively flat growth surfaces and sharp interfaces between PZT and $SrRuO_3$ are evident. Planar defects running approximately perpendicular to the substrate are present in all films. Unambiguous identification of the origin of these defects was difficult to achieve. The most likely possibilities however are growth defects resulting from mosaicity during film growth or ferroelectric domain walls. From simple geometric criteria, ferroelectric domains walls in rhombohedral PZT conventionally lie on either $\{110\}_{pc}$ or $\{100\}_{pc}$ planes. Careful dark field studies using the appropriate two beam condition should elucidate the criteria $g.R = 0$ and $g.R \neq 0$ where R is the displacement vector of the planar defect and g is the reciprocal lattice vector. The absence of any condition for 'invisibility' for the planar defects utilizing $\{001\}_{pc}$ and $\{110\}_{pc}$ type reflections indicates that they do not have low order habit planes and favors the argument that they are growth defects rather than ferroelectric domains.
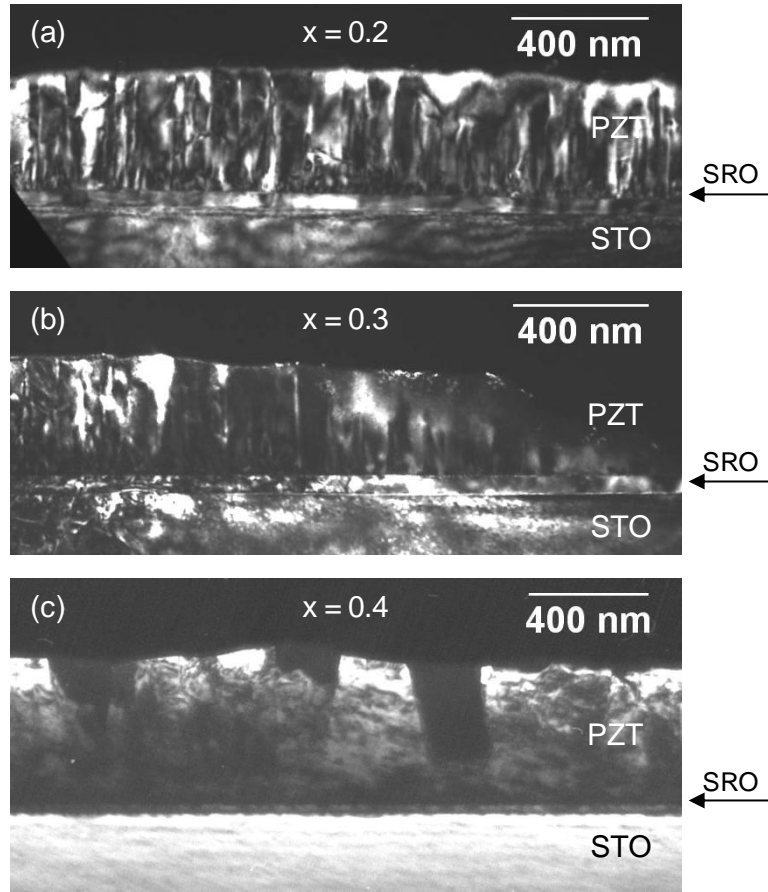
Figure 5.4. Dark field TEM images recorded close to the $<100>_{pc}$ zone axis for the compositions of (a) x = 0.2, (b) x = 0.3 and (c) x = 0.4, respectively.

Representative selected area electron diffraction patterns taken along the $<110>_{pc}$ zone axes at room temperature are shown in Figure 5.5. For films with x = 0.2 and 0.3, a well-defined pseudocube-on-pseudocube orientation relationship between the PZT layers and the underlying substrates was confirmed, Figure 5.5(a) and (b). The selected area aperture (~0.2 μm diameter on screen) covers several domains in the images which presumably gives rise to the splitting of the diffraction spots observed in Figure 5.5(c). The splitting cannot be indexed according to a conventional twin domain relationship, which further suggests that planar defects separate crystallographically misaligned

regions formed during film growth. In addition to fundamental reflections, Figure 5.5 (a) and (b) also reveal superstructure reflections at $\frac{1}{2}\{ooo\}_{pc}$ positions (where the o denotes an odd index, as described by Glazer),[15] attributed to antiphase rotations of the O octahedra and associated with R3c rather than R3m symmetry.[2,16] If the diffraction patterns in Figure 5.5 are qualitatively compared, it is evident that $\frac{1}{2}\{ooo\}_{pc}$ superlattice reflections decrease in intensity with increasing Ti concentration (x= 0.2 > 0.3) and eventually disappear (x = 4). This is consistent with the bulk $PbZr_{1-x}Ti_xO_3$ phase diagram.[1]

| x = 0.2 | x = 0.3 | x = 0.4 |
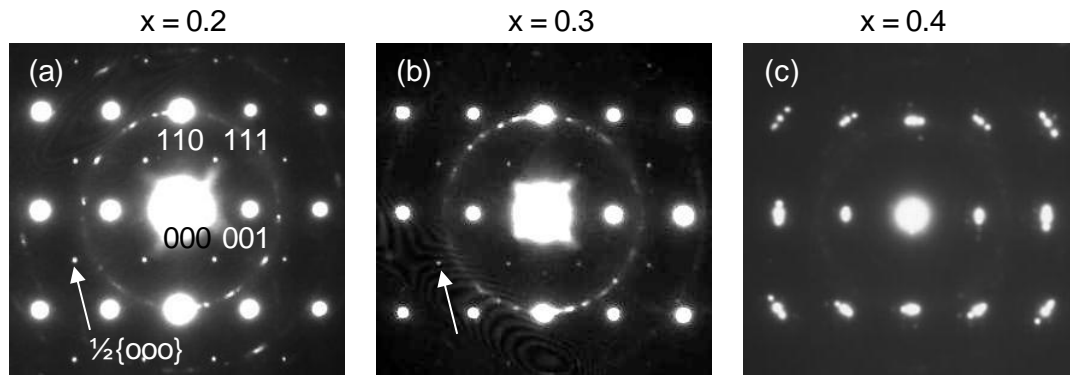
Figure 5.5. $<110>_{pc}$ zone axis electron diffraction patterns recorded at room temperature for the compositions of (a) x = 0.2, (b) x = 0.3 and (c) x = 0.4, respectively. The weak polycrystalline ring pattern observed in some electron diffraction patterns is an artifact of the ion thinning process in which nanocrystals form at the TEM foil surface as a result of PbO loss. The effect is well known and does not influence the diffraction data obtained from the bulk of the foil, but does increase the diffuse background intensity.

To study further the onset of octahedral tilting (at temperature T_{Tilt}), samples were either heated (x = 0.2 and 0.3) or cooled (x = 0.4) within the microscope (Figure 5.6). As evidenced by the appearance or disappearance of the ½{ooo}$_{pc}$ type superlattice spots, T_{Tilt} for each composition was ~130°C, 100°C and -160°C for x = 0.2, 0.3 and 0.4, respectively. This data was recorded from samples in cross section. As a result, in addition to ½{ooo} reflections from the R3c PZT phase, ½{ooo} superstructure reflections from the SrRuO$_3$ (a$^-$a$^-$c$^+$, Pbnm) electrode are also observed in some patterns. If these are present, then the equivalent fundamental reflections from SrRuO$_3$ appear adjacent to those of PZT and the pertinent superstructure reflections associated with the R3c phase can be readily distinguished (arrowed in Figure 5.6).

Although long exposure electron diffraction patterns are considered sensitive to short range or short coherence order, it is difficult in these samples to identify unambiguously, weak diffuse ½{ooo}$_{pc}$ reflections from PZT above T_{Tilt}. Accurate observation of diffuse scatter in electron diffraction patterns requires very low background intensity of the diffuse scatter from other sources. Here the proximity of the amorphous glue in cross sectional samples and the presence of an ion-beam/electron beam damage layer on the surface of the PZT have resulted in a strong background intensity of diffuse scatter, above which it is difficult to observe diffuse reflections. Moreover, in many cases the equivalent discrete reflection from the SrRuO$_3$ electrode layer is present which raises the background intensity in the vicinity of the ½{ooo}$_{pc}$ positions. It is therefore concluded that observation of diffuse short coherence ½{ooo}$_{pc}$

is unreliable in electron diffraction given the limitations of sample preparation described here.
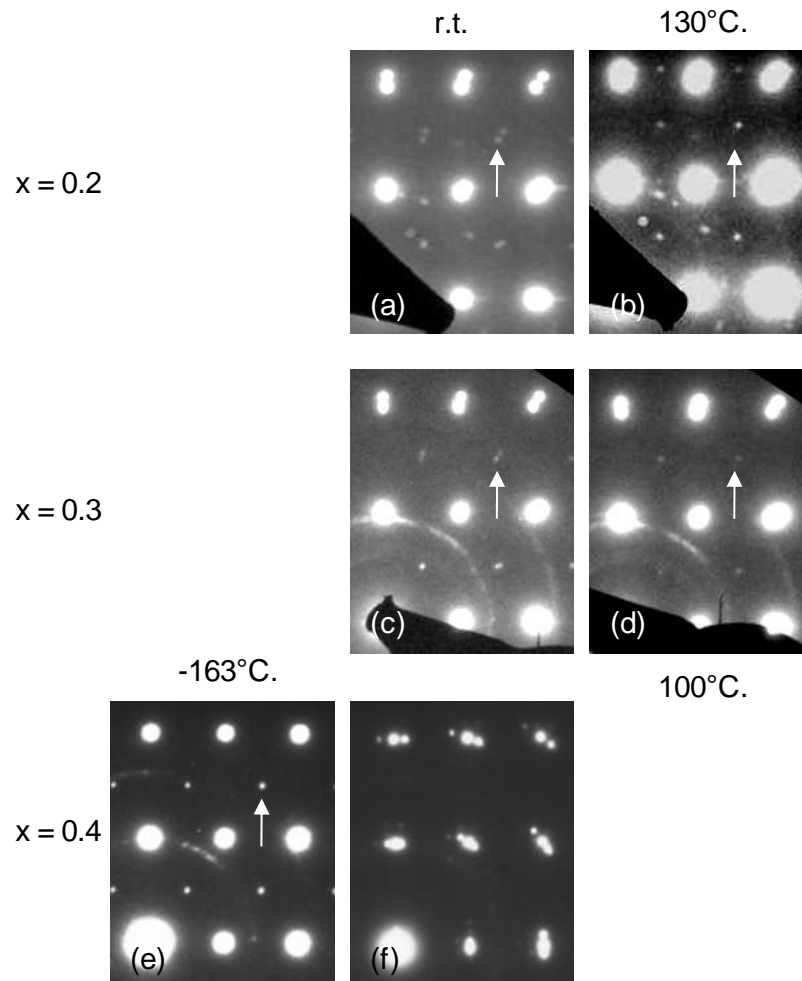
Figure 5.6. $<110>_{pc}$ zone axis electron diffraction patterns for composition of x = 0.2, recorded at (a) room temperature and (b) 130°C, respectively; $<110>_{pc}$ zone axis electron diffraction patterns for composition of x = 0.3, recorded at (c) room temperature and (d) 100°C, respectively; $<110>_{pc}$ zone axis electron diffraction patterns for composition of x = 0.4, recorded at (e) -163°C and (f) room temperature, respectively. Arrows indicate ½{ooo} reflections from the PZT layer.

5.2 *Electrical Characterization of Pb(Zr$_{1-x}$Ti$_x$)O$_3$ Thin Films*

5.2.1 Relative Permittivity Studies

Electrical measurements were also conducted to assess the phase transition temperatures. Thick relaxed films were shown to exhibit room temperature permittivities of 400-500 with loss tangents less than 5%, as shown in Figure 5.7(a-c). The electrical quality of the films is high; the loss tangents remain low up to 400°C. A clear maximum in the dielectric permittivity is observed for each composition at T_C. The relaxed PZT films exhibited T_C within 20 °C of those reported for bulk PZT Curie temperatures. There is no clear signature in either the dielectric constant or loss data that corresponds to T_{Tilt} for any of the films. The inverse of the permittivity as a function of temperature is shown in Figure 5.7(d-f). From the high temperature data, the Curie-Weiss constants were found to be within 15% of those of bulk materials.[17]   Similarly, it is observed that there is a deviation from linear behavior at temperatures between the reported T_{Tilt} and T_C. Similar behavior was reported previously for bulk PZT ceramics and was attributed to the presence of local tilting.[18]   Plotting the inverse permittivity with the integrated intensity of the ½{311}$_{pc}$ peak, it is apparent that the deviation from linear behavior correlates with the appearance of the tilt superlattice reflection.

Additionally, the temperature dependent properties of poled films were measured. The films were poled either at room temperature with ~3 times the coercive field for 1 hour or at 150°C for 20 minutes. In either case, the samples were aged for 1 hour and the relative permittivity and loss tangent were measured on heating. The films exhibited similar permittivity maxima at T_C to those of unpoled films. It was found that there was

no consistent indication of the tilt transition in the loss tangent. There was a deviation from linearity in the inverse permittivity data of poled samples, however, that was at temperatures above which were observed for the tilt transition observed from x-ray diffraction. Deviations such as this have been seen in the work of Dai, Xu and Viehland in bulk ceramics. Their materials, however, had a characteristic pinching of the hysteresis loop indicative of Pb and O vacancies. To assess whether comparable phenomena were responsible for the temperature anomalies in films, low field minor hysteresis loops were performed on the samples. No evidence for pinched hysteresis loops was detected as evidenced in the representative sample shown in Figure 5.8.
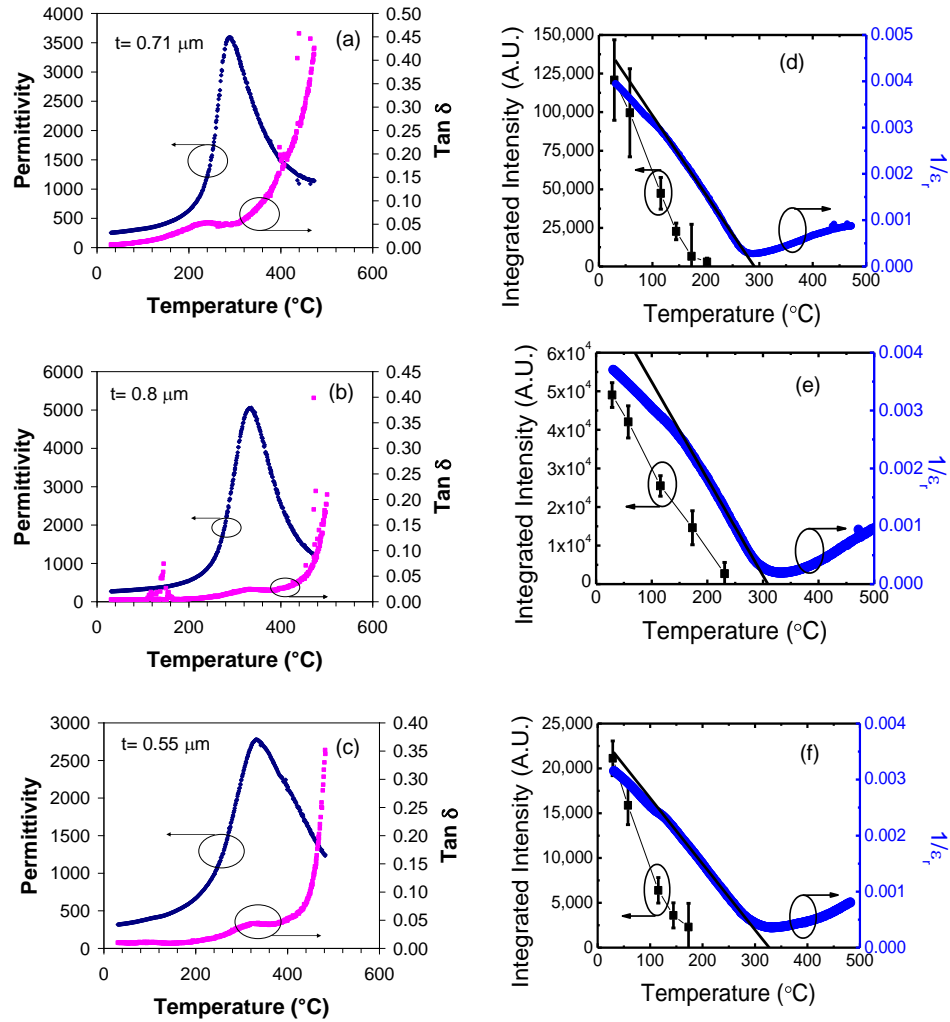
Figure 5.7. Relative permittivity and loss tangent vs. temperature for samples with composition (a) x=0.2, (b) x=0.3 and (c) x=0.4 at 10 kHz and $1/\varepsilon_r$ vs temperature for films with (d) x=0.2, (e) x=0.3, and (f) x=0.4 plotted with corresponding integrated intensities of the ½{311}$_{pc}$ peak. The appearance of intensity at the ½{311}$_{pc}$ peak correlates with a dielectric anomaly within the films. (The solid lines are linear fits to the experimental data to illustrate the deviation from linearity.)
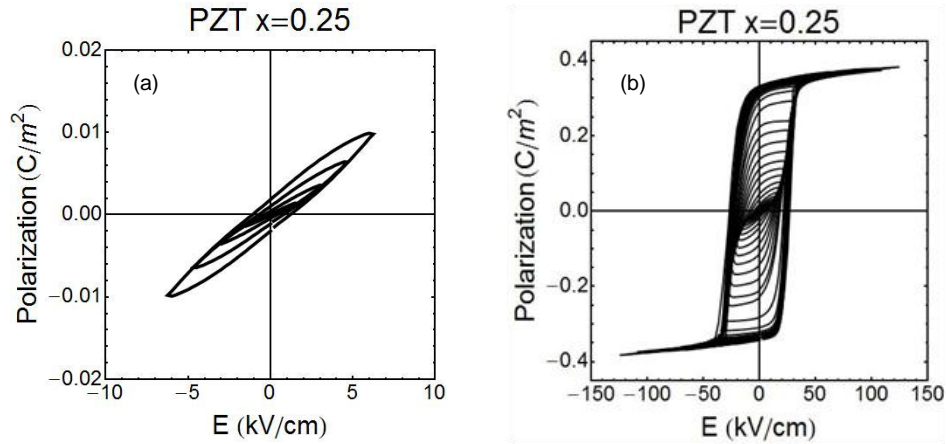
Figure 5.8.   (a) Minor loops for a representative film showing no pinching associated with Pb-O vacancy defect dipoles and (b) evolution of the hysteresis loop for a film with x=0.25.

5.2.2 Polarization Studies

The switchable polarization (P_{SW}) was measured as a function of temperature using the PUND technique to compensate for leakage at high temperatures. Because the paraelectric - ferroelectric phase change is second order,[9] the spontaneous polarization scales with the square root of temperature below T_C, while octahedral tilting leads to a small step in the spontaneous polarization.[19] Figure 5.9(a-c) shows the values for P_{SW}^2 plotted with the integrated intensities of the ½{311}$_{pc}$ peak as a function of temperature. At high temperatures, P_{SW}^2 follows a linear dependence. A deviation from linearity is observed above the reported T_{Tilt}. As was the case for the inverse permittivity, the deviation from linearity instead coincides with the appearance of the weak, broad ½{311}$_{pc}$ peak.   The PUND measurements showed that the coercive field initially decreased on increasing temperature, and then leveled off at temperatures typically above ~200-250°C. This leveling off is presumably because of leakage that inflated the E_C

values at high temperatures. However, there was no observable link between the appearance of the superlattice reflection and the coercive field measured through this technique.
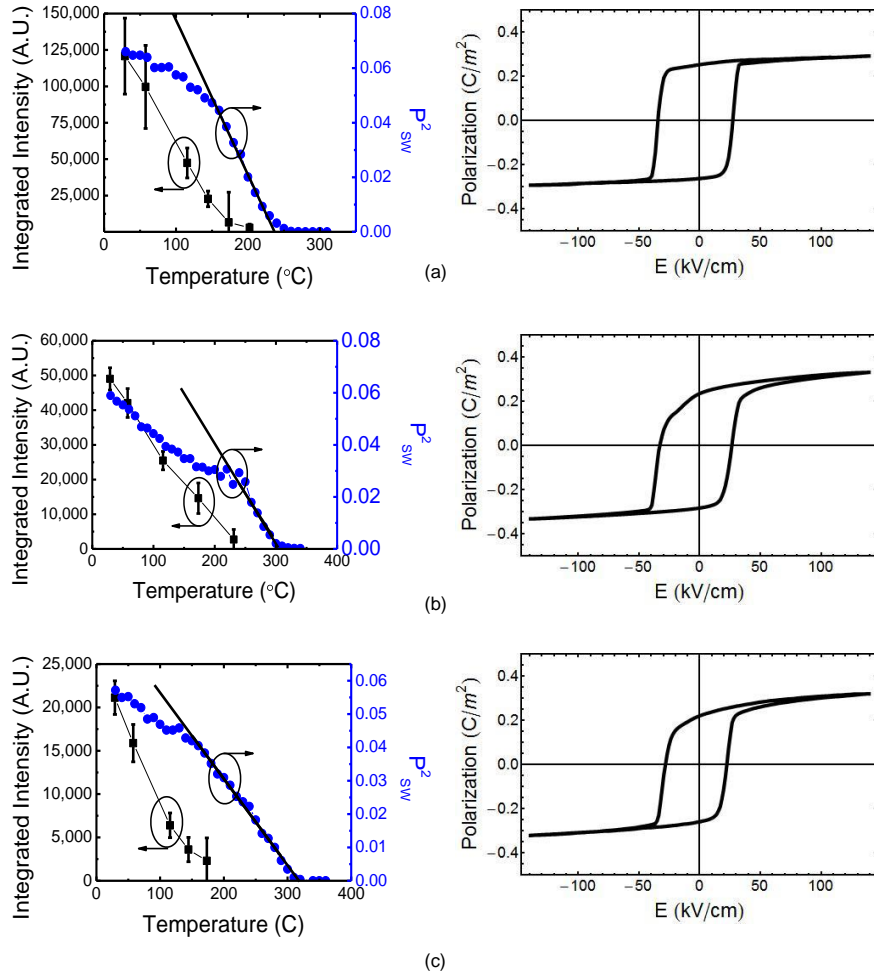
Figure 5.9. P^2_{SW} shown with the integrated intensity of the ½{311}$_{pc}$ reflection to illustrate the effects of local tilting on the switchable polarization of the film for samples with (a) x=0.2, (b) x=0.3, (c) x=0.4. Also shown are the room temperature hysteresis loops for the compositions. (The solid lines are linear fits to the experimental to illustrate the deviation from linearity.)

5.3 *Pb(Zr$_{1-x}$Ti$_x$)O$_3$ Phase Diagram*

As a model system to study octahedral tilting, Pb(Zr$_{1-x}$Ti$_x$)O$_3$ films with x=0.2-0.4 were investigated as described above. Films with thicknesses greater than 350 nm had permittivities in the 400-500 range with loss tangents less than 3% at 10 kHz with Curie temperatures similar to bulk ceramics. However, it was found from electrical and structural measurements that T$_{Tilt}$ is not between tilted and un-tilted states, but rather between a region of no tilt, to a region of non-zero-tilt, to long-range coherent tilting occurring near the reported T$_{Tilt}$. This explains anomalies in the temperature dependence of the relative permittivity and switchable polarization of thin films. As a result, it is possible to redraw the phase diagram for these PZT films, as shown in Figure 5.10. The base diagram was taken from the work of Woodward, Knudsen and Reaney.[1] The diagram is modified to include the transition from non-zero-tilting to the untilted phase. A summary of the phase transition temperatures reported for bulk PZT[1,20] is compared to those of the relaxed films in Table 5.2. As was discussed above, no attempt was made to examine lead displacements, so the possibility of a monoclinic distortion as described by Glazer et al.[21] and Yokota et al.[7] could not be verified here.

T$_{Tilt}$ as indicated in the phase diagram for these films is no longer considered as the onset of temperature of tilting but rather the temperature at which the lattice contracts in the <111>$_{pc}$ direction as a result of spontaneous strain arising from tilting. A detailed phenomenological description of the complex interactions of polarization, strain, and amplitude of tilt is now required; from a simple mechanistic perspective, tilted regions

92

form above T_{Tilt} with a weak amplitude of rotation and limited correlation length. On further cooling, the amplitude and correlation length increase and at T_{Tilt} the resulting spontaneous strain couples to that of the conventional paraelectric-ferroelectric transition.
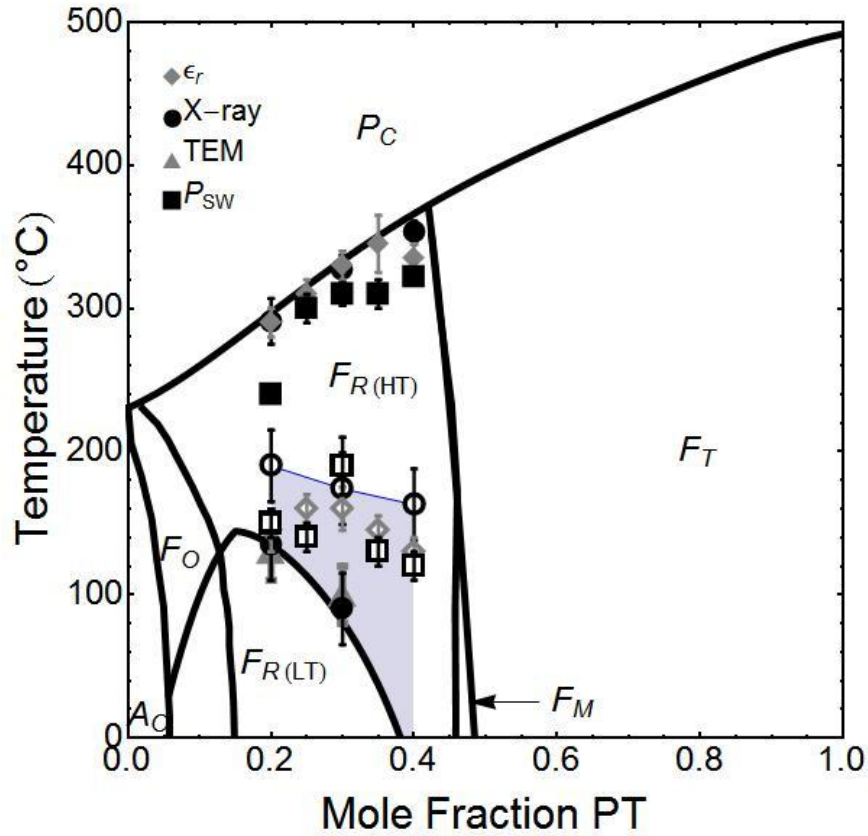
Figure 5.10. Pb(Zr$_{1-x}$Ti$_x$)O$_3$ thin film phase diagram measured by various techniques. Filled symbols denote the ferroelectric and tilt transitions whereas open symbols denote the region of non-zero-tilt. F denotes the ferroelectric phase, A an antiferroelectric phase, and P the paraelectric phase. The subscripts T, M, R, O, and C refer to the tetragonal, monoclinic, rhombohedral, orthorhombic, and cubic phases. LT and RT refer to low temperature and high temperature phases, respectively. The shaded region is the region of non-zero tilt observed within the films.

Table 5.2 Phase transition temperatures for relaxed $Pb(Zr_{1-x}Ti_x)O_3$ thin films.

Error bars are given in the parentheses following each number.

		Bulk	Thin Film				
		Phase Diagram[1,20]	ε_r	P_{SW}	Spontaneous Strain	Integrated Intensity ½{311}	Electron Diffraction
x=0.2	T_C (°C)	297	290(10)	247(3)	291(11)		
	T_{NZT} (°C)	179	145(15)	150(10)		200(25)	
	T_{Tilt} (°C)	134			135(25)		130
x=0.25	T_C (°C)	315	310(10)	300(10)			
	T_{NZT} (°C)	174	160(10)	140(10)			
	T_{Tilt} (°C)	113					
x=0.3	T_C (°C)	333	330(10)	310(8)	327(20)		
	T_{NZT} (°C)	167	160(15)	190(20)		200(25)	
	T_{Tilt} (°C)	81			90(25)		100
x=0.35	T_C (°C)	350	345(20)	310(10)			
	T_{NZT} (°C)	160	145(10)	130(10)			
	T_{Tilt} (°C)	37					
x=0.4	T_C (°C)	366	335(10)	322(5)	353(16)		
	T_{NZT} (°C)	152	130(15)	120(10)		170(25)	
	T_{Tilt} (°C)	-27			<RT		<RT

5.4 *References:*

[1]D. I. Woodward, J. Knudsen, and I. M. Reaney, "Review of crystal and domain structures in the PbZr$_x$Ti$_{1-x}$O$_3$ solid solution," *Physical Review B,* **72**[10] 104110 (2005).

[2]A. M. Glazer, "Classification of tilted octahedra in perovskites," *Acta Crystallographica Section B-Structural Science,* **B 28**[Nov15] 3384-92 (1972).

[3]B. Noheda, J. A. Gonzalo, A. C. Caballero, C. Moure, D. E. Cox, and G. Shirane, "New features of the morphotropic phase boundary in the Pb(Zr1-xTix)O-3 system," *Ferroelectrics,* **237**[1-4] 541-48 (2000).

[4]D. L. Corker, A. M. Glazer, R. W. Whatmore, A. Stallard, and F. Fauth, "A neutron diffraction investigation into the rhombohedral phases of the perovskite series PbZr$_{1-x}$Ti$_x$O$_3$," *Journal of Physics-Condensed Matter,* **10**[28] 6251-69 (1998).

[5]M. J. Haun, E. Furman, Z. Q. Zhuang, S. J. Jang, and L. E. Cross, "Thermodynamic theory of the lead zirconate-titanate solid-solution system," *Ferroelectrics,* **94** 313-13 (1989).

[6]B. Jaffe, W. R. Cook Jr., and H. Jaffe, "Piezoelectric Ceramics,*"* pp. 317. Academic Press Ltd. : New York, (1971).

[7]H. Yokota, N. Zhang, A. E. Taylor, P. A. Thomas, and A. M. Glazer, "Crystal structure of the rhombohedral phase of PbZr$_{1-x}$Ti$_x$O$_3$ ceramics at room temperature," *Physical Review B,* **80**[13] 104109 (2009).

[8]Y. S. Touloukian, "Thermal Expansion--Nonmetallic Solids." in Thermophysical Properties of Matter*,* **Vol. 13.** IFI/Plenum, 1977.

[9]M. J. Haun, E. Furman, S. J. Jang, and L. E. Cross, "Thermodynamic theory of the lead zirconate-titanate solid-solution system, .1. phenomenology," *Ferroelectrics,* **99** 13-25 (1989).

[10]M. J. Haun, E. Furman, H. A. McKinstry, and L. E. Cross, "Thermodynamic theory of the lead zirconate-titanate solid-solution system, .2. Tricritical behavior," *Ferroelectrics,* **99** 27-44 (1989).

[11]M. Lambert and R. Comes, "Chain structure and phase transition of $BaTiO_3$ and $KNbO_3$," *Solid State Communications,* **7**[2] 305-08 (1969).

[12]G. Shirane, R. A. Cowley, M. Matsuda, and S. M. Shapiro, "Q-dependence of the central peak in the inelastic-neutron-scattering spectrum of $SrTiO_3$," *Physical Review B,* **48**[21] 15595-602 (1993).

[13]J. D. Axe, G. Shirane, and K. A. Mueller, "Zone-boundary phonon instability in cubic $LaAlO_3$," *Bulletin of the American Physical Society,* **14**[1] 61-68 (1969).

[14]U. Rutt, A. Diederichs, J. R. Schneider, and G. Shirane, "Depth dependence of strain, mosaicity and sharp component in the critical scattering of $SrTiO_3$," *Europhysics Letters,* **39**[4] 395-400 (1997).

[15]A. M. Glazer, "Simple ways of determining perovskite structures," *Acta Crystallographica Section A,* **31**[Nov1] 756-62 (1975).

[16]E. L. Colla, I. M. Reaney, and N. Setter, "Effect of structural-changes in complex perovskites on the temperature-coefficient of the relative permittivity," *Journal of Applied Physics,* **74**[5] 3414-25 (1993).

[17]M. J. Haun, Z. Q. Zhuang, E. Furman, S. J. Jang, and L. E. Cross, "Thermodynamic theory of the lead zirconate-titanate solid-solution system, .3. Curie constant and 6th-order polarization interaction dielectric stiffness coefficients," *Ferroelectrics,* **99** 45-54 (1989).

[18]X. H. Dai, Z. Xu, J. F. Li, and D. Viehland, "Constriction of the Polarization by Incoherent Oxygen Octahedral Tilting in Rhombohedral-Structured Lead-Zirconate-Titanate," *Journal of Applied Physics,* **77**[7] 3354-60 (1995).

[19]M. J. Haun, E. Furman, S. J. Jang, and L. E. Cross, "Thermodynamic theory of the lead zirconate-titanate solid-solution system, .5. theoretical calculations," *Ferroelectrics,* **99** 63-86 (1989).

[20]X. H. Dai, Z. K. Xu, and D. Viehland, "Effect of oxygen octahedron rotations on the phase-stability, transformational characteristics, and polarization behavior in the lead-zirconate-titanate crystalline solution series," *Journal of the American Ceramic Society,* **78**[10] 2815-27 (1995).

[21]A. M. Glazer, P. A. Thomas, K. Z. Baba-Kishi, G. K. H. Pang, and C. W. Tai, "Influence of short-range and long-range order on the evolution of the morphotropic phase boundary in $Pb(Zr_{1-x}Ti_x)O_3$," *Physical Review B,* **70**[18] 184123 (2004).

Chapter 6   Strained Epitaxial Pb(Zr$_{1-x}$Ti$_x$)O$_3$Thin Films

Because of the clamping imposed by the substrates, the mechanical boundary conditions experienced by films are considerably different compared with those for bulk samples. Most ceramic materials can withstand only a few tenths of a percent of strain before failure.[1]   However, in thin films the strain levels that can be achieved before cracking or delamination can be an order of magnitude higher.[2] With the imposed strain, the electrical properties can change, ferroelectricity can be induced, and the crystal structure can be strain-driven from rhombohedral to tetragonal.[3]

In order to achieve coherently strained films, one must look at the lattice mismatch between the film and the substrate material. For the PZT films studied in this thesis, SrTiO$_3$ was the substrate utilized. The room temperature lattice parameter of SrTiO$_3$ is 3.905 Å,[4] while (as shown in Figure 5.2) the room temperature lattice parameter for relaxed Zr-rich PZT films is 4.10 Å or larger. Coherent films of rhombohedral PZT will then have in excess of 4% in-plane compressive strain. As shown in Figure 6.1, the largest lattice parameter for a commercially available perovskite substrate is that for Pb(Mg$_{2/3}$Nb$_{1/3}$)O$_3$-PbTiO$_3$, which has a lattice parameter of 4.04 Å. This value would provide approximately a 2% in-plane compression for the PZT films in this thesis.
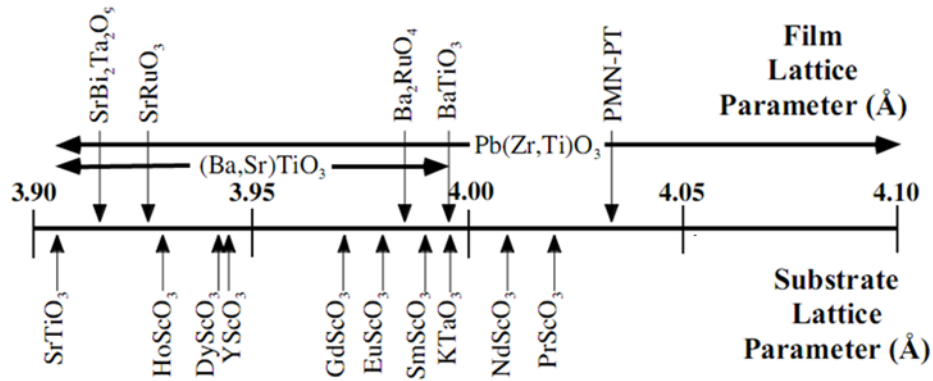
Figure 6.1.   Lattice parameters of several substrate materials and their match to Pb(Zr$_{1-x}$Ti$_x$)O$_3$.[5]

The Matthews-Blakeslee criterion[6] is used to estimate the point at which dislocations are energetically favorable to reduce the strain in coherent films, as shown in Equation 2.5. As illustrated in Figure 6.2(a), this predicts dislocation formation in PZT films on SrTiO$_3$ having a thickness ~4 times the length of the Burgers vector. It has been shown that the Burgers vector in perovskites can be in the <100>$_{pc}$ or the <110>$_{pc}$ directions.[7] If we consider the minimum thickness for dislocation formation at 2% strain, this yields a film of approximately 4 unit cells in thickness. Although somewhat thicker films can often be prepared prior to relaxation, such films may still be too thin for many measurements. To circumvent these limitations, a substrate with $a_{pc} > 4.08$ Å is required.

In lieu of a substrate with the required lattice parameter, it was decided to investigate the use of a buffer layer of relaxed PZT films as a "pseudo-substrate."[8] In order to facilitate investigations of tilt in the coherent films, it is desirable that the buffer

layer be untilted. The bulk pseudo-cubic lattice parameters across the PZT solid solution[4] are shown in Figure 6.2(b). As is shown in the diagram, the narrow, unshaded composition range is suited for use as a buffer layer because of the large lattice parameter and lack of long-range order of octahedral tilt. Thus, strained films with compositions of x = 0.2, 0.25, 0.3, and 0.35 were grown on a buffer layer with a composition of x = 0.4. Due to the change in lattice parameters across the chosen compositions (4.11 - 4.14 Å), changing the composition of the strained layer changes the strain level of the film.

(a)   (b)
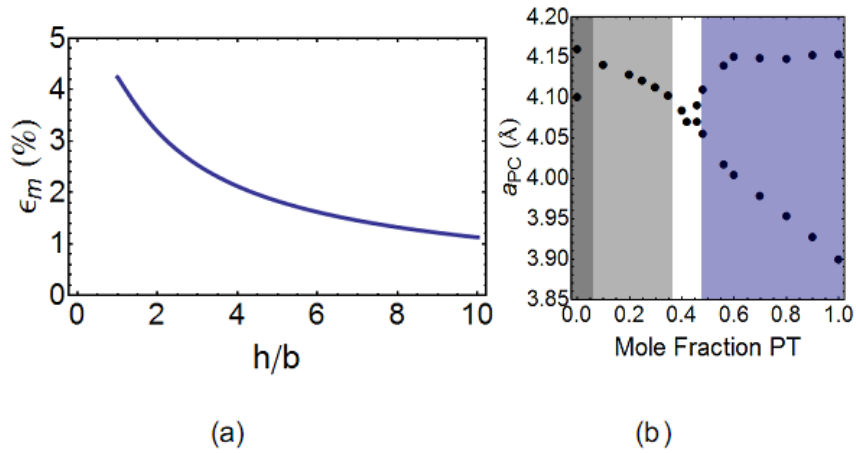
Figure 6.2.   (a) Matthews-Blakeslee criterion for the critical thickness in PZT films and (b) $Pb(Zr_{1-x}Ti_x)O_3$ lattice parameter as a function of $PbTiO_3$ composition.

The buffer layer grown on $SrTiO_3$ to enable preparation of strained PZT layers needs to be sufficiently thick to relax, without generating significant levels of roughness.[9] Based on the Matthews-Blakeslee criterion, one expects the x=0.4 buffer layer to start forming dislocations after only a few unit cells. However, this criterion often underestimates the thickness at which relaxation is complete.[9] Therefore a ~10 nm thick buffer layer was deposited to ensure a relaxed film without significant levels of islanding.

The deposition of the buffer layer was performed as described earlier, with rapid cooling to minimize Pb-loss.[10] Because the chamber was able to accommodate only one PLD target at a time, it was necessary to break the vacuum and switch targets. This was done while the buffer layer was still hot (~200 °C), and the time the sample saw atmospheric pressure was kept to a minimum. Once the targets were switched, the chamber was evacuated using a mechanical pump and the substrate temperature was increased to 300-400°C. This minimized the amount of time required to heat the sample to the deposition temperature while keeping the sample cool enough to prevent Pb-loss. The sample was maintained at elevated temperatures while the chamber was evacuated to low pressures using the diffusion pump. The chamber was filled with the O_2/O_3 mixture and brought to the desired deposition pressure. At this point, the sample was heated as quickly as possible to the deposition temperature and the deposition was immediately performed, so that the buffer experienced a minimal amount of time at temperatures in excess of 600°C.[10] Following growth, the sample was cooled quickly.

6.1 *(001)$_{pc}$ Oriented Strained Films*

A representative x-ray diffraction pattern for a strained film is shown in Figure 6.3 for a 10 nm, x = 0.2 film on a 10 nm buffer layer with x = 0.4. The modulated thickness fringes in Figure 6.3(a) show that the surface of the film and the interface between the two films is parallel to the substrate and smooth. Figure 6.3(b) is a ϕ scan of the strained film's 101_{pc} peak exhibiting epitaxy. Figure 6.3(c) shows the in and out of plane lattice parameter for the as-deposited bi-layer. For the x=0.4 buffer layer, the out-of-plane lattice parameter and the in-plane lattice parameter are similar. The difference

may stem from either incomplete relaxation or a slight difference due to the thermal expansion mismatch of the film and substrate. However, the in-plane lattice parameter for the x=0.2 strained layer is identical to that of the x=0.4 buffer layer within experimental error, suggesting a coherently strained film.

These observations are consistent with the observation of misfit dislocations at the $Pb(Zr_{0.6}Ti_{0.4})O_3/SrTiO_3$ interface but not between the two PZT layers (results shown below) in the high-resolution TEM image shown in Figure 6.3(d). To achieve this image, bright-field high-resolution TEM was performed on the film and the image was processed using a fast Fourier transform (FFT). A digital mask was used to isolate the intensity from the Bragg peaks in the diffraction pattern. This filtered diffraction pattern was processed through an inverse Fourier transform (IFT) to achieve a filtered real-space image of the film. The lack of observable misfit dislocations at the interface between the strained layer and the buffer layer confirms that the x=0.2 film is coherently strained to the buffer layer.
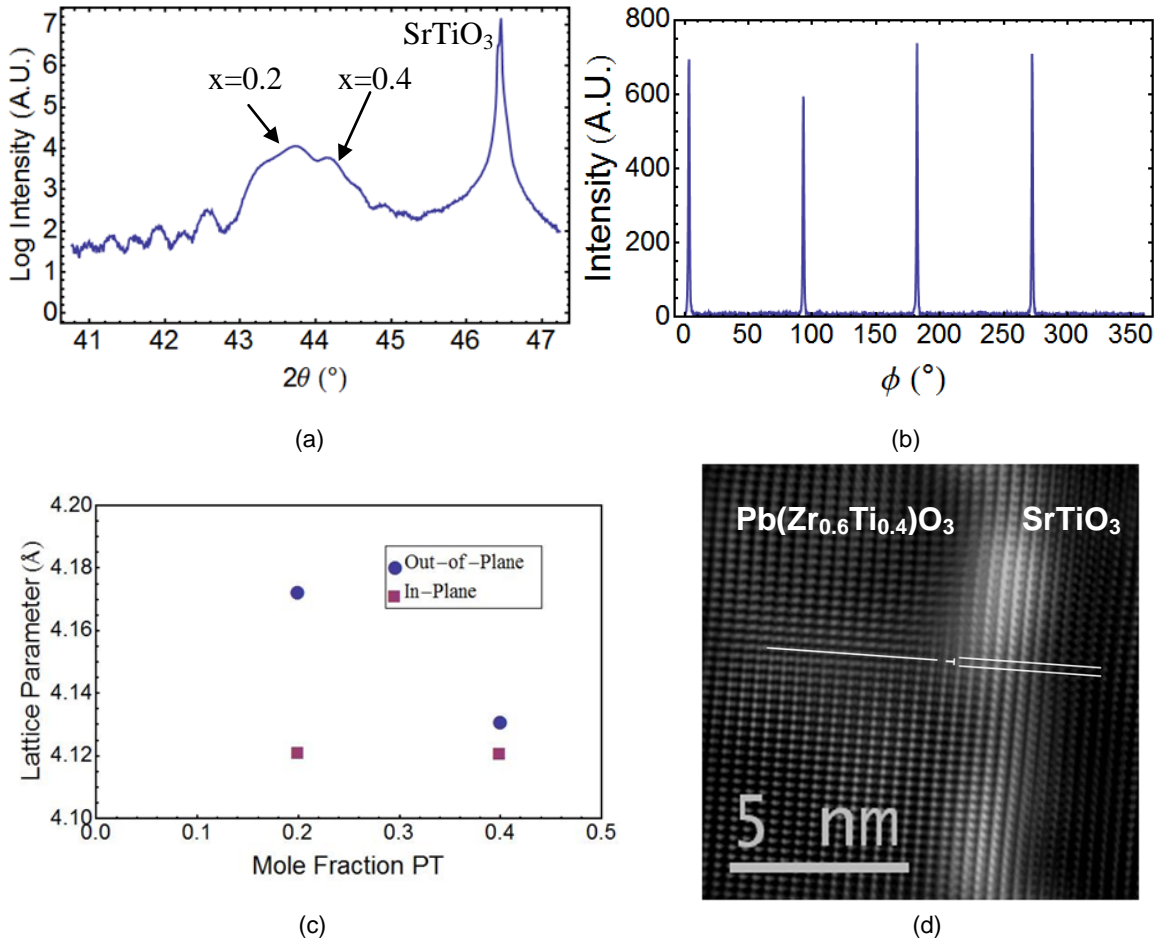
Figure 6.3. (a) $2\theta-\theta$ scan of 10 nm strained x = 0.2 PZT on 10 nm x = 0.4 PZT buffer layer; the unlabeled peaks correspond to thickness fringes (b) ϕ scan on the $\{101\}_{pc}$ peak on film peaks, showing epitaxy; (c) the in and out-of-plane lattice parameters for the x=0.4 buffer layer and x=0.2 strained layer: and (d) high-resolution TEM image of the PZT/SrTiO$_3$ interface, showing a misfit dislocation.

Figure 6.4 shows a dark field TEM taken along the $<110>_{pc}$ zone axis of a bi-layer sample. As can be seen, there is a clear interface between the SrTiO$_3$ and the PZT. The inset in Figure 6.4 shows the selected area diffraction pattern of the bi-layer,

illustrating its epitaxial nature. From the image, it is possible to see that the entire thickness of the bi-layer is ~30 nm. The image shows strain contrast, which only occurs within the bottom 15 nm (e.g., the buffer layer of PZT x=0.4). This is due to the presence of dislocations within the buffer layer as evidenced in Figure 6.3(d). This is shown in more detail in Figure 6.3(d), where a dislocation is marked by the discontinuity in the atomic columns. Drawing a Burger's circuit around the dislocation shows that the Burger's vector length of one unit cell is consistent with that for perovskites.[7]
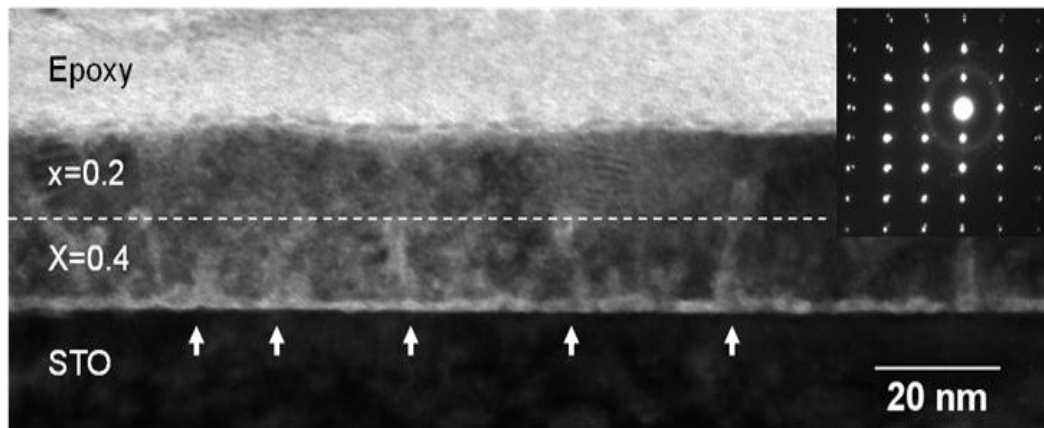
Figure 6.4.   Dark-field TEM images for a bi-layer film (inset is the selected area diffraction pattern for the film). The arrows indicate the presence of dislocations.

High-resolution TEM was performed on these samples to determine the coherency of the interfaces within the PZT; results are shown in Figure 6.5. The atomic columns within the bi-layer sample show good registry between the film and the substrate.

The high-resolution TEM image gives a real-space image of the atomic locations, while diffraction gives the positions within reciprocal space. A Fourier transform was

performed on the selected regions shown in order to yield something similar to an electron diffraction image. Regions were selected in both the buffer layer and the strained layer to investigate the presence of octahedral tilting through inspection of the superlattice spots. The image was taken along the $<110>_{pc}$ zone axis, which is one of the zone axes that will allow observation of the superlattice reflection. The Fourier transforms are shown in the insets in Figure 6.5. The Fourier transform on the selected regions show no presence of a superlattice reflection from the buffer layer, yet it shows evidence of there being a superlattice reflection from the strained $x = 0.2$ layer. This suggests the presence of octahedral tilting within the strained layer.
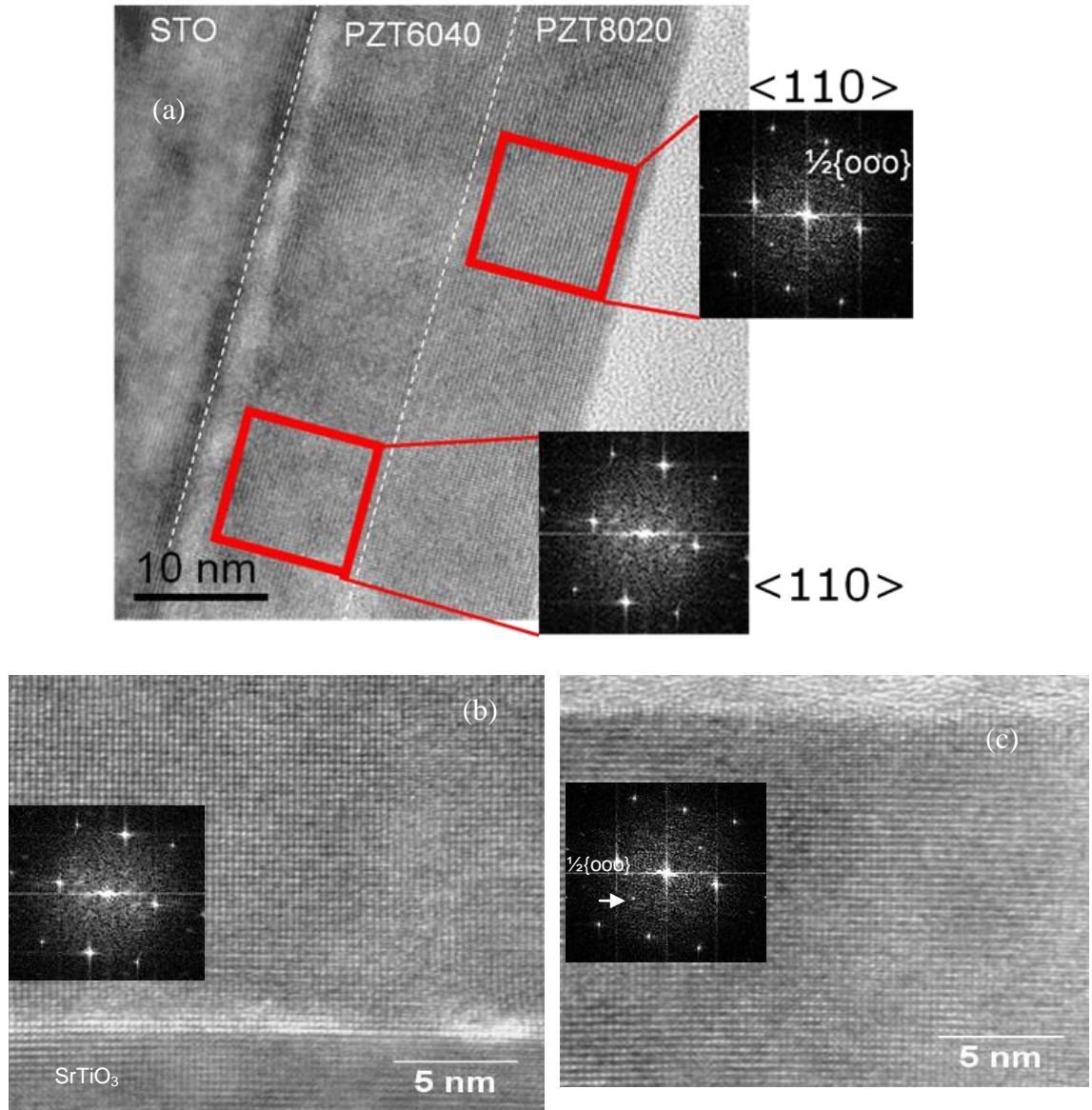
Figure 6.5.   (a) High-resolution TEM image of a representative bi-layer sample with calculated diffraction patterns for the strained and buffer layer of the films; (b) enlargement of the high-resolution TEM image of the buffer layer; and (c) enlargement of the high-resolution TEM image of the strained layer, with the calculated diffraction pattern illustrating presence of octahedral tilting.

From the calculated electron diffraction patterns, high-frequency filters were applied to remove the noise.[†] The Bragg peaks were removed as well, to leave only the superlattice reflections. Then, an inverse Fourier transform (iFFT) was applied to the electron diffraction pattern to get a clearer real-space image of the sample. This procedure is shown in Figure 6.6. From the calculated real-space image in Figure 6.6, it is possible to see that the tilt domains within the strained layer are small, on the order of 3-5 nm. This is consistent with the small coherent scattering size calculated from the FWHM of the superlattice reflection of the films was ~2-5 nm.

[†] The help of Weiguo Lu is gratefully acknowledged.
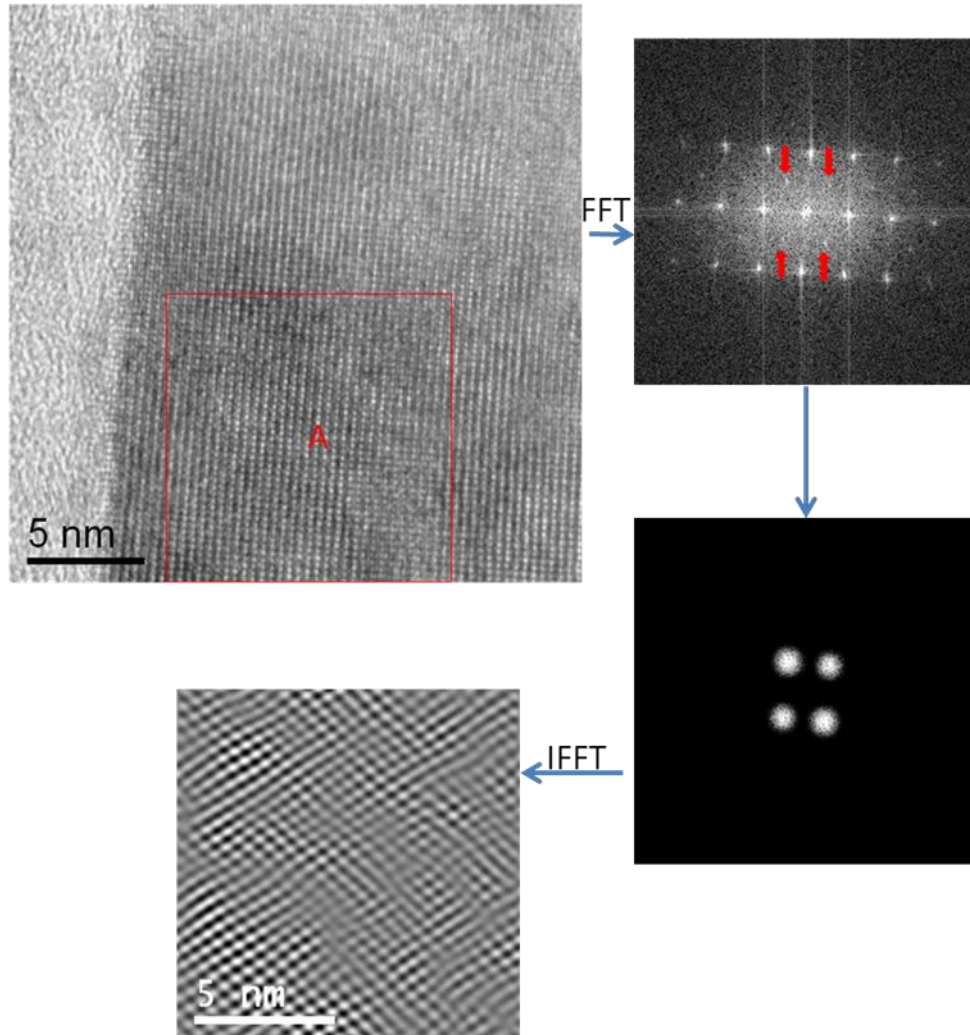
Figure 6.6. High resolution TEM image of the strained layer with corresponding calculated electron diffraction image, filtered electron diffraction, and the calculated real space image of the tilt domains within the sample. FFT is a fast-Fourier transform.

The room temperature out-of-plane lattice parameters for the strained bi-layers on (100) $SrTiO_3$ are plotted in Figure 6.7(a), along with the lattice parameters for relaxed films. As shown in the figure, the out-of-plane lattice parameters for the strained films are larger than those for relaxed films, indicating that they are in compressive in-plane

strain as deposited. This is to be expected from the lattice parameter mismatch. When the lattice parameter of the relaxed films is compared with the lattice parameter for bulk material, we see that there is a slight increase in lattice parameter with respect to bulk, which is likely a result of ion bombardment during deposition.[11] Using Figure 6.1, it is possible to calculate the out-of-plane lattice parameter mismatch relative to the buffer layer for the films, assuming that the relaxed buffer layer has the same values for the in-plane and out-of-plane lattice parameters. This assumption would not be absolutely correct for partially (rather than fully) relaxed buffer layers, but is a reasonable starting point. As can be seen in Figure 6.7(b), the strain scales from ~0.4 to 0.9 % with composition. This demonstrates that changing the Zr/Ti ratio of the film is a valid method for changing the strain of tilted films in the $Pb(Zr_{1-x}Ti_x)O_3$ system.
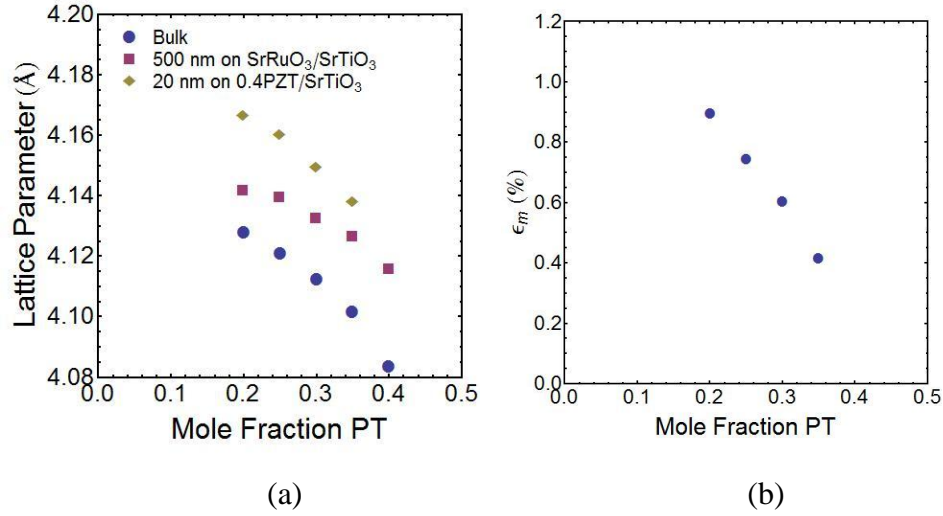
Figure 6.7. (a) Lattice parameter as a function of composition for bulk, relaxed and strained films and (b) misfit strain relative to (100) relaxed films as a function of composition.

Temperature-dependent synchrotron x-ray diffraction measurements were performed on the strained samples at the Advanced Photon Source at Argonne National Laboratory to determine the Curie temperature and the tilt transition temperature. The out-of-plane lattice parameters of the PZT films were measured using the 006_{pc} reflection. The sample was heated to 600°C, and the 006_{pc} reflection was measured every 25°C during cooling. The peaks were fitted using a pseudo-Voigt profile to determine peak position; the goodness of the fits obtained is shown in Figure 6.8(a-d). From the d-spacing calculated by fitting the profiles at each temperature, the out-of-plane d-spacing for the strained films can be extracted; this is shown in Figure 6.8(e). By assuming that the material is in the paraelectric cubic region at high temperatures and experiences a linear thermal expansion, a straight line can be used to calculate the thermal expansion of the material at high temperatures. Linear fits to the experimental data in Figure 6.8(e)

over the 200–400°C range were performed to extract the Curie temperature of the film (this works out to be very similar to the point where the lattice parameter deviates substantially from the thermal expansion of the paraelectric region). From this, the T_C of the films is shown to increase linearly with strain (Figure 6.8(f)) up to 150°C above that observed for bulk or relaxed films. This result is consistent with other compressively strained ferroelectric films.[12] In Figure 6.8(f) the solid line is the calculated shift in T_C due to biaxial strain from phenomenology.[13-15] The equation used to calculate ΔT_C was given in the work of Choudhury, Li and Chen and is given in Equation 6.1:[15]

$$\Delta T_C = 2C\varepsilon_o \frac{2Q_{12}}{s_{11} + s_{12}} x$$

Equation 6.1. Change in T_C as a function of strain

where C is the Curie constant, ε_o is the permittivity of free space, Q_{12} is the electrostrictive constant, s_{11} and s_{12} are compliance coefficients, and x is the strain. The values for the Curie constant and electrostrictive constant were that found by Haun[13] and the compliance were reported by Pertsev et al.[14] As shown, the recorded change in T_C was less than that predicted by this equation. Assuming that the electrostrictive constant changes for films and using this equation to fit to the experimental data, it is found that the electrostrictive constant is lowered by a factor of 2 relative to the reported bulk values.
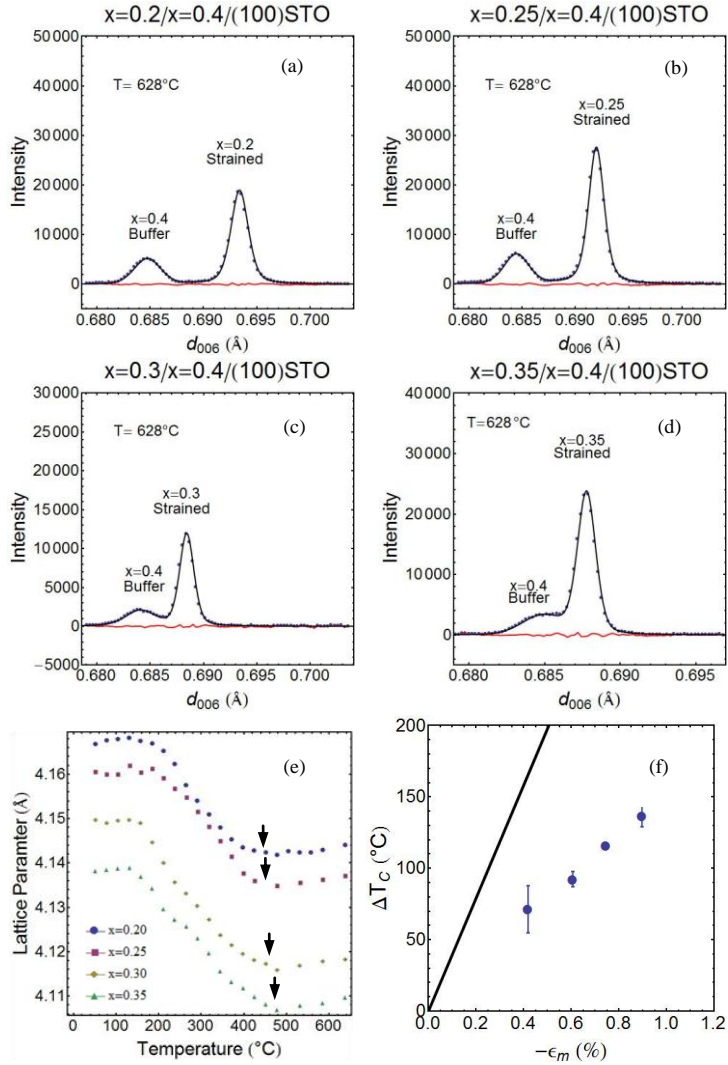
Figure 6.8. X-ray profiles for strained (a) x = 0.2, (b) x = 0.25, (c) x = 0.3, and (d) x = 0.35 on relaxed x = 0.4 on (100) $SrTiO_3$ above the T_C of the films; (e) shows the d-spacing as a function of temperature for all compositions, and (f) shows the relative increase in T_C as a function of strain within these films. The points are experimental data; the black line, the two-peak pseudo-Voigt fit; and the red line, residuals from the fit. Arrows in (e) denote T_C. The solid line in part (e) is the T_C shift calculated from phenomenology.[13-15]

As the films were cooled, the ½{311}$_{pc}$ peak was investigated for the presence of intensity due to rotation of the oxygen octahedra within the perovskite crystal structure. As was the case for the relaxed films, finite intensity was observed at temperatures above that of the bulk tilt transition temperature, as seen in Figure 6.9 (compare to the bulk T$_{Tilt}$ given in Table 2.3). The intensity of the superlattice peak (shown in Figure 6.10) can vary with magnitude of the tilt, volume of diffracted region, and domain population, so direct comparison to intensity of the relaxed films and the point at which the peak is absorbed into the background was not performed. For a high-quality epitaxial film, one would expect the FWHM in θ and ϕ to be identical to that of the substrate. As can be seen from the FWHM of the ϕ scan of the strained layer (shown in Figure 6.9), the FWHM is much larger. This may be attributed to the mosaicity present as a result of coherent growth on a mosaic pseudo-substrate.
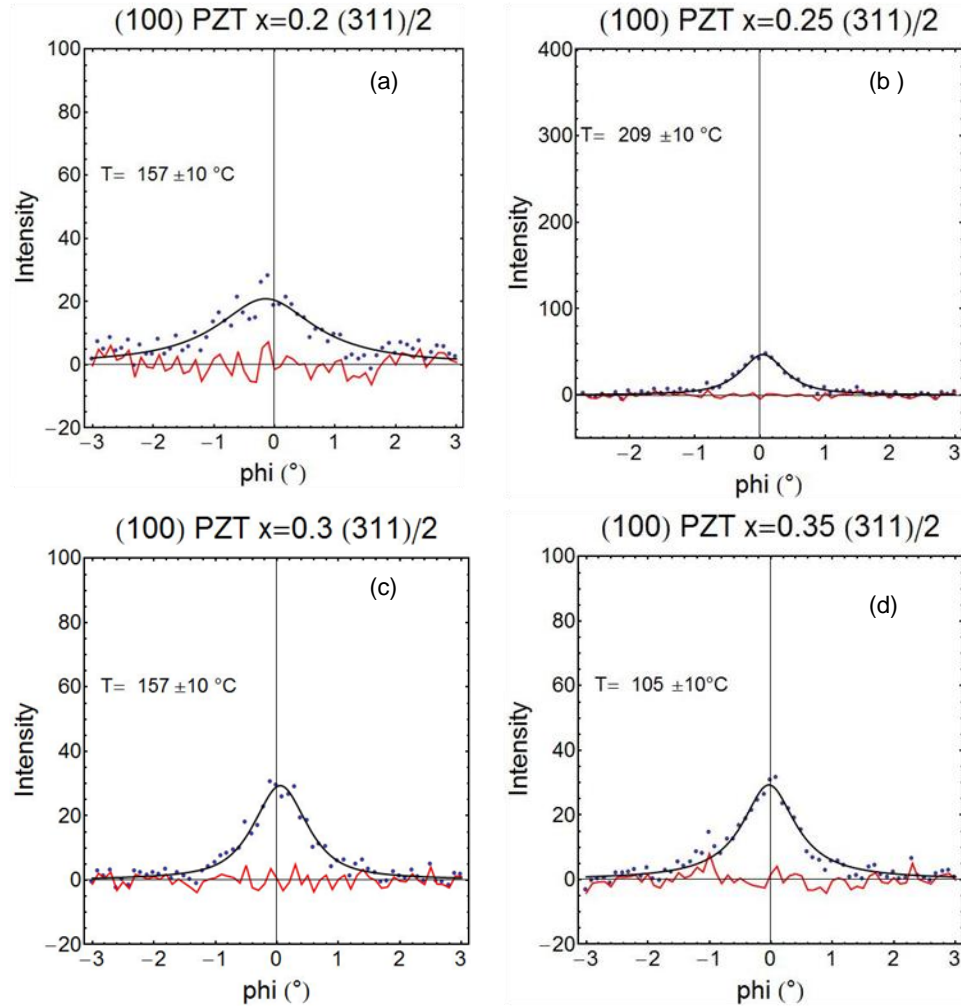
Figure 6.9. X-ray profiles for $\frac{1}{2}\{311\}_{pc}$ peak of strained (a) x = 0.2, (b) x = 0.25, (c) x = 0.3, and (d) x = 0.35 on relaxed x=0.4 on (100) $SrTiO_3$ at temperatures above bulk T_{Tilt}. The points are experimental data; the black line, the two-peak pseudo-Voigt fit; and the red line, a fit to the residuals.

The ϕ scans on the $\frac{1}{2}\{311\}_{pc}$ peak were fitted with pseudo-Voigt peaks so that the FWHM and integrated intensity of the peak could be calculated. ϕ scans rotate the sample about the normal to the diffracting plane (under ideal conditions) and in doing so yield information about the coherent in-plane scattering from the film. Figure 6.9 shows an example of the fits to the experimental data at temperatures above the bulk T_{Tilt} for

each strained PZT composition grown. No clear intensity for the superlattice reflection was observed from the buffer layer for these films. This could be due to a combination of factors, e.g. the intensity arising from the superlattice reflection of the buffer being buried in the signal of the strained layer, or simply the lack of a coherent diffraction region large enough to produce measureable intensity.

Should the FWHM in ϕ match that of the substrate, then the in-plane registry of the film on the substrate is perfect. If the FWHM is larger than that of the substrate then there is some misalignment between the film and the substrate due to dislocations present at the interface. Another method to achieve a large FWHM is through small coherent scattering lengths.[16] For these films, should the width arise solely from the mosaic character of the films, there should be no increase in FWHM with increasing temperature. However, since there is an observable FWHM increase as the temperature is increased in most of the samples, it can be concluded that there is a decrease in the lateral correlation length of octahedral tilting in the films upon heating. Similar to the relaxed films, the T_{Tilt} of the films was identified as the point at which the FWHM of the $\frac{1}{2}\{311\}_{pc}$ peak begins to increase. For the x=0.35 composition, the FWHM of the strained film increases with temperature, suggesting that the T_{Tilt} is at or near room temperature, which is consistent with bulk. From Figure 6.10, the T_{Tilt} observed for the x=0.3 is within error of the observed T_{Tilt} in the bulk. The x=0.25 shows an increase in FWHM at temperatures higher than 150°C, which is only a modest increase in transition temperature as compared with bulk T_{Tilt}. Lastly the x=0.2 film showed no measurable increase in FWHM before signal from the superlattice reflection was lost.
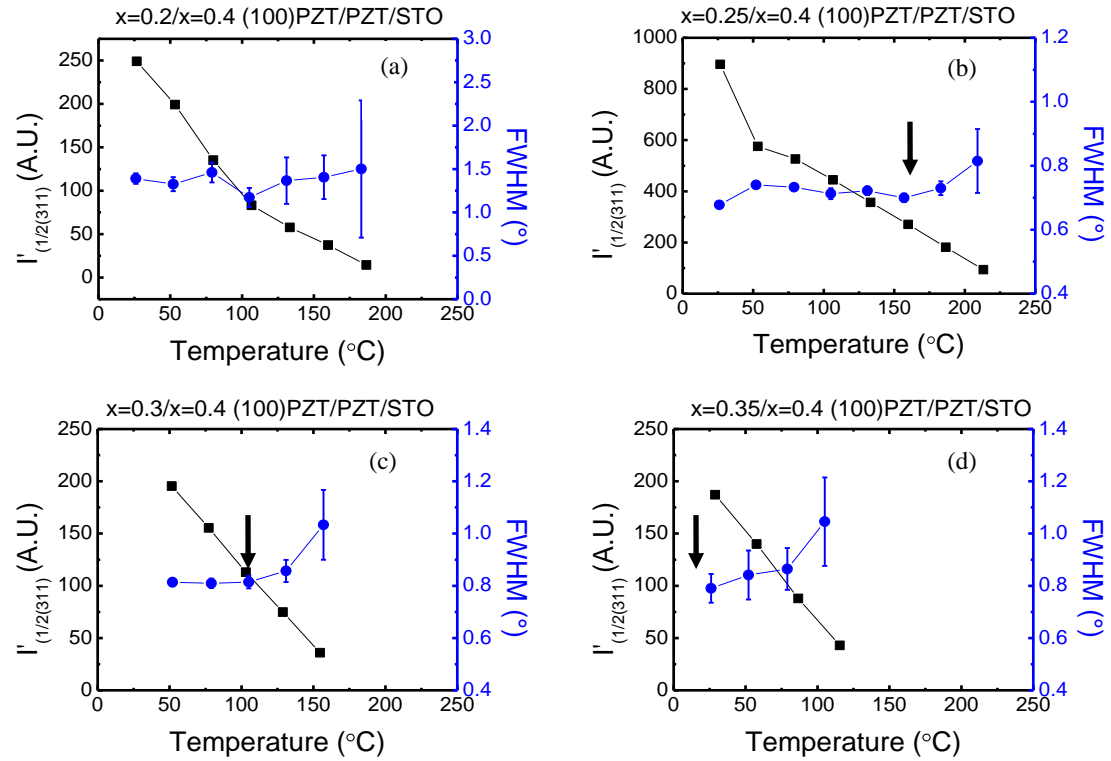
Figure 6.10. Integrated intensity plotted with the full width at half maximum (FWHM) for the $\frac{1}{2}\{311\}_{pc}$ peak for (a) x = 0.2, (b) x = 0.25, (c) x = 0.3, and (d) x = 0.35 on relaxed x = 0.4 on (100) SrTiO$_3$. Finite peak intensity is observed at temperatures above that of bulk T$_{Tilt}$. Arrows mark estimated T$_{Tilt}$

Figure 6.10 shows the integrated intensity of the superlattice peak plotted alongside the FWHM. A finite integrated intensity can be observed for the strained films at temperatures well above those reported in the bulk phase diagram. At high temperatures, there is an observable increase in the FWHM of the $\frac{1}{2}\{311\}_{pc}$ peak. In most cases, there is still finite intensity from the $\frac{1}{2}\{311\}_{pc}$ peak at temperatures above where the FWHM begins to increase. This result is consistent with observations on the relaxed films. The arrows estimating the transition from a long-range tilted phase to one

with non-zero tilting is marked in Figure 6.10 with arrows. As noted, T_{NZT}, the temperature at which octahedral tilting can no longer be detected, is higher than the reported bulk T_{Tilt}. For the films, T_{Tilt} is defined as the point at which the FWHM of the superlattice reflection stabilizes on cooling. There is a weak increase in T_{Tilt} with increasing strain as noted in Table 6.1. To quantify this more precisely measurements should be taken at smaller temperature intervals. The observed strain dependence for this transition is weaker than the strain-dependence of T_C for $Pb(Zr_{1-x}Ti_x)O_3$ thin films.

Table 6.1. Phase transition temperatures for strained $Pb(Zr_{1-x}Ti_x)O_3$ thin films

Error bars are given in the parentheses following each number.

x	ε_m	Phase Transition	Phase Diagram[13]	Strained Films	ΔT (°C)
0.35	-0.42	T_C (°C)	350	421(50)	70(32)
		T_{Tilt} (°C)	37	25(25)	-12(25)
0.30	-0.6	T_C (°C)	333	422(11)	88(11)
		T_{Tilt} (°C)	81	100(25)	19(25)
0.25	-0.71	T_C (°C)	315	431(4)	115(4)
		T_{Tilt} (°C)	113	150(25)	37(25)
0.20	-0.89	T_C (°C)	296	431(12)	134(15)
		T_{Tilt} (°C)	134		

This outcome suggests that the region of non-zero tilt above the bulk T_{tilt} is not significantly changed by the applied biaxial strain. Here, "non-zero-tilt" refers to the existence of either a small domain size in a long-range ordered tilted material, short-range order of the tilt, or a zone of smaller tilt magnitudes. It should also be noted that though the region of non-zero tilt was not strongly influenced by the biaxial strain, the T_C of the films did shift significantly. Thus, it may be possible to use biaxial strains as a means of increasing the stability of ferroelectric phases in low-transition-temperature compounds without simultaneously favoring tilt. This, in turn, could be useful in engineering materials for piezoelectric applications, where high transition temperatures are desirable to expand operating temperature ranges. The ability to independently increase T_C without large accompanying changes in T_{tilt} is useful, because the piezoelectric properties are degraded in tilted materials, potentially as a result of additional domain wall pinning associated with the tilt domain structure.

Using the out-of-plane lattice parameter from Figure 6.8(e), it is possible to calculate the out-of-plane spontaneous strain (x_3) for these films. As expected, the spontaneous strain goes to zero at T_C. When a straight line is plotted to the temperature range of ~200–400°C, there is an observable turn-over. It was difficult to make a proper quadratic fit for the temperature dependence of the spontaneous strain, given the ferroelectric transition in the buffer layer itself. When the spontaneous strain is plotted with the integrated intensity (I') of the ½{311}$_{pc}$ reflection (Figure 6.11(a-d)), it is clear that the turn-over corresponds to the appearance of the superlattice peaks. Therefore, the turn-over in the spontaneous strain is associated with the development of octahedral

tilting. It is unclear at this point if the tilting is due to the short coherence length of the

octahedral tilting, a small domain structure in a long-range-ordered material, or dynamic

short-range ordering.
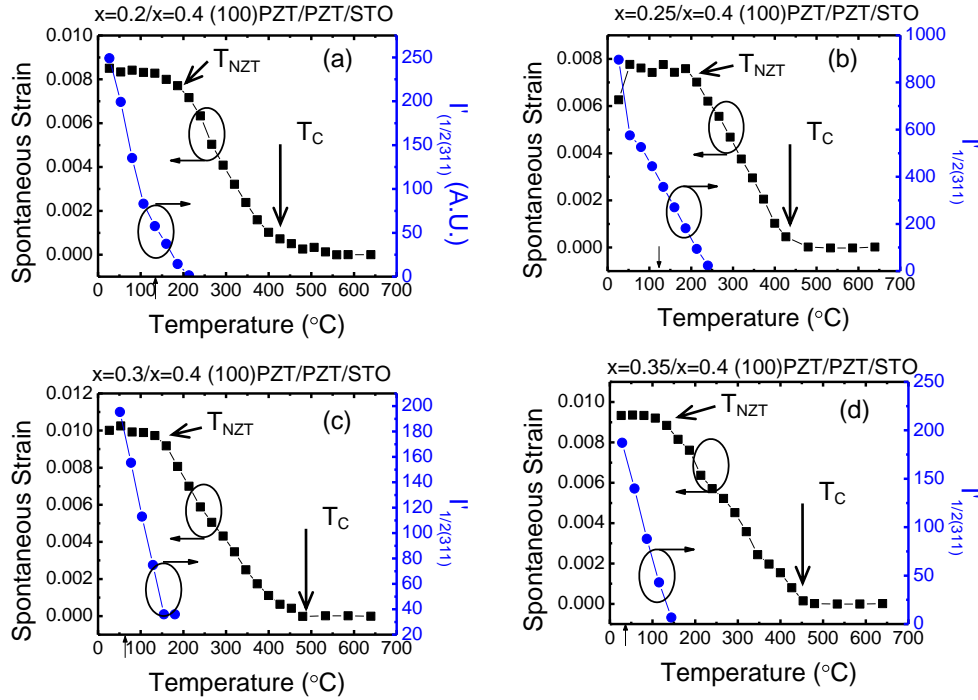
Figure 6.11.   Spontaneous strain and integrated intensity (I′) of the ½(311)$_{pc}$ reflection

for films with (a) x = 0.2, (b) x = 0.25, (c) x = 0.3 and (d) x = 0.35.

Vertical arrows on the x-axis denote bulk tilt transition temperature.

6.2 *(111)$_{pc}$ Oriented Strained Films*

Several theoretical investigations into octahedral tilting have suggested that

differing orientations of epitaxial strain may stabilize different phonon modes responsible

for different tilt stystems.[17,18] In rhombohedral PZT with space group R3c, the tilt can be

characterized as a rotation of the oxygen octahedra around the [111]$_{pc}$ direction. It is

with this in mind that strained [111]$_{pc}$ oriented films were examined to determine if

changing the orientation influenced the tilt of strained rhombohedral PZT films. The mismatch along this orientation is expected to be the same for the buffer layer a ~15 nm film was used. Strained $[111]_{pc}$ oriented films were deposited under the same conditions as $[100]_{pc}$ oriented films yielding ~20-25 nm thick film. The films were taken to the Advanced Photon Source at Argonne National Laboratory to undergo temperature-dependent x-ray diffraction.

The out-of-plane 333_{pc} reflections were studied in order to determine the Curie temperature of the films. The peaks were fitted using a two-peak pseudo-Voigt function, as demonstrated in Figure 6.12(a-c). The out-of-plane spontaneous strain was calculated for these films. The observed strain behavior was found to be similar to that for the *polar* direction of the 111_{pc} relaxed films. This indicates that the compressive strain from the substrate pushes the polarization out of the plane in the coherent films. Similar behavior has been seen for < 150 nm $PbTiO_3$ films on (100) oriented $SrTiO_3$ substrates.[19] The spontaneous strain of the films was calculated from the difference between the measured d-spacing and an extrapolation from the thermal expansion in the paraelectric phase and is plotted in Figure 6.12(d). As with the 100_{pc} strained films, there is an observable increase in T_C for all compositions. Additionally, there is a pronounced turn-over in the spontaneous strain at low temperatures, presumably due to tilt. Similar to the 100_{pc} strained films, it was found that a linear fit to the data in the 200-400°C range yielded the best results. There are a couple differences for the strained films, the first being that only the 111_{pc} direction was observed as compared with a domain state that included non-180° domain walls in the relaxed films. Additionally, these strained films had a ferroelectric

buffer layer which undergoes a ferroelectric phase transition as well and there may be some interaction between the two layers. The small ΔT_C for the x=0.2 composition may come from a partially relaxed film state.
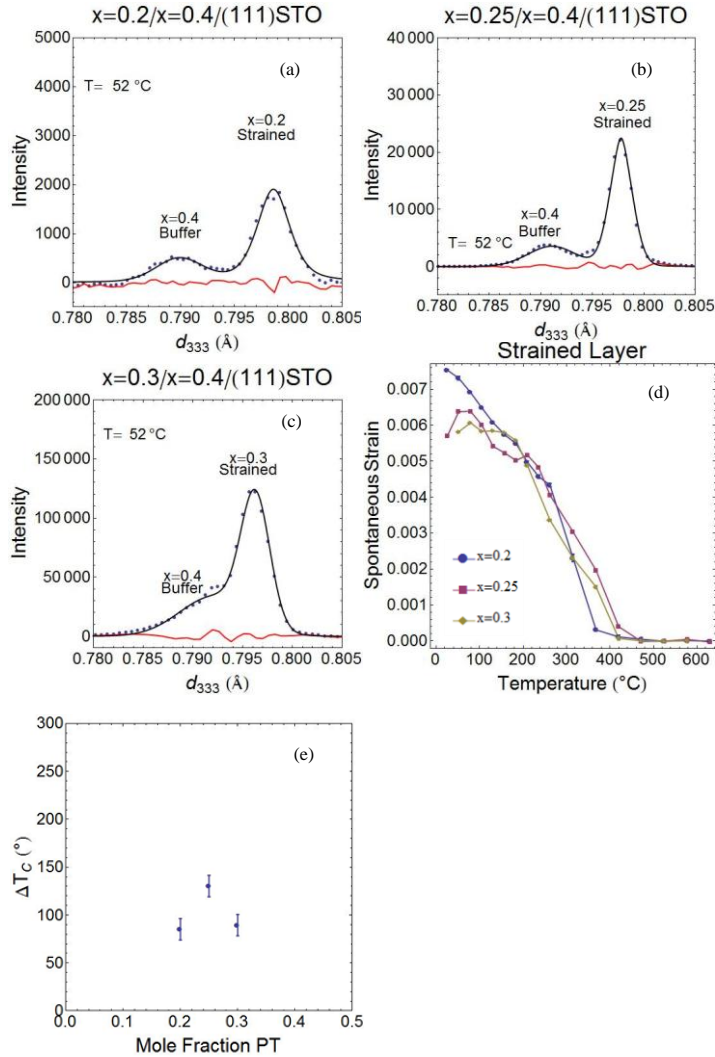
Figure 6.12. X-ray profiles for strained (a) x = 0.2, (b) x = 0.25, and (c) x = 0.3 on relaxed x = 0.4 on (111) SrTiO$_3$; (d) the spontaneous strain for the three compositions; and (e) the extrapolated ΔT_C vs. strain for 111$_{pc}$ samples. In (a-c), the points are experimental data; the black line, the two-peak pseudo-Voigt fit; and the red line, a fit to the residuals.

Figure 6.13 shows the stereographic projections for 111_{pc} oriented PZT films. From the calculated diffraction pattern for PZT, the most intense superlattice reflections are the $\frac{1}{2}\{311\}_{pc}$ type reflections. Figure 6.13(a) shows the location for all $\{311\}_{pc}$ Bragg peaks; they can be seen to occur at three different values in χ (~30°, ~60°, and ~80°). Figure 6.13(b) shows the location of the $\frac{1}{2}\{311\}_{pc}$ peaks when the polar direction is pointed out-of-plane. In this case, superlattice peaks only occur at $\chi \sim 60°$, corresponding to the $\frac{1}{2}\left\{3\bar{1}1\right\}_{pc}$ peak. The fact that the $\frac{1}{2}\{311\}$ peak had intensity for the relaxed films studied in Chapter 5 was a consequence of having a domain state with non-180° domain walls present. Since the strained films should have the polar direction pointed out of plane of the film, the superlattice reflection was sought at $\chi \sim 60°$, as indicated in Figure 6.13(b). As can be seen in Figure 6.13(b), the $\frac{1}{2}\{311\}_{pc}$ reflections for a 111_{pc} oriented film occur only at the $\frac{1}{2}\left\{3\bar{1}1\right\}_{pc}$ - related positions.

(a)   (b)
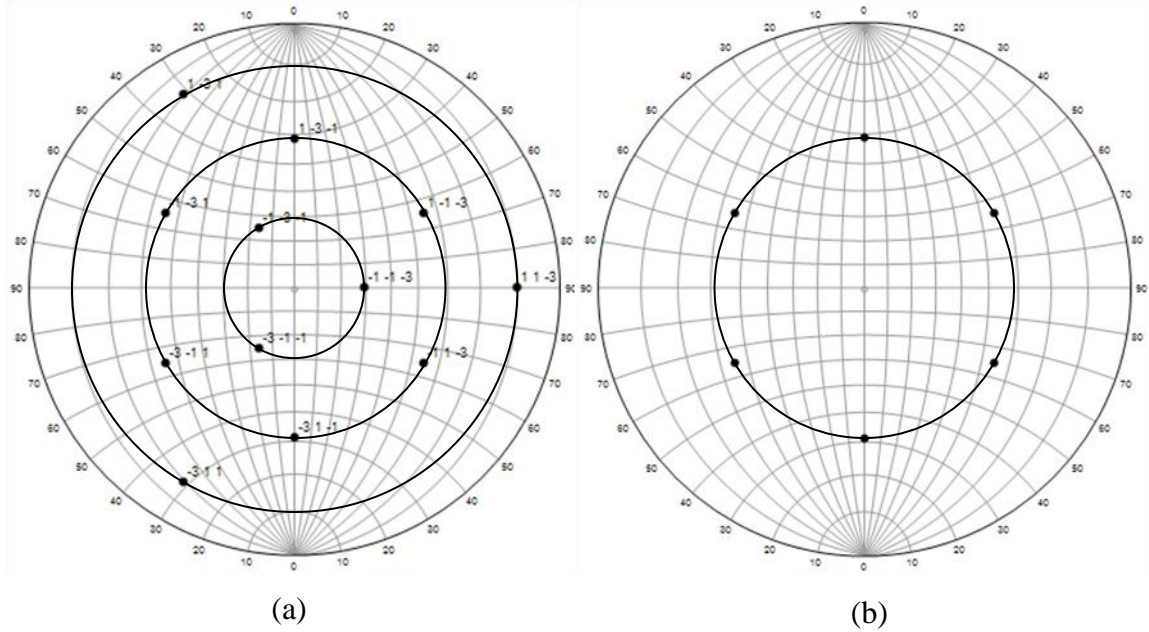
Figure 6.13.   Stereographic projection showing the (a) {311} family Bragg peaks for a

cubic perovskite along the $[111]_{pc}$ direction, showing the locations of the

$\{ooo\}_{pc}$ Bragg peaks, and for (b) rhombohedral $Pb(Zr_{0.8},Ti_{0.2})O_3$ showing

the location of $\frac{1}{2}\{ooo\}_{pc}$ reflections (black dots) when the polar direction

is out-of-plane.

In Figure 6.14(a-c), the superlattice reflection for all three types of $\frac{1}{2}\left\{3\bar{1}1\right\}_{pc}$

reflections is shown for temperatures greater than bulk T_{Tilt}; the data are representative of

all compositions investigated. As evidenced in Figure 6.14(d), peaks were observed only

at the $\frac{1}{2}\left\{3\bar{1}1\right\}_{pc}$ positions which is consistent with only 180° domain walls in the as-grown

strained films, unlike the poly-domain structure observed with the relaxed films.

In addition, the $\frac{1}{2}\{321\}_{pc}$ reflection was investigated to determine if a $\{111\}_{pc}$

oriented PZT constrained films yielded a different tilt system. Figure 6.14(d) shows a ϕ

scan on a $\frac{1}{2}\{321\}_{pc}$ reflection; the lack of any observable intensity signifies the lack of

in-phase tilting within the strained film. Likewise, diffraction patters were collected at variations of the ½{311}$_{pc}$ and ½{321}$_{pc}$ reflections to determine if tilt occurred along an individual axis, however the only tilting present was consistent with the a⁻a⁻a⁻ tilt system.
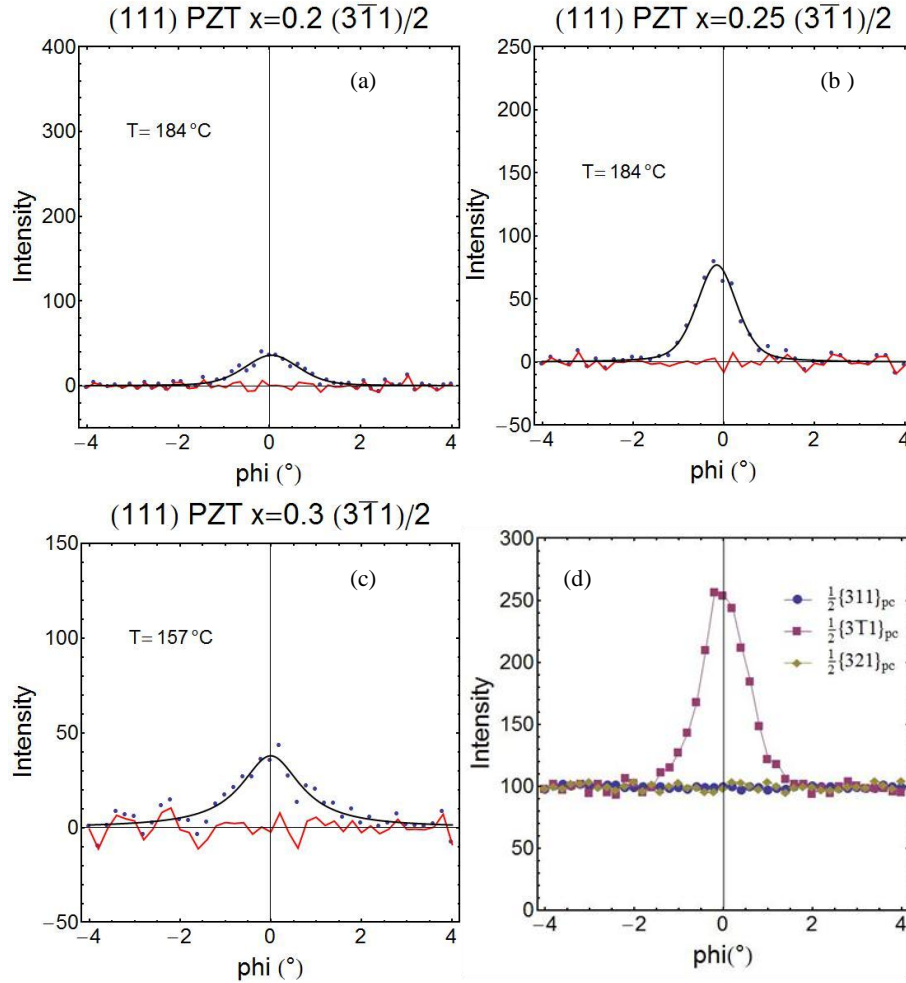
Figure 6.14. X-ray profiles for ½$\left\{3\bar{1}1\right\}_{pc}$ peak of strained (a) x = 0.2, (b) x = 0.25, and

(c) x = 0.3, on relaxed x = 0.4 on (100) SrTiO₃; and (d) x-ray diffraction

pattern from a superlattice peak at the ½{311} and ½$\left\{3\bar{1}1\right\}_{pc}$. The points

are experimental data; the black line, the two-peak pseudo-Voigt fit; and

the red line, a fit to the residuals.

As was observed with all the PZT films studied in this thesis, finite intensity was detected for the tilt-related superlattice lines at temperatures above those shown for the bulk tilt transition. As was done elsewhere in the thesis, the peaks were fitted using a pseudo-Voigt function and the integrated intensities and FWHM of the peaks were calculated. This is shown in Figure 6.15, where the integrated intensity of the superlattice peak is plotted alongside the FWHM. There is a finite integrated intensity observed for the strained films at temperatures above the bulk T_{Tilt}. This corresponds to a trend in the FWHM to increase as the temperature increases. Unfortunately, the large error at near the temperatures at which the peak disappears makes it difficult to determine an exact T_{Tilt} for these materials. The trend in FWHM to increase suggests that there is some non-zero tilting present.
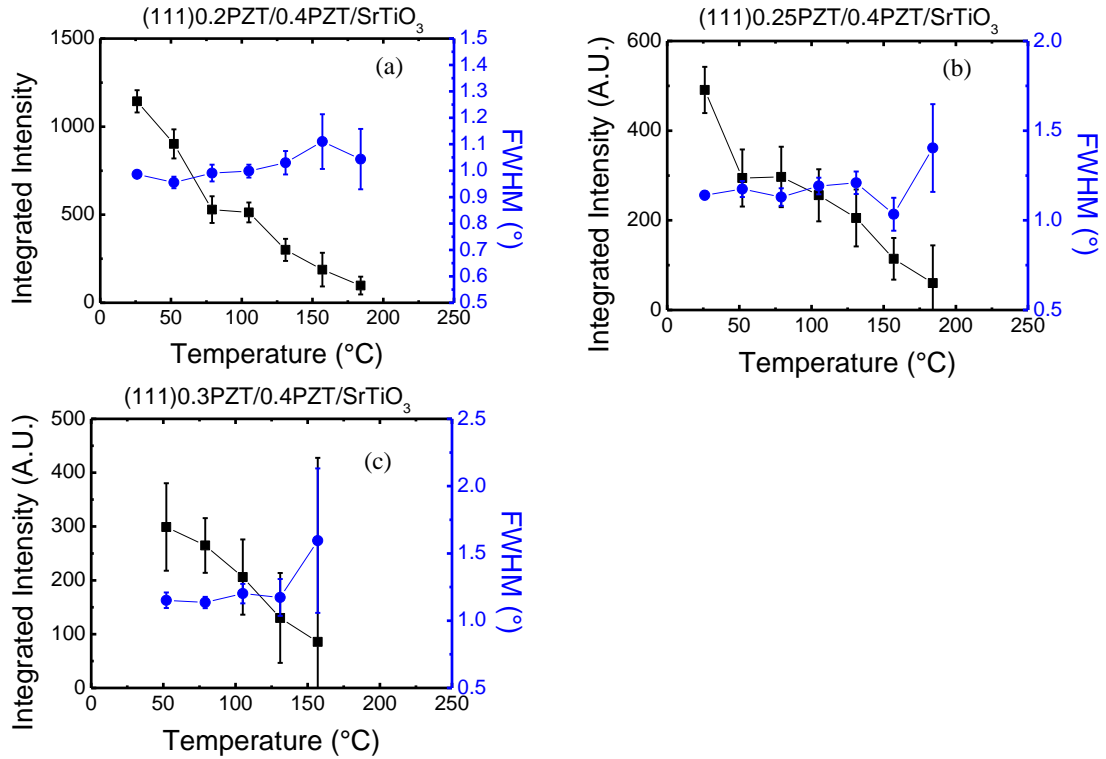
Figure 6.15. Integrated intensity plotted with the full width at half maximum (FWHM) for the $\frac{1}{2}\left\{3\bar{1}\bar{1}\right\}_{pc}$ peak for (a) x = 0.2, (b) x = 0.25, and (c) x = 0.3, on relaxed x = 0.4 on (111) SrTiO$_3$. Finite peak intensity was observed at temperatures above that of bulk T_{Tilt}.

Using the out-of-plane d-spacing from Figure 6.12(e), it is possible to calculate the out-of-plane spontaneous strain (*x*) for these films. As expected, the spontaneous strain goes to zero at T_C. There is an observable turn-over in the spontaneous strain at temperatures higher than the reported T_{Tilt}. The turn-over in the spontaneous strain is correlated with the development of non-zero octahedral tilting. This demonstrates that the appearance of non-zero rotation is not strongly strain- or orientation-dependent for Pb(Zr$_{1-x}$Ti$_x$)O$_3$ thin films.
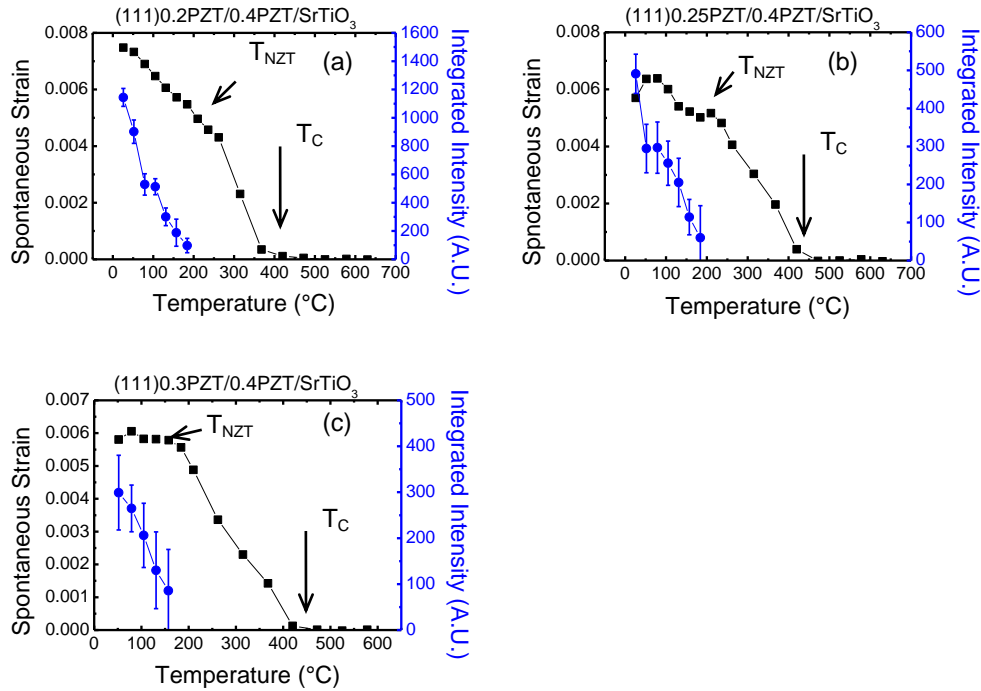
Figure 6.16. Spontaneous strain and integrated intensity (I′) of the ½(311) reflection for films with (a) x = 0.2, (b) x = 0.25, and (c) x = 0.3, on relaxed x = 0.4 on (111) SrTiO₃.

One purpose of this thesis was to determine if strain has an effect on the tilt transition temperature. In Figure 6.17, the FWHM of the half-order peak is plotted for strained films of $(100)_{pc}$ and $(111)_{pc}$ orientations and compared to that of relaxed films. The peaks show similar FWHM trends for relaxed and strained films. Additionally, the increase in FWHM indicative of a decrease in the coherent scattering volume occurs at similar temperatures for each sample. Finally, the temperature at which the superlattice peak disappears is similar for each orientation as well. This indicates that there is little to no orientation dependence of strain on the observable non-zero tilt within PZT films.
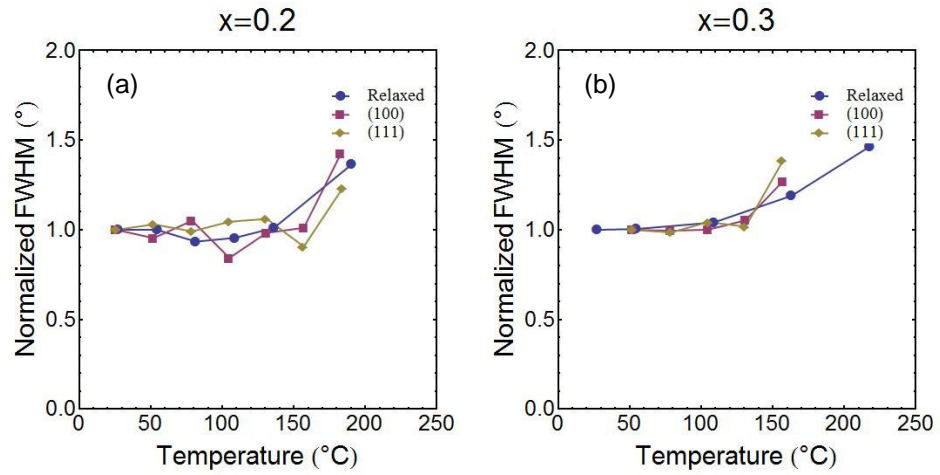
Figure 6.17. Normalized FWHM of 100_{pc} and 111_{pc} strained bi-layer films with compositions of (a) x = 0.2, and (b) x = 0.3 compared to data for 111_{pc} relaxed films of the same composition.

6.3 *References:*

[1]Y. M. Chiang, D. Birnie, and W. D. Kingery, "Physical Ceramics,*"* pp. 522 1st ed. John Wiley & Sons, Inc: New York, New York, (1997).

[2]M. Putero-Vuaroqueaux, N. Burle, and B. Pichaud, "Metastability in the Matthews-Blakeslee mechanism for semiconductor film relaxation," *Philosophical Magazine Letters,* **81**[8] 519-25 (2001).

[3]R. J. Zeches, M. D. Rossell, J. X. Zhang, A. J. Hatt, Q. He, C. H. Yang, A. Kumar, C. H. Wang, A. Melville, C. Adamo, G. Sheng, Y. H. Chu, J. F. Ihlefeld, R. Erni, C. Ederer, V. Gopalan, L. Q. Chen, D. G. Schlom, N. A. Spaldin, L. W. Martin, and R. Ramesh, "A Strain-Driven Morphotropic Phase Boundary in $BiFeO_3$," *Science,* **326**[5955] 977-80 (2009).

[4]Powder Diffraction File, International Centre for Diffraction Data, (2009)

[5]M. Biegalski, "Epitaxially Strained Strontium Titanate" pp.209, Ph.D. thesis in Materials Science and Engineering, The Pennsylvania State University, (2006)

[6]J. R. Downes, D. J. Dunstan, and D. A. Faux, "Analysis of the shortcomings of the Matthews-Blakeslee theory of critical thickness at higher strains," *Philosophical Magazine Letters,* **76**[2] 77-81 (1997).

[7]N. Doukhan and J. C. Doukhan, "Dislocations in Perovskites $BaTiO_3$ and $CaTiO_3$," *Physics and Chemistry of Minerals,* **13**[6] 403-10 (1986).

[8]T. Ueno, T. Irisawa, Y. Shiraki, A. Uedono, S. Tanigawa, R. Suzuki, T. Ohdaira, and T. Mikado, "Characterization of low temperature grown Si layer for SiGe pseudo-

substrates by positron annihilation spectroscopy," *Journal of Crystal Growth,* **227** 761-65 (2001).

[9]A. G. Cullis, "The morphology and misfit dislocation formation characteristics of strained heteroepitaxial layers - ex-situ and in-situ growth-studies," *Scanning Microscopy,* **8**[4] 957-67 (1994).

[10]R. People and J. C. Bean, "Calculation of Critical Layer Thickness Versus Lattice Mismatch for Ge_xSi_{1-x}/Si Strained-Layer Heterostructures," *Applied Physics Letters,* **47**[3] 322-24 (1985).

[11]J. P. Maria, S. Trolier-McKinstry, D. G. Schlom, M. E. Hawley, and G. W. Brown, "The influence of energetic bombardment on the structure and properties of epitaxial $SrRuO_3$ thin films grown by pulsed laser deposition," *Journal of Applied Physics,* **83**[8] 4373-79 (1998).

[12]D. G. Schlom, L. Q. Chen, C. B. Eom, K. M. Rabe, S. K. Streiffer, and J. M. Triscone, "Strain tuning of ferroelectric thin films," *Annual Review of Materials Research,* **37** 589-626 (2007).

[13]M. J. Haun, "Thermodynamic theory of the lead zirconate-titante solid solution system" pp.158, Ph.D. thesis in Solid State Science, The Pennsylvania State University, (1988)

[14]N. A. Pertsev, V. G. Kukhar, H. Kohlstedt, and R. Waser, "Phase diagrams and physical properties of single-domain epitaxial Pb(Zr1-xTix)O-3 thin films," *Physical Review B,* **67**[5] - (2003).

[15]S. Choudhury, Y. L. Li, and L. Q. Chen, "A phase diagram for epitaxial PbZr1-xTixO3 thin films at the bulk morphotropic boundary composition," *Journal of the American Ceramic Society,* **88**[6] 1669-72 (2005).

[16]B. E. Warren, "X-ray Diffraction,*"* pp. 381. Dover Publications Inc.: Mineola, NY, (1990).

[17]A. T. Zayak, X. Huang, J. B. Neaton, and K. M. Rabe, "Structural, electronic, and magnetic properties of $SrRuO_3$ under epitaxial strain," *Physical Review B,* **74**[9] 094104 (2006).

[18]K. M. Rabe, "Theoretical investigations of epitaxial strain effects in ferroelectric oxide thin films and superlattices," *Current Opinion in Solid State & Materials Science,* **9**[3] 122-27 (2006).

[19]C. D. Theis, "Investigation of growth and domain structure of epitaxial lead titanate thin films" pp.114, M.S. thesis in Materials Science and Engineering, The Pennsylvania State University, (1996)

Chapter 7   Conclusions and Future Work

Relaxed epitaxial $\{100\}_{pc}$ and $\{111\}_{pc}$ oriented films of $Pb(Zr_{1-x}Ti_x)O_3$ on $SrRuO_3/SrTiO_3$ substrates were grown by pulsed laser deposition for x values from 0.2 to 0.4. For all compositions, films with thicknesses >350 nm had room temperature permittivities between 400 and 500 which rose to >3000 at the Curie temperature; the loss tangents were < 5% at 10 kHz over this temperature range. The films exhibited bulk Curie temperatures (T_C) and Curie-Weiss constants within experimental error. Synchrotron x-ray diffraction was used to investigate both the spontaneous strain and the superlattice reflections arising from octahedral tilting. It was found that the tilt transition temperatures for the relaxed films correspond with the bulk phase diagram. From the spontaneous strain, a phase transition was found to exist at temperatures corresponding to the bulk T_{Tilt}. However, finite intensity above the reported bulk tilt transition was found to exist which appears to correlate to an extended region of non-zero octahedral tilt. This region of non-zero tilt was found to correspond to anomalies in the dielectric permittivity and switchable polarization. This suggests that in rhombohedral PZT the tilt transition is not a simple turning on of the tilt, rather it goes through an extended region of non-zero tilt which affects the electrical properties. The phase diagram for $Pb(Zr_{1-x}Ti_x)O_3$ is redrawn as a result to include a region of non-zero tilt.

100_{pc} and 111_{pc} strained films were also grown by pulsed laser deposition using a 0.4PZT layer for lattice matching. For 100_{pc} films a linear dependence of T_C on the in-plane compressive strain was found. Calculating the T_{Tilt} from the FWHM of the superlattice reflection shows that a weak increase in the T_{Tilt} with increasing strain. The

strained films showed the same type of non-zero-tilting above the bulk tilt transition as the relaxed films. 111_{pc} oriented strained films also exhibited a T_C shift upon the application of strain. The large error on the fits of the ½{ooo} reflections on the 111_{pc} oriented samples prevents any conclusions about the change in T_{Tilt} for these films. The larger strain dependence for the ferroelectric transition temperature, relative to the tilt transition temperature, suggests that it may be possible to use strain to stabilize ferroelectric phases without greatly increasing the temperature at which octahedral tilting or non-zero tilt is observed. Through studying the strained films on multiple orientations it was found that only anti-phase tilting was observed and therefore strain does not greatly affect the tilt system of the $Pb(Zr_{1-x}Ti_x)O_3$ thin films.

7.1 *Future Work*

7.1.1 Origins of Non-Zero Octahedral Tilting

This purpose of this thesis was to study octahedral tilting in thin films and to discover if there was a way to control the tilt transition temperature. Films were deposited with nominally tilted and untilted phases. The films produced in this study, despite their high electrical quality, exhibited behavior which was not commonly found in bulk.[1,2] However, while these studies showed dielectric evidence for non-zero tilt at temperatures similar to those seen in this thesis, the polarization behavior are widely different between these films and the bulk materials studied. Additionally, studies done on piezoelectric non-linearity in bulk rhombohedral PZT exhibited phase transition temperatures nearly identical to that of the reported phase diagram and showed no

133

evidence of non-zero tilting.[3,4]   These discrepancies between these various studies suggest that octahedral tilting still needs to be understood.

The first question that arises is 'is the non-zero tilt observed in epitaxial thin films fundamental to the behavior of PZT, or is it something that is inherent to thin films deposited under the conditions used in this thesis'. To address this question, it would be pertinent to perform experiments on both bulk and thin film samples prepared by other methods. Temperature dependent diffraction should be performed on carefully processed bulk PZT powders and ceramics to determine if the non-zero tilt region exists at temperatures higher than reported in previous studies on the bulk phase diagram. If the experiments do not show a region of non-zero tilt, it would be important to understand why it exists in thin films. Thin film deposition processes have been shown to create large number of defects in the resulting films. If the non-zero tilt region existed solely due to defects, this relationship would need to be studied. A possible experiment would be to introduce the defects into the bulk to study how each defect may affect octahedral tilting.

Additionally, inelastic scattering such as Raman scattering or inelastic x-ray or neutron diffraction[5,6] would give information on the nature of the phonon mode responsible for octahedral tilting. Once, the origin of the non-zero tilt is understood, it will be necessary to determine how to manipulate tilt in such a way so that no tilt phases exist at compositions of interest.

A second set of experiments should be performed to determine the nature of the non-zero tilt regions. This thesis pointed to the existence of a region of non-zero tilt, but

134

leaves open the question of whether the non-zero tilt was from short-range order, long-range order with small domain size, or simply small but finite tilting. Diffraction studies recording numerous peaks would allow for calculation of the magnitude of the tilt for the films. Additionally, through the refinement of the diffraction data, it would be possible to calculate the distortion of the oxygen octahedra. Studying the behavior of tilting as a function of electric field would also be beneficial. Figure 7.1 shows the strain in the d-spacing of the 002_{pc} reflection as a function of applied voltage for a thick 100_{pc} oriented relaxed film with a composition of x-= 0.4. As can be seen, as the voltage is increased, there is a linear relationship between strain and voltage. Studying the coupling between field dependent diffraction will show how the octahedral distorts and rotates as a function of electric field.
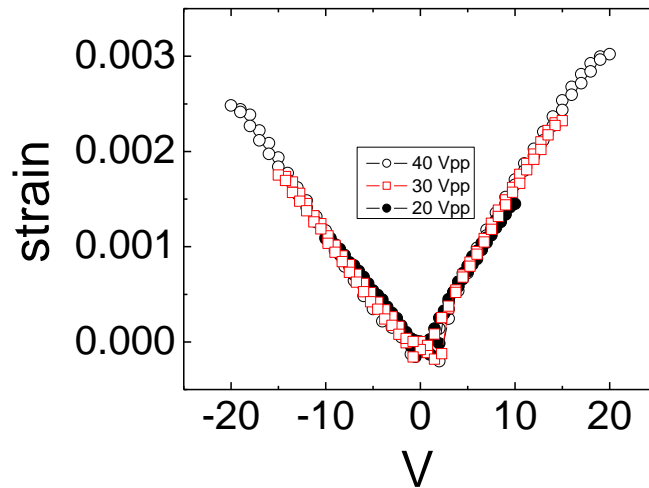
Figure 7.1.   Strain as a function of applied voltage for a ~400 nm thick Pb(Zr$_{0.6}$,Ti$_{0.4}$)O$_3$ thin film as measured by x-ray diffraction

Finally, it was shown in this thesis that the non-zero tilt region influences the electrical properties. This can be detrimental to any resulting devices performance. Studying the coupling between the non-zero tilt region and the polarization may help design better devices so that the deleterious effects of tilt can be avoided or at the very least minimized in the future. Expanding beyond the PZT system is also crucial to determine if this exists solely for PZT, or if it translates to other systems.

7.2 *References:*

[1]X. H. Dai, Z. K. Xu, and D. Viehland, "Effect of oxygen octahedron rotations on the phase-stability, transformational characteristics, and polarization behavior in the lead-zirconate-titanate crystalline solution series," *Journal of the American Ceramic Society,* **78**[10] 2815-27 (1995).

[2]X. H. Dai, Z. Xu, J. F. Li, and D. Viehland, "Constriction of the Polarization by Incoherent Oxygen Octahedral Tilting in Rhombohedral-Structured Lead-Zirconate-Titanate," *Journal of Applied Physics,* **77**[7] 3354-60 (1995).

[3]R. Eitel and C. A. Randall, "Octahedral tilt-suppression of ferroelectric domain wall dynamics and the associated piezoelectric activity in Pb(Zr,Ti)O$_3$," *Physical Review B,* **75**[9] (2007).

[4]M. J. Haun, "Thermodynamic theory of the lead zirconate-titante solid solution system" pp.158, Ph.D. thesis in Solid State Science, The Pennsylvania State University, (1988)

[5]G. Fraysse, J. Haines, V. Bornand, J. Rouquette, M. Pintard, P. Papet, and S. Hull, "Low-symmetry phases at the tilt boundary of the Pb(Zr$_{1-x}$Ti$_x$)O$_3$ solid solution," *Physical Review B,* **77**[6] 064109 (2008).

[6]J. D. Axe, G. Shirane, and K. A. Mueller, "Zone-boundary phonon instability in cubic LaAlO$_3$," *Bulletin of the American Physical Society,* **14**[1] 61-68 (1969).

Appendix:

X-ray Diffraction Measurements on SrRuO$_3$ Films

SrRuO$_3$ (SRO) films were grown on various substrates under standard conditions. The deposition time was varied in order to change the film thickness over the range from ~10 nm to 200 nm. As the film thickness increased, the color of the film changed from translucent to a deep purplish color at the 80-100 nm thickness range.

The lattice mismatch between SRO and LaAlO$_3$ is ~4% and therefore it is expected that the samples will relax within a few nanometers. Samples grown on (100)$_{pc}$ LaAlO$_3$ (LAO), such as those on which the TEM analysis was conducted, were measured using four circle x-ray diffraction. Examples of the x-ray patterns are given in Figure A.1 - no second phase is present within the films for all thicknesses studied.. The peaks were fitted using the pseudo-Voigt function and the d-spacings were calculated using Bragg's law.
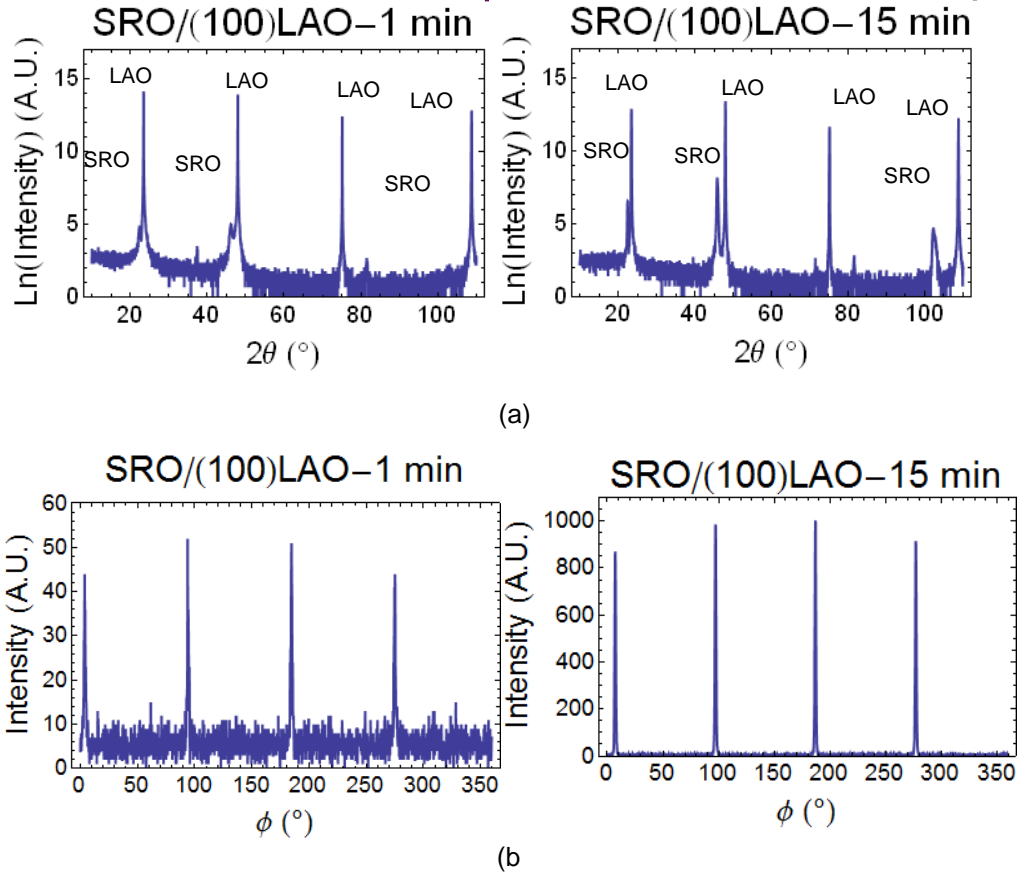
Figure A.1. (a) X-ray diffraction patterns for two SRO/(100)$_{pc}$LAO samples exhibiting epitaxial growth; and (b) corresponding φ scans on the 101pc peak on the samples confirming epitaxy.

The d-spacing for the 001, 002, 003 (if present) and the 004 reflections for the films were measured and the out-of-plane lattice parameters for the films were calculated using the Nelson-Riley analysis. These are plotted in Figure A.2(a). The ~10 nm and ~25 nm films showed a lattice parameter of 3.92 ± 0.005 Å. This is smaller than reported from bulk and may be associated with the observed Ru-deficiency. The lattice parameters then decreased for samples below ~150 nm thick, which would be consistent with fully relaxed Ru-deficient films. The ~150 nm thick film however had a larger

lattice parameter. It has been shown before that increased ionic bombardment during deposition may increase the lattice parameters for the films and may be the case for the inflation of the lattice parameters here.[1]

In order to calculate the in-plane lattice parameter, scans along the 101_{pc} family of peaks was performed. It was difficult to resolve the 303 film peak due to low intensity, which resulted in larger uncertainty in the Nelson-Riley fitting of $d_{101,pc}$. From $d_{101,pc}$ and the out-of-plane lattice parameter, the in-plane lattice constant was calculated. If the SRO films were constrained to the substrate, one would expect their lattice parameters to be matched to the LAO lattice parameter. The ~ 25 nm thick sample has an in-plane lattice parameter of ~3.85 ± .01 Å, which is intermediate between the bulk value and that of 3.79Å of the LAO substrate. This is consistent with a partially relaxed film. The 1 minute sample however has an apparent lattice parameter larger than that in the out-of-plane direction. Should the film be compressively strained, the 2θ scan on the 101 reflection might not record the strained film reflection due to it being at a different χ angle, however, with low resolution on the χ circle, it is possible to record some intensity. Using this value along with the lattice parameter for the out-of-plane direction may lead to the artificially large in-plane lattice parameter.
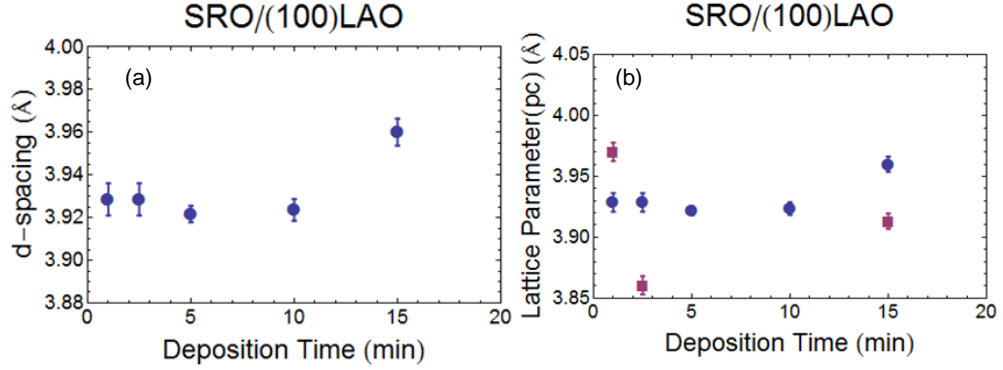
Figure A.2. (a) d-spacing for the 001_{pc} reflection calculate from a Nelson-Riley Fit and (b) lattice parameters for SRO/(100)LAO thin films. Circles are out of plane lattice parameters and squares represent in plane lattice parameters.

X-ray rocking curves were taken of the 002 SRO reflections. The x-ray rocking curves for 10, 25 and 150 nm films are shown in Figure A.3. For the 15 minute deposition, the resulting ~150 nm thick film is expected to be fully relaxed. The rocking curve for the 10 nm thick film grown for 1 minute shows a sharp intense peak corresponding to the strained material that is surrounded by more diffuse shoulders due to the relaxed part of the film. As the deposition thickness is increased, the diffuse shoulder begins to dominate the rocking curve. This would indicate that the film is more fully relaxed. Figure A.3 shows the rocking curve taken at two values in ϕ for a ~150 nm thick sample deposited for 15 minutes. Rather than a single peak, the rocking curve shows multiple peaks. These peaks are separated by ~ 0.4° tilt, which is consistent with orthorhombic tilt of the SRO layer on a substrate.[2] The ϕ scan taken at 0° shows three peaks, indicating that the domain structure for this sample is such that it has the c-axis pointed both in and out of the plane of the film.
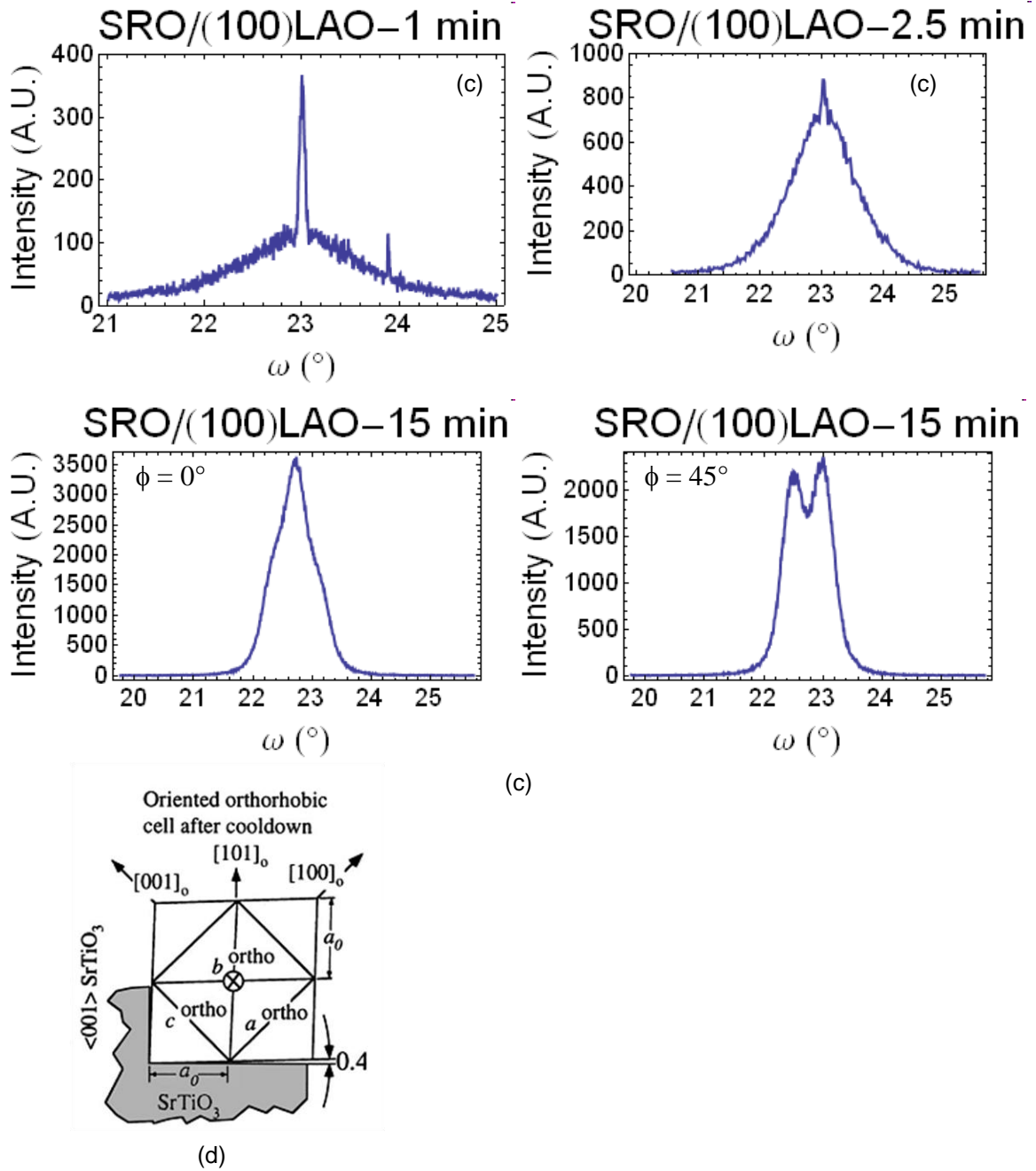
Figure A.3. X-ray rocking curves of SRO/(100)LAO thin films at (a) ~10 nm, (b) ~25 nm; (c) two separate directions in f for a ~150 nm sample and a schematic showing the origin of the tilt seen in part (c).[2]

X-ray Diffraction Measurements on Pb(Zr_{1-x}Ti_x)O₃ Films

Relaxed films were taken to the Advanced Photon Source at Argonne National Laboratory to perform high temperature synchrotron diffraction. The films were heated above T_C and measured upon cooling. Relaxed films were deposited on 111 oriented $SrRuO_3/SrTiO_3$ and the out of plane x-ray diffraction was measured. The sample was heated and the scans θ–2θ scans around the 444_{pc} reflection were performed. The raw results are presented in Figure A.4.
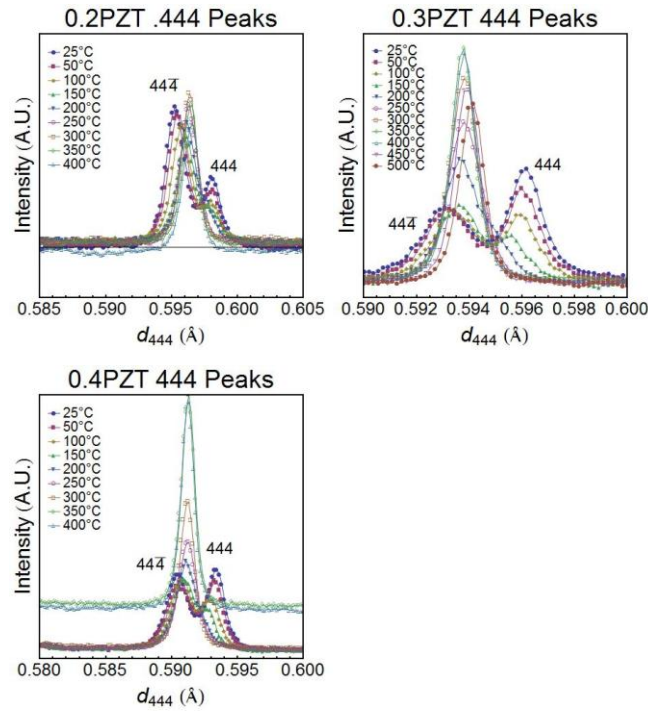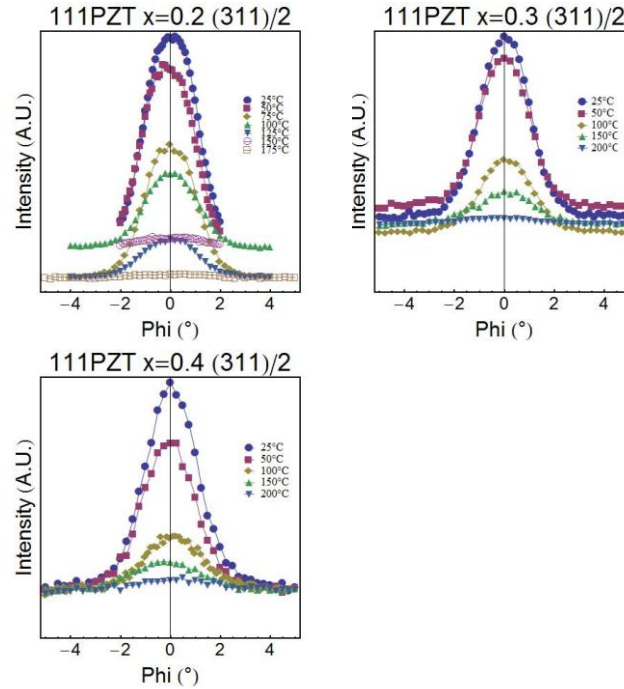

Figure A.4. d-spacing for the 444_{pc} peak at various temperatures for relaxed 111_{pc} oriented films with a composition of (a) x=0.2, (b) x=0.3, (c) x=0.4

As the temperature was cooled, ϕ scans were performed at $\frac{1}{2}\{311\}_{pc}$ position for PZT. At the first indication of the superlattice reflection, scans were performed on the 2θ, χ and ϕ axis to center on the peak location. In doing so, the peak position was

identified and one final φ scan was performed to record the intensity for fitting the peak. The collected scans are shown in Figure A.5.

Figure A.5. φ scans on the ½{311}pc reflection at various temperatures for relaxed 111$_{pc}$ oriented films with a composition of (a) x=0.2, (b) x=0.3, (c) x=0.4

For the 100$_{pc}$ strained films the sample was heated to 600°C assuming that this would be above the Curie temperature and in the paraelectric cubic state. Scans were then performed on the 006$_{pc}$ peak and the d-spacings were recorded. The 006$_{pc}$ peak was used so that to make fitting to the 006$_{pc}$ reflection of the strained film and the buffer layer possible. The collected scans are shown in Figure A.6. Similar treatments were done for the 111$_{pc}$ oriented films and are shown in Figure A.6. For the 111$_{pc}$ oriented strained films, when the intensity from the 333$_{pc}$ reflection from the buffer layer was insufficient for fitting, scans from the 222$_{pc}$ reflection were used.
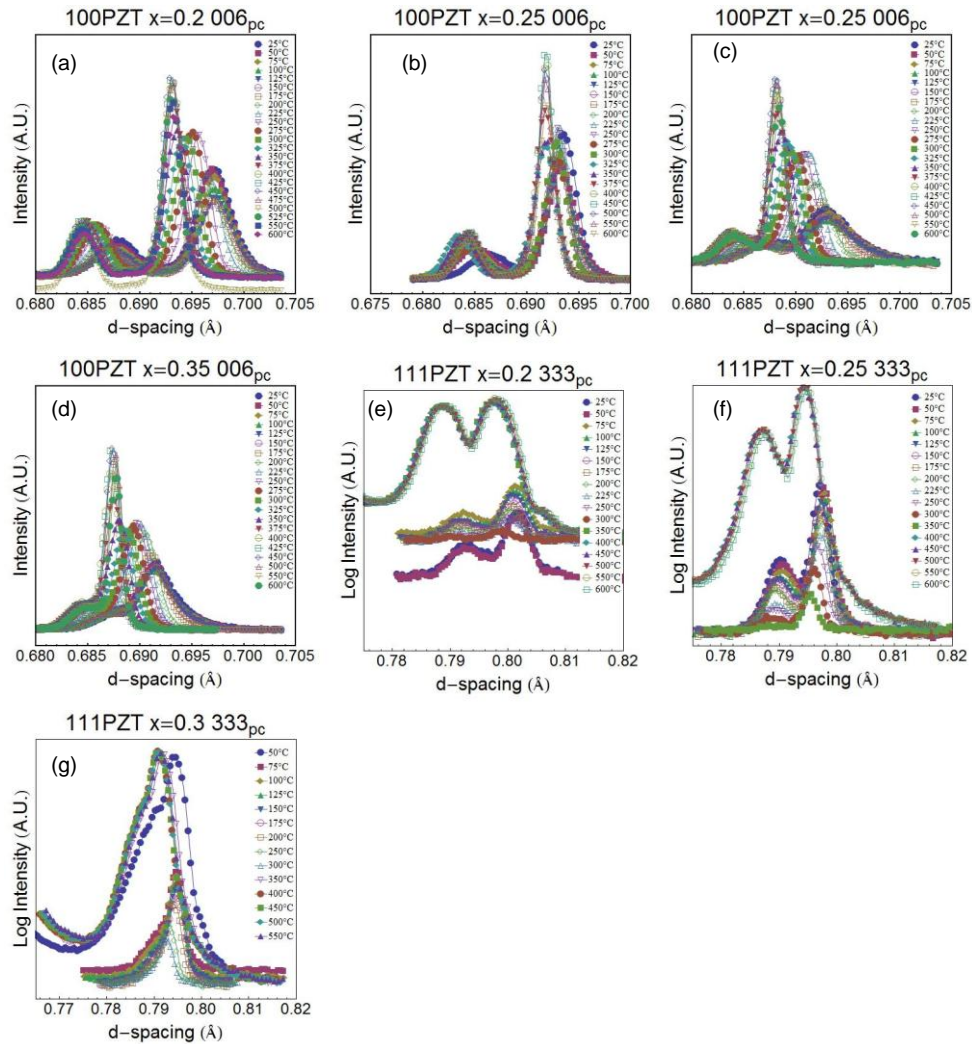
Figure A.6. d-spacing as a function of temperature for $\{001\}_{pc}$ oriented films with compositions of (a) x=0.2 (b) x=0.25 (c) x=0.3 and (d) x=0.35 ; and $\{111\}_{pc}$ oriented films scans with compositions of (e) x=0.2 (f) x=0.25 (g) x=0.3.

The superlattice reflections for strained films were monitored as a function of temperature. Similar procedure was performed on the films where an initial scan was performed to determine if there was intensity present, and then subsequent scans were

performed to locate the center of the reflection. The collected scans for the $\{100\}_{pc}$ and the $\{111\}_{pc}$ strained films are shown in Figure A.7.
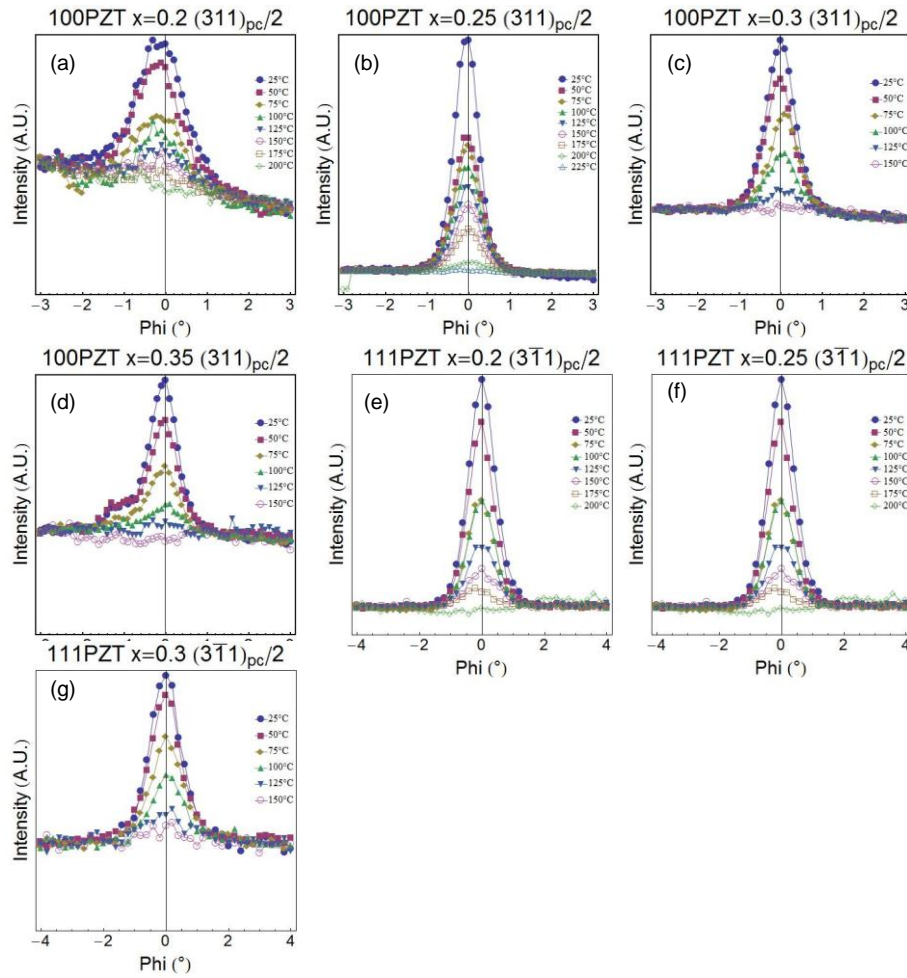
Figure A.7. ϕ scans on the $\frac{1}{2}\{311\}_{pc}$ reflection at various temperatures for strained $\{001\}_{pc}$ oriented films with a composition of (a) x=0.2, (b) x=0.25, (c) x=0.3 (d) x=0.35 and strained $\{111\}_{pc}$ oriented films with composition of (e) x=0.2, (f) x=0.25, (g) x=0.3.

During the initial alignment of the films at room temperature, several superlattice positions were investigated to determine if there was any superlattice intensity. Doing so can yield information about the domain structure and the tilt system of the films. For

111_{pc} oriented films, the superlattice reflections investigated are shown in Figure A.8 for a representative sample. As can be seen, only significant superlattice intensity occurs at the $\frac{1}{2}3\bar{1}1$ peak location. This indicates that only anti-phase tilting is present within strained films.
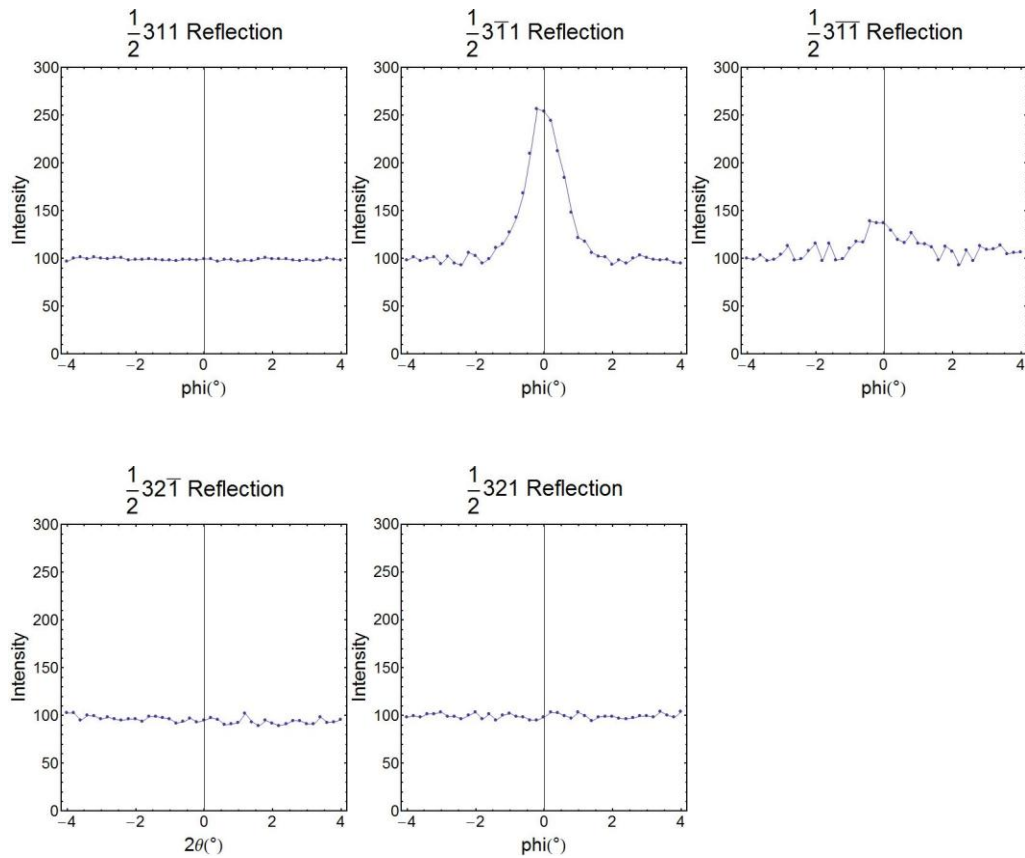
Figure A.8. ϕ scans on the various superlattice reflections for a $Pb(Zr_{1-x}Ti_x)O_3$ strained film with a composition of x = 0.2.

References:

[1] J. P. Maria, S. Trolier-McKinstry, D. G. Schlom, M. E. Hawley, and G. W. Brown, "The influence of energetic bombardment on the structure and properties of epitaxial $SrRuO_3$ thin films grown by pulsed laser deposition," *Journal of Applied Physics,* **83**[8] 4373-79 (1998).

[2] J. P. Maria, H. L. McKinstry, and S. Trolier-McKinstry, "Origin of preferential orthorhombic twinning in $SrRuO_3$ epitaxial thin firms," *Applied Physics Letters,* **76**[23] 3382-84 (2000).

VITA

Daniel Scott Tinberg was born on July 6, 1981 in Elkhorn, WI to Theoder and Janice Tinberg. Daniel graduated from Delavan-Darien High School in 1999 where he was a student athlete and member of the academic decathalon team. Earning the George W. Borg Science Scholarship, he attended the University of Wisconsin-Madison, studying Materials Science and Engineering. After his junior year, he obtained a student research position in Dr. Reid F. Cooper's research group where his responsibilities included furnace maintenance, designing experimental apparatus, aiding graduate students in their experiments, TEM sample preparation and was in charge of his own research experiment studying the stability of feldspars at high temperatures ($>1200°C$) in an H_2O containing environment for stability as thermal barrier coatings in jet engines. For his senior design project, he worked with Dr. Marc Anderson studying resistivity of sol-gel derived oxide films. After graduation he worked with his former professors, Drs. Evans and Lagally, in the materials integration on silicon MRSEC group studying the growth, structure, patterning and stresses of Ge-hut growth on silicon and thin silicon membranes. There he got his first exposure to ferroelectrics, high-resolution x-ray diffraction and vacuum deposition techniques.

In August 2004, he started in the Susan Trolier-McKinstry Research Group studying ferroelectric thin films. There he was first to synthesize $BiScO_3$-$BaTiO_3$ based dielectrics, for which he received his M.S. in Materials Science and Engineering in 2006. After receiving his masters, Daniel began work studying octahedral tilt transitions in perovskites, culminating in receiving his Ph.D. in December 2010.